Frontiers of Gravity: Astrophysical Environments, Ringdown Nonlinearities and the Semiclassical Approximation

by

Laura Sberna

A thesis
presented to the University of Waterloo
in fulfillment of the
thesis requirement for the degree of
Doctor of Philosophy
in
Physics

Waterloo, Ontario, Canada, 2020

Examining Committee Membership

The following served on the Examining Committee for this thesis. The decision of the Examining Committee is by majority vote.

External Examiner:	Vitor Cardoso Professor, Instituto Superior Tecnico, Departamento de Fsica
Supervisor:	Neil Turok Higgs Chair of Theoretical Physics, University of Edinburgh Senior Faculty member, Perimeter Institute for Theoretical Physics Professor of Physics, University of Waterloo
Internal Members:	Latham Boyle Junior Faculty member, Perimeter Institute for Theoretical Physics
	Robert Mann Professor of Physics, University of Waterloo
Internal-External Member:	Achim Kempf Professor, Applied Mathematics, University of Waterloo

Author's Declaration

This thesis consists of material all of which I authored or co-authored: see *Statement of Contributions* included in the thesis. This is a true copy of the thesis, including any required final revisions, as accepted by my examiners.

I understand that my thesis may be made electronically available to the public.

Statement of Contributions

The material presented in this thesis is largely my own, and it includes the portions of co-authored publications to which I made significant contributions. Text taken from publications (pages listed below) is written in the voice of the publication authors. The remaining pages are my original work, written for this thesis.

Chapter 2 of this thesis consists of material from: publication [63] (pages 14–26), co-authored with A. Caputo, A. Toubiana, S. Babak, E. Barausse, S. Marsat and P. Pani; publication [224] (pages 28–29), co-authored with A. Toubiana, A. Caputo, G. Cusin, S. Marsat, K. Jani, S. Babak, E. Barausse, C. Caprini, P. Pani, A. Sesana and N. Tamanini; publication [212] (pages 29–36, 107–109), co-authored with A. Toubiana and C. Miller.

Chapter 3 of this thesis consists of ongoing research in collaboration with P. Bosch, W. East and L. Lehner. The numerical data used in Chapter 3 was produced by P. Bosch, with code co-authored by P. Bosch, S. Green, L. Lehner and H. Roussille.

Chapter 4 of this thesis consists of material from the publication [240] (pages 68–80, 110–114), co-authored with Y. Yargic and A. Kempf.

Abstract

Einstein's general relativity is based on a tensorial, nonlinear equation for the spacetime metric. The gravitational interaction is however so weak that, in most circumstances, the equations can be solved perturbatively. This is true in early-time cosmology, for the inspiral of binary systems, and even after black holes merge, releasing the equivalent of multiple solar masses in gravitational waves. In this thesis, we analyze a range of problems that can be addressed assuming a background gravitational field and small fluctuations over it. We will progress from problems where the perturbative hypothesis can be tested and holds, to ones that begin to show nonlinear effects, ending with an application of perturbation theory to quantum gravity, where it is only a working hypothesis.

We first analyze the dynamics of black hole binaries immersed in a dense gas environment or interacting with a stellar companion. For binaries in a dense environment, we study the effect of accretion and dynamical friction on the gravitational wave emission. We derive the modification of the gravitational wave phase in the assumption of small accretion rates, and assess whether future gravitational wave observatories could detect this effect. For black holes in a binary with a white dwarf, we identify new evolutionary relations and propose a method to infer the black hole and white dwarf masses and their luminosity distance from the gravitational wave signal alone.

Next, we study how isolated black holes react to perturbations, in the simplified setting of spherical symmetry and negative cosmological constant. We show that modes belonging to the linear spectrum can be excited nonlinearly. We further find that nonlinear effects can change the black hole mass at percent level, and that this effect can be explained by the flux of characteristic excitations through the black hole horizon.

Finally, we propose a new definition of the semiclassical Einstein equations for cosmological spacetimes. We propose that the source on the right hand side of the Einstein equations could be the amount of stress-energy above the instantaneous ground state. In this more speculative application, the linear order semiclassical approximation is not guaranteed to hold. If our hypothesis were confirmed, however, the vacuum stress-energy above the instantaneous ground state would not renormalize the cosmological constant, hinting at a resolution of the longstanding problem connected to its observed value.

Acknowledgements

I am grateful to my advisor, Neil Turok. Neil gave me the opportunity to come to Perimeter, together with many opportunities to travel and meet interesting physicists. He also inspired me to aim for the big, fundamental questions in physics and to not be afraid to go against the current, and taught me this through example. I am not sure I always followed his advice but thanks to him, I will keep striving to be a better scientist.

I thank Angelika Fertig, Job Feldbrugge and Beatrice Bonga for their collaboration and support. I cherish the endless hours spent on a couch at Perimeter, working on projects that will soon see the light of day. I especially thank Angelika Fertig and Job Feldbrugge for their guidance in my first months as a PhD student.

Andrea Caputo deserves the biggest thanks for academic collaboration – and a six-years-strong friendship. Andrea gave me a big push when my research had stalled. He will make for a great supervisor one day (very soon, if you've seen his publication list).

Another special thanks goes to Alexandre Toubiana, for our fun collaborations that turned into a friendship, and to Cole Miller, for his amazingly supportive mentorship. I am also indebted to Jean-Luc Lehners for his collaboration and for hosting me at the Albert Einstein Institute on several occasions.

Although science shouldn't be about people, working with people is what I enjoy the most about it. I sincerely thank all my close collaborators and mentors: Paolo Pani, Enrico Barausse, William East, Luis Lehner, Latham Boyle, Achim Kempf, Diego Blas, Mikhail Ivanov, Stas Babak, Yigit Yargic, Alice Di Tucci, Pablo Bosch and Enrico Cannizzaro.

The international community at Perimeter Institute and in Kitchener-Waterloo made my stay in Canada joyful and unique. I thank Martina Canesi and Luca Dellantonio (my second home away from home), Jinglei Zhang, Alessandro Malusà, Davide Racco, Flaminia Giacomini and Jan Haase; Angelika Fertig, Nils Wilde, Pablo Bosch, Nayeli Galindo, Beatrice Bonga, Nestor Ortiz, Will and Annie East, Job Feldbrugge and Nynke Niezink; Anna Heffernan and Max Corman; Dani Marcheva, Laura Bernard and Lena Funcke. I am so greatful to have met you all.

My PhD started in the hardest time of my life so far. I thank my family, mia madre Maria Rita e mio fratello Francesco, for supporting me in this journey abroad despite our need for each other at home. I would not be who I am today without my family, and my life-long friends Letizia, Federica, Serena, Clara, Fabiana, Caterina, Oliviero and Gianluca, and Marco.

I thank my partner Stephen Green, for the way we support, encourage and help each other in our academic endeavors. My peace of mind, my plans for the future – and my semi-fluent English – would not exist without him. I love you tortolito.

To my father,
who never tired of my first questions
about the Universe

Table of Contents

List of Tables

List of Figures

Chapter 1

Introduction: the frontiers of gravity

1.1 Classical gravity

We live in a great era for gravitational physics. Observations of the cosmos and its components are being made over an incredible range of scales. We are now sensitive to scales close to the cosmological horizon, through the cosmic microwave background (Planck [20], near-future missions CMB-S4 [5], the Simons Observatory [18]), and through observations of the large scale structure, gravitational lensing and baryon acoustic oscillations (Sloan Digital Sky Surveys [22] and near-future Euclid [25], Rubin Observatory [132], DESI [81] and Nancy Grace Roman Space Telescope, formerly WFIRST [218]). We are also more sensitive to tensor cosmological perturbations (or the primordial gravitational wave background) than ever before, thanks to the successors of BICEP [16], pulsar timing [29, 139, 92] and other planned gravitational wave detectors. On smaller scales, current observations are probing black hole horizons through the gravitational wave emission of merging black holes [9], as well as the behavior of matter in the vicinity of horizons – by the tracking of stellar orbits (GRAVITY [15, 14]) or the observation of accretion disks emission (Event Horizon Telescope [104]).

For the first time in human history, we are probing the Universe not only through electromagnetic radiation, but through gravity waves themselves. This was the result of the decades-long experimental, numerical and theoretical effort of the gravitational-wave community. LIGO and VIRGO (to be soon joined by KAGRA [82]) are now detecting tens of black hole binary coalescences at every observing run, with 39 events detected in the latest one [11]; see Fig. 1.1. Current gravitational-wave detectors are sensitive to signals with frequencies falling in the ~ 10–10^3 Hz range, corresponding to the merger frequencies of black

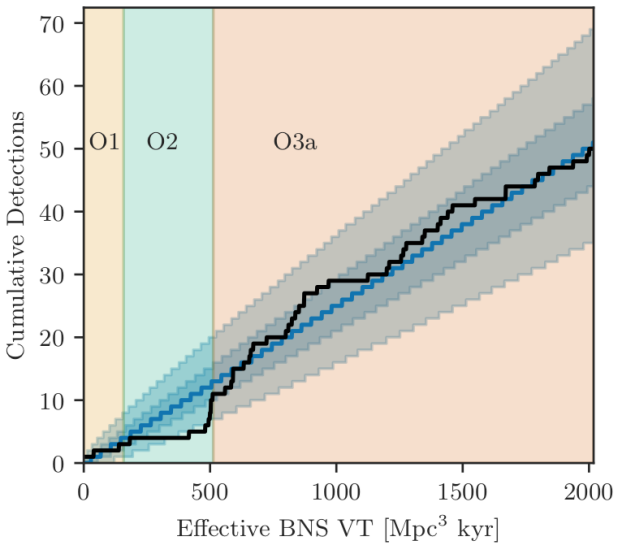

Figure 1.1: Total number of gravitational wave detections made by the LIGO-Virgo Collaboration as a function fo the effective volume-time (VT) during which the network was sensitive to (binary neutron star) coalescences [11].

holes with total mass 10–$10^3 M_\odot$. In the next one to two decades, the sensitivity in this frequency range will be improved with two proposed detectors, the Einstein Telescope [165] and the Cosmic Explorer [206]. In addition, space-borne detectors such as the Laser Interferometer Space Antenna (LISA) [31], DECIGO [137], TianQin [176], together with pulsar timing arrays (SKA [134] and IPTA [128]), will probe brand new frequencies. These new observatories will detect, at frequencies below 1 Hz and as low as nHz, new classes of gravitational wave sources: massive black hole binaries, extreme-mass-ratio inspirals, galactic binaries containing one or two stars, and (stochastic) gravitational wave backgrounds. In the dawning era of gravitational-wave astronomy, gravitational-wave observations will be able to probe the structure, evolution, and composition of the Universe. Multimessenger (*i.e.*, electromagnetic and gravitational wave) observations, moreover, promise to be even stronger probes of the Universe than the sum of the two parts.

The observations of the past ten years paint a picture of the Universe that is simpler than we could have, in some sense, hoped for. These observations have put stringent bounds on the presence of primordial tensor modes and primordial non-Gaussianities, as well as modifications of gravity at large and small scales. Most recently, gravitational-wave observations have bounded several possible alternatives to general relativity by constrain-

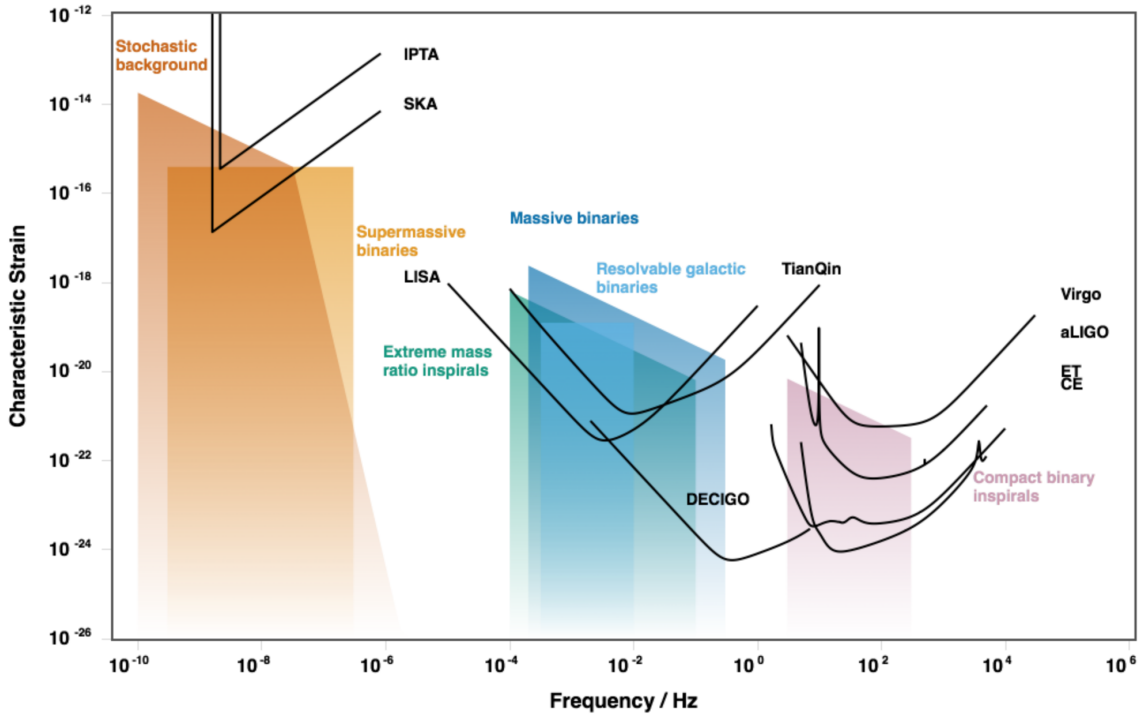

Figure 1.2: Sensitivity of present and future gravitational-wave detectors and the characteristic strain of their most important sources [185, 1].

ing deviations in the inspiral, merger and ringdown signals from compact binary coalescences [9, 7, 13]. As physicists, we had hoped that inconsistencies between the predictions of our standard theories and observations would point us to resolutions of crucial problems related to gravity: the nature of dark matter and dark energy, the beginning of the Universe, and the quantum completion of general relativity. But so far, no such inconsistencies have emerged. The reported tension in the value of the Hubble constant inferred from early and late Universe measurements [229] is still (allegedly) subject to systematic uncertainties [100]. The resolution or confirmation of this tension might need to wait for gravitational-wave standard sirens.

On the one hand, the simplicity of the picture emerging from recent observations implies that, if physics beyond our current models is to be discovered, it will require further effort. For gravitational wave observations, constraining new physics might require us to model and independently constrain complicated ordinary-matter and nonlinear effects. This will challenge our predictive abilities and require us to construct more accurate analytical and

numerical models to describe matter effects, extreme mass ratios, eccentric binaries and nonlinearities. In this direction, effort is being put in refining existing analytical formalisms to describe the coalescence of compact objects: expansions where velocities are assumed to be small compared to the speed of light (post-Newtonian [102]) and fields are assumed to be weak (post-Minkowskian [44, 45] and -Newtonian); and the self force program, where the mass ratio is used as the small expansion parameter [203]. A promising new approach is based on scattering amplitudes techniques, and is finding increasing applications in gravitational wave calculations (*e.g.*, [231]). Numerical relativity played a crucial role in the first detection of gravitational waves, and continues to push its frontiers towards eccentric, precessing and unequal mass binaries, as well as theories beyond general relativity [54, 67].

Besides describing known effects with higher accuracy, discovering new physics might require thinking outside the box, and identifying effects (and causes) that have been so far overlooked. On the other hand, the simplicity of the observed Universe could be seen as a clue, rather than a curse. Such simplicity might indicate, for example, that the application of a few fundamental principles of quantum mechanics and general relativity could explain the beginning of the universe and its current accelerated expansion, without the introduction of additional degrees of freedom.

Despite their simplicity, current observations not only exclude exotic gravitational scenarios, but also provide a wealth of information on the workings of the Universe. Gravitational-wave observations in the past five years have identified the sources producing gamma-ray bursts in the merger of binary neutron stars [6, 184, 115], discovered an environment where r-process nucleosynthesis occurs [199], discovered black holes with masses missed by X-ray observations and discovered compact, stellar-mass black hole binaries. These observations have also helped to constrain the neutron star equation of state [103] and the properties of the population of compact binaries [83].

Future gravitational-wave detectors will address more key questions in astrophysics and cosmology: how (and if) super-massive black holes merge; how (and if) different classes of binaries evolve into compact orbits; what is the internal structure of neutron stars and their merger products; what surrounds super-massive black holes at the center of galaxies; how massive black holes grow in mass with their host galaxies. Future detections will also probe further the distribution of matter in our Galaxy and the Universe, the nature of dark matter and the expansion of the Universe. A particularly promising avenue is the possibility of characterizing dark matter through gravitational-wave observations. In some settings, this can rely solely on the demonstrated fact that dark matter gravitates, independently of its other interactions with ordinary matter. Gravitational-wave observations could, for instance, probe the existence of primordial black holes, detect dark-matter-induced environmental effects leading to the dephasing of the signal or the spin-down of black holes,

probe the existence of exotic compact objects, and that of stochastic backgrounds associated with nonperturbative phenomena (phase transitions, topological defects, inflationary pre- or re-heating, extra dimensions) [43]. Thinking about the new observatories under construction, physicists and astrophysicists alike certainly hold on to one thought: "It would be unprecedented in the history of astronomy if the gravitational radiation windows being opened did not reveal new, enigmatic sources" [88], like the heavy black hole binaries already observed.

1.2 Quantum gravity

Fully quantum effects of gravity are expected to only become relevant at very high energies – or small scales, such as inside a black hole or at the Big Bang – and can be safely neglected in interpreting many of the observations mentioned so far. However, some aspects of quantum gravity in the classical limit can be important for the description of two of the targets of gravitational-wave and cosmological observations: black hole horizons and the accelerated expansion of the Universe. These effects usually fall in the region of validity of semiclassical gravity, *i.e.*, leading (first) order in an expansion in Planck's constant.

The idea that black holes could hold a key to the interpretation of quantum and semiclassical gravity has been around since the singularity theorems by Penrose and Hawking. These theorems showed the inevitability of a breakdown of the classical theory beyond black hole horizons and at very early time in cosmology. The discovery of the Hawking radiation mechanism further strengthened this connection. Nowadays, the related information paradox has become a fundamental puzzle whose resolution is a basic test for theories of quantum gravity. LIGO and Virgo's detections of gravitational waves from a variety of sources has also revived the hope that quantum or semiclassical effects could be detected or constrained with data. There are suggestions that quantum effects at the black hole horizon (*e.g.*, firewalls [24]) or the quantization of the black hole area [38, 39] could produce observable effects in the gravitational wave emission of black hole binaries. A train of echoes is predicted to follow the merger signal of these binaries, as modes that do not satisfy the quantization condition are reflected non-classically at the black hole horizon [110, 66]. Under some assumptions on the discretization unit for the black hole mass and the properties of the quantized spectrum, horizons would absorb and emit radiation in the 10^2–10^3 Hz range, accessible to ground-based detectors [21].

The accelerated expansion of the Universe, first detected with supernovae observations [207, 197] and confirmed by several other probes, is so far consistent with a constant dark energy component (for which the pressure is equal to minus the energy density) or,

equivalently, a cosmological constant introduced in the left-hand side of the Einstein equations. The most recent Planck analysis sets the observed value of the dark energy denstiy in a ΛCDM Universe to $\rho_\Lambda = 7.2583 \times 10^{-121} M_{\rm Pl}^4$ [20]. Near future observations will improve the current measurement of the dark energy density, and put stronger constraints on the equation of state. Long before precision measurements, however, the cosmological constant was considered a natural element of a general relativistic theory of gravity, fully consistent with the symmetries of Einstein's theory. In a quantum field theory perspective, it was also natural to conclude that the vacuum energies of matter fields would gravitate, and contribute to the energy density of the Universe as a cosmological constant. The observed value of this constant, however, is many orders of magnitude smaller than what any quantum field theory estimate would suggest.

The standard argument showing this discrepancy is rather naive, and does not respect Lorentz invariance in flat spacetime [144]. The argument goes as follows: the calculation of the vacuum energy density of, *e.g.*, a scalar field, involves an integral over momenta that diverges in the ultraviolet. A cut-off in momentum space is therefore introduced and set to the energy scale at which other degrees of freedom may come into play, *i.e.*, the Planck scale. One then finds that the vacuum energy density is proportional to the fourth power of the cut-off scale, or $\rho_\Lambda \sim M_{\rm Pl}^4 \sim 10^{76}\,{\rm GeV}^4$ (see, *e.g.*, [72, 236]). Cut-off regularization, however, does not respect the assumed symmetry of the spacetime in this calculation (a Minkowski metric), and the resulting stress energy tensor is not proportional to the metric, as would be required to interpret the result in terms of a cosmological constant. When using a covariant regularization scheme, such as dimensional or Pauli-Villars regularization, the discrepancy between the predicted and observed value of the cosmological constant is reduced and acquires a logarithmic dependence on the renormalization scale. The vacuum energy density of electrons alone is then found to be proportional to $\rho_\Lambda \sim -m_e^4 \log(m_e^2/\mu^2) \sim -10^{-14}\,{\rm GeV}^4$, where μ is an arbitrary renormalization scale. Unfortunately, prediction and observation are still separated by tens of orders of magnitude, and even a sign. This is because the negative contribution of fermions dominates over the one of bosons in the Standard Model. This brief discussion should serve to prove that the cosmological constant problem is challenging in its very definition, with wildly different estimates still appearing in the literature. The modern cosmological constant problem is usually phrased in terms of *technical naturalness*, by noting that the cosmological constant does not remain small as we extend our effective field theory to higher energies and include more massive degrees of freedom [61].

The cosmological constant problem has continued to challenge our understanding of quantum field theory and semiclassical gravity for the past fifty years. For this reason, Hollands and Wald call for caution over the cosmological constant problem, and suggest

that attention should rather be paid to the consistent formulation of quantum field theory on curved spacetime [129]. At the moment, the physics community has not agreed on a quantum theory of gravity, or produced one that could consistently address either the semiclassical approximation or the cosmological constant problem from first principles. All existing approaches to quantum gravity, from the ones inspired by quantum field theory, to the ones led by the geometrical interpretation of Einstein's theory, have attempted to tackle this problem with little success. String theory seems to predict a multitude of ways to realize a spacetime with accelerated expansion. A recent series of "swampland" conjectures could narrow down these "quintessence" models and explain the observed dark energy. These conjectures, however, do not currently stand on solid ground, and might be already in tension with cosmological data [23]. In some sense, the development of theoretical predictions around the cosmological constant remains far behind the advances in cosmological observations.

1.3 Summary and outline

Gravitational physics is deeply connected, per its fundamental nature, to the most pressing questions in physics, and to many traditionally distinct research areas. This thesis, as a result, embraces both observations and theoretical modeling, and develops at the intersection of astrophysics, gravitational-wave astronomy and cosmology.

We start by discussing the connection between gravitational wave sources and their astrophysical environments. Gas-rich environments, such as active galactic nuclei (AGNs), can affect the evolution of black hole binaries and their gravitational wave signal. In this thesis, we focus on the effect of two processes, namely mass accretion and dynamical friction. We describe their effect on the binary evolution (at the Newtonian level) and their observational consequences, concentrating on the gravitational wave dephasing. We explore in detail the detectability of these effects by LISA, finding favorable odds for both stellar-mass and intermediate-mass black hole binaries. However, the modification of the gravitational-wave phase induced by environmental effects is not completely unique to them. Distinct environmental effects and modifications of gravity can be essentially degenerate, especially if the effect is at the threshold of detectability. It is therefore crucial to complement gravitational-wave observations with electromagnetic follow-ups, which might characterize the environment of the binary and detect specific electromagnetic signatures. We found that this will be possible with observatories scheduled to come online before or at the same time as LISA, such as the X-ray telescope Athena [178] and the radio telescope SKA [3].

While the effect of matter in the environment is weak in most black hole binaries in compact orbits, matter within the binary can be a primary driver of the dynamics even at short separations. This is the case, for instance, when a black hole is in a binary with a white dwarf, and the binary is sufficiently close to allow for mass exchange between the companions. The gravitational-wave frequency evolution of the binary is then fundamentally affected by mass transfer, and this will clearly be detectable with LISA. In this thesis, we make important steps in the modeling of the gravitational wave signal of white dwarf–black hole binaries. Our main result is the identification of a new relation for the evolutionary tracks followed by this class of binaries. This can be used as a new observational tool, which will allow for the inference of the masses and luminosity distances of white dwarf–black hole binaries.

Astrophysical phenomena in the inspiral phase are only one of the modeling challenges facing gravitational-wave astronomy. The ringdown, the gravitational-wave signal immediately following a binary merger, has recently presented us with observational challenges that have nothing to do with matter effects, and everything to do with the properties of the Einstein equations. The latter being complicated, nonlinear tensorial equations, it was suspected that linear black hole perturbation theory would fail for a few dynamical times after a remnant black hole is formed in a merger. The analysis of state-of-the-art numerical simulations has revealed that this might not be the case, or that nonlinearities might not take the form we expected. While the implications of these analyses are still being debated, in this thesis we attempt to characterize nonlinearities by performing "experiments" on a simplified black hole system. Our choice of testing ground is a scalar field-black hole system in spherically symmetry and with a negative cosmological constant. The scalar field allows to study interesting dynamics (absent in pure gravity in spherical symmetry), while the anti de Sitter (AdS) asymptotics (with reflective boundary conditions) can boost nonlinear behavior, because of the absence of dissipation. In this system, we can set the initial conditions for the scalar field to match a linear mode configuration. Thanks to the orthogonality of the linear modes, we can easily identify extra modes in the scalar ringdown as having been generated nonlinearly. Our main result is that nonlinearities excite modes within the linear spectrum, rather than producing completely new features. This is an important step in the understanding of ringdown nonlinearities, although much remains to be done.

Gravitational physics, despite its nonlinear features, is fairly well understood at the classical level. A much bigger challenge is revealed whenever we try to incorporate elements of quantum mechanics into general relativity. The semiclassical approximation for gravity is the final topic of this thesis. We propose a minimal modification of the standard approach to semiclassical gravity in a cosmological setting, and study its implications with a focus on

the cosmological constant problem. The proposal consists in a redefinition of the quantum contribution to the right hand side of the Einstein equation, *i.e.*, a redefinition of the expectation value of the stress energy tensor of the matter fields. We find that our proposal, within its assumptions and limitations (free theories on a Friedman-Robertson-Walker background spacetime), indicates a possible path to the resolution of the decades-long conundrum surrounding the value and renormalization of the cosmological constant.

In Chapter 2 we give a brief summary of astrophysical phenomena potentially relevant to gravitational-wave sources containing a black hole. We then present our results on mass accretion and dynamical friction in black hole binaries, and on mass transfer in white-dwarf black hole binaries.

In Chapter 3 we summarize the status of the nonlinearity problem in the black hole ringdown. We then describe our set up and present the analysis of numerical simulations. We conclude with the calculation of the back-reaction of scalar perturbations onto the black hole mass, and discuss the potential steps we could take in the future to push further our understanding of nonlinearities in more realistic systems.

In Chapter 4, we begin by summarizing the standard semiclassical approximation in gravity, and the present status of the cosmological constant problem. We describe our proposal for a renormalized stress-energy tensor, clearly stating the assumptions made and its implications for the renormalization of the cosmological constant. We conclude by providing a possible pathway to overcome our simplifying assumptions.

In this thesis, we use the metric signature $(-,+,+,+)$ and natural units, $G = c = 1$ unless stated otherwise.

Chapter 2

Astrophysical environments

2.1 Black holes in astrophysical environments

The gravitational wave signal from a binary containing a stellar mass or intermediate mass black hole (BH) is affected by matter effects if

- the binary companion is not a black hole but a star (broadly defined to include non-standard objects such as boson stars [214]). Examples most relevant to gravitational-wave (GW) observations are neutron star–black hole binaries [111] and white dwarf–black hole binaries; or
- the binary is immersed in a matter-rich environment, such as an active galactic nucleus (AGN) [224] or a dark matter over-density (spike, whose existence is however debated) [99]. Black hole binaries may form preferentially in the gas-rich nuclear regions surrounding AGNs [175] – as a result, *e.g.*, of third body interactions with the central black hole or fragmentation/instabilities of the AGN accretion disk.

Supermassive black holes at the center of merging galaxies or extreme mass-ratio inspirals (EMRIs) would deserve a separate treatment, which is beyond the scope of this Chapter. Here we will focus on stellar mass and intermediate mass black holes.

There is currently little evidence that the stellar mass black holes observed by gravitational-wave detectors live in gas-rich environments. The only exception is GW190521, the most massive compact binary merger observed by the LIGO/Virgo Collaboration to date, with progenitor black-hole masses of $85^{+21}_{-14}\,M_\odot$ and $66^{+17}_{-18}\,M_\odot$ [10, 12]. Remarkably, the Zwicky

Transient Facility observed an optical flare (ZTF19abanrhr), interpreted as coming from the kicked GW190521 merger remnant moving in an AGN disk [118]. The flare occurred $\sim$ 34 days after GW190521 (the delay being ascribed to the remnant's recoil) in AGN J124942.3+344929 at redshift $z = 0.438$. If confirmed, this would be the first electromagnetic counterpart to a BH coalescence. Unfortunately, evidence in support of this association is not sufficiently strong to make this claim [30].

When black holes do inhabit a gas-rich environment, or posses a stellar companion, environmental/matter effects can manifest in several forms. We list a few of them below:

- mass accretion, either from the surrounding matter or from the binary companion. Matter accreted can be ordinary or exotic/dark;
- tidal interactions within the binary;
- dynamical friction, planetary migration (the effect of differential gas torques in an accretion disk) or other forms of gravitational pull exerted by the surrounding matter;
- electromagnetic field effects (magnetic fields, electric charge, or even superradiant growth of photons acquiring mass in a plasma [85], an effect still being debated [48, 65]).

For a comprehensive review, see [34]. Environmental effects can also depend on the presence of a third (or more) body, as is the case for

- Kozai-Lidov resonances [155, 145], which can induce eccentricity in the binary and leave a dynamical imprint on the gravitational wave signal;
- Doppler shifts, when the binary orbits around a third body, causing its distance from the detector to vary;
- gravitational lensing, which could produce multiple images and also affect the single gravitational wave signal [105];
- Shapiro delay, and other relativistic effects such as spin-orbit and spin-spin couplings [241, 106].

Most of these effects are not relevant (or only marginally, for instance in the case of gravitational lensing) to current gravitational wave detections made by the LIGO-Virgo

Collaboration. Some effects will however be relevant at lower gravitational wave frequencies, when the binary components are further apart and their gravitational attraction will not be necessarily the dominant dynamical drive. Even at lower gravitational wave frequencies, most of these effects will only be relevant for a subset of events: those located in a sufficiently dense environment, on a sufficiently tight orbit around a third body, or those events equipped with a stellar member in the binary [34, 64].

Matter effects, if detected, could provide information on the environment where the binary formed and identify the binary as belonging to a specific population (*e.g.*, AGN binaries [221, 124]). They can also narrow down the search for electromagnetic counterparts, suggesting, *e.g.*, to cross-correlate the gravitational wave localization with AGN catalogues. However, matter effects could also obstacle tests of gravity at low gravitational wave frequencies, where signals could be modified in a similar way by, *e.g.*, a time-varying Newton's constant or a vacuum dipole emission [36, 73, 117].

In this Chapter, we describe a range of matter effects, their consequences on the gravitational wave signal and their observability by future observatory LISA. Matter accretion from the surroundings of stellar origin and intermediate mass black hole binaries (SOBHB and IMBHB, respectively) is the topic of Section 2.2, while Section 2.3 briefly discusses analogous results related to dynamical friction. SOBHBs will be first observed in the LISA $\sim$ mHz band, and will then disappear for weeks/months before entering the $\gtrsim 1$ Hz band of ground detectors, where they merge [215]. Despite this frequency gap, piercing together the LISA low-frequency regime and the terrestrial high-frequency merger will allow for effectively observing these systems for 10^5–10^6 GW cycles. Therefore, even small inaccuracies in modeling the GW phase evolution will bias the estimation of the parameters (and particularly the merger time) or even prevent detection by LISA. IMBHBs might be detected by LISA for the first time for a whole range of total masses and mass ratios, with the lighter binaries spending more time in band. While the existence of intermediate-mass black holes has not been confirmed yet, several candidates exist (see, *e.g.*, Ref. [179] for a review), and they might also provide seeds for the growth of the supermassive black holes that are ubiquitously observed in the local universe (see, *e.g.*, [179, 150]). While their formation mechanism is unknown, proposed scenarios include direct collapse of massive first-generation, low-metallicity Population III stars [163, 210], runaway mergers of massive main sequence stars in dense stellar clusters [180, 168]; accretion of residual gas onto stellar-origin black holes [154]; and chemically homogeneous evolution [169].

Both SOBHBs and IMBHBs offer the potential to constrain low-frequency modifications of the phase evolution, *if* the latter are included in the GW templates used for the analysis in the LISA band. The results of Sections 2.2 and 2.3 extend the work of Barausse, Cardoso and Pani [34] by computing the leading order GW phase correction for binaries

with comparable masses, and better estimating the detectability of these effects with Fisher matrix analyses and population estimates.

Section 2.4 also deals with mass accretion onto a black hole but, this time, the mass is being transferred within the binary rather than from the surrounding environment. The binaries we have in mind, white dwarf–black hole (WDBH) systems, have received little attention compared to other classes of galactic binaries (see however [227]). Population studies predict that tens of thousand of mass-transferring WDBHs could form in the Milky Way (see, *e.g.*, [131], [242]), but the rates are still uncertain by more than an order of magnitude. The expectation is that binaries containing a black hole will be subdominant in the range of frequencies relevant for LISA ($0.1 - 1\,\mathrm{mHz}$, see, *e.g.*, [188]). In particular, although Breivik et al. [56] suggest that LISA might not see any detached WDBHs in the Galaxy, Kremer et al. [147] find that a few events could come from systems formed through binary interactions in Galactic globular clusters. Overall, these sources are often discarded in BH population synthesis simulations (*e.g.*, [148]) and further investigations are needed to predict the rate of their mass-transferring phase.

These systems are particularly exciting because, as we will show in Section 2.4, LISA could be the first observatory to confirm their existence – or at the very least, provide a complementary investigation of this elusive population. There are no confirmed observations of WDBH binaries from electromagnetic surveys, although these binaries, like other mass-transferring systems, are expected to emit across a broad spectrum and have even been suggested to produce gamma-ray bursts [95]. The X-ray binary X-9, in the globular cluster 47 Tucanae, might host a white dwarf (WD) and a BH ([181], [225], [78]), but the system is also consistent with a neutron star accretor. Other candidates include XMMUJ122939.7 + 075333 in a globular cluster of the Virgo Galaxy NGC 4472 [161].

In Section 2.4, we present a semi-analytical model for mass-transferring white dwarf–black hole binaries and derive a new relation for their evolutionary tracks. We use the latter to show that LISA observations could infer the binary masses and luminosity distance, something not possible without the new evolutionary relation or for other galactic binaries.

2.2 Mass accretion from the surrounding gas

2.2.1 Accretion in the gravitational waveform

An accreting binary can be described by a Hamiltonian $H(q, p)$, where the masses m_1, m_2 vary adiabatically, $dm_i/dt \ll m_i \frac{\omega}{2\pi}$. As shown for instance in [149] and [217], the action

variables $I_q = \oint p\mathrm{d}q/(2\pi)$ are adiabatic invariants. To see this, consider a Hamiltonian $H(q,p,\lambda)$ which is a function of an adiabatically varying parameter λ. The energy will then vary with time according to

$$\frac{dE}{dt} = \frac{\partial H}{\partial t} = \frac{\partial H}{\partial \lambda}\frac{d\lambda}{dt}\,. \tag{2.1}$$

Averaging over a period, $\langle x\rangle = \frac{1}{T}\int_0^T x\,dt$, and using the fact that over a period λ varies slowly, the equation above becomes

$$\langle\frac{dE}{dt}\rangle = \langle\frac{\partial H}{\partial \lambda}\rangle\frac{d\lambda}{dt}\,. \tag{2.2}$$

We can use $\frac{dq}{dt} = \frac{\partial H}{\partial p}$ to rewrite the period as $T = \oint \frac{dq}{\frac{\partial H}{\partial p}}$, and take the energy approximately independent of the adiabatic parameter, $\frac{dE}{d\lambda} = \frac{\partial H}{\partial \lambda}\Big|_q + \frac{\partial H}{\partial p}\frac{\partial p}{\partial \lambda}\Big|_q = 0$, to rewrite

$$\langle\frac{dE}{dt}\rangle = \frac{d\lambda}{dt}\frac{1}{T}\int_0^T \frac{\partial H}{\partial \lambda}dt = -\frac{d\lambda}{dt}\frac{1}{\oint \frac{dq}{\frac{\partial H}{\partial p}}}\oint \frac{\cancel{\frac{\partial H}{\partial p}}\frac{\partial p}{\partial \lambda}}{\cancel{\frac{\partial H}{\partial p}}}dq\,. \tag{2.3}$$

Bringing the last result to the left-hand side, we find

$$\oint dq\left[\langle\frac{dE}{dt}\rangle\frac{\partial p}{\partial E} + \frac{d\lambda}{dt}\frac{\partial p}{\partial \lambda}\right] = 0, \tag{2.4}$$

which implies the conservation of the action variables defined above, $\langle dI/dt\rangle = 0$.

In the case of a Newtonian binary, working in polar coordinates r,ϕ and in the center of mass frame, we then have that $I_\phi = p_\phi$ and $I_r = \oint p_r \mathrm{d}r/(2\pi)$ are conserved under accretion [1]. The latter implies that circular orbits remain circular under accretion, while the former is equivalent to the conservation of the orbital angular momentum under accretion. Then, to leading order, angular momentum is only lost through GWs [198],

$$\dot{L}_{GW} = -\frac{32\,m_1^2\,m_2^2\,M^{1/2}}{5\,r^{7/2}} = -\frac{32}{5}\mu^2\omega^{7/3}\,M^{4/3}\,. \tag{2.5}$$

where $M = m_1 + m_2$ is the total mass, $\mu = m_1 m_2/M$ is the reduced mass and ω is the orbital angular frequency. Defining the reduced angular momentum $\tilde{L}_z = L_z/\mu M$, the evolution of the binary can be obtained through

$$\dot{\tilde{L}}_z = \frac{\dot{L}_{GW}}{\mu M}\,. \tag{2.6}$$

[1] Ref. [71] showed that accretion and dynamical friction can actually increase the eccentricity of the binary, but this effect is subdominant at the frequencies considered in this Chapter.

Integrating Eq. (2.6), one can find the evolution of the orbital frequency induced by GW emission,

$$\omega_{\rm GW}(t) = \left(\omega_0^{-8/3} - \frac{256}{5} M^{2/3}\,\mu\,t\right)^{-3/8} , \tag{2.7}$$

where $\omega_0 = \pi f_0$ is the orbital frequency at $t = 0$ in terms of the initial GW frequency. The time as a function of the orbital frequency is found inverting Eq. (2.7),

$$t_{\rm GW}(\omega) = t_c - \frac{5}{256\,\mu\,M^{2/3}\,\omega^{8/3}} , \tag{2.8}$$

where t_c is the merger time in the Newtonian approximation, corresponding to $\omega \to \infty$ in (2.7). In the stationary-phase approximation, the GW phase in frequency space $h(f) \sim |h(f)|e^{i\phi(f)}$ can be computed from the evolution of the angular frequency [89, 164]

$$\phi_{\rm GW}(f) = 2\pi f t_c + \phi_c - 2\int_t^{t_c} \omega_{\rm GW}(t')dt' = 2\pi f t_c + \phi_c + \frac{3}{4}\left(8\pi\mathcal{M}f\right)^{-5/3} , \tag{2.9}$$

where ϕ_c is the phase at merger and $\mathcal{M} = \mu^{3/5}M^{2/5}$ is the chirp mass of the system.

We shall now compare these known results with what happens in the presence of mass accretion. We assume that the binary is surrounded by gas and that both bodies are accreting mass at a same fraction of the Eddington rate,

$$f_{{\rm Edd},i} = \frac{\dot{m}_i}{\dot{m}_{\rm Edd}} , \tag{2.10}$$

where $\dot{m}_{\rm Edd} \simeq 2.2\times10^{-8}\left(\frac{m_i}{M_\odot}\right) M_\odot\,{\rm yr}^{-1}$ is the Eddington accretion rate (obtained from the Eddington luminosity assuming radiative efficiency of 10%). Then the two component masses grow in time as

$$m_i(t) = m_{i,0}\,e^{f_{\rm Edd}\,t/\tau} , \tag{2.11}$$

where $\tau = 4.5\times10^7\,{\rm yr}$ is known as the Salpeter time scale and $m_{i,0}$ is the initial mass of the i-th body. The subscript zero in this section will always refer to a quantity measured at the beginning of the gravitational wave observation. When this time dependence is taken into account in the expression for the angular momentum, Eq. (2.6) acquires an extra term:

$$\dot{\tilde{L}}_z = \frac{\dot{L}_{GW}}{\mu M} - \tilde{L}_z\frac{(\mu\dot{M})}{\mu M} . \tag{2.12}$$

In this equation, all masses should be considered time dependent, except the ones appearing in the angular momentum radiated by GWs. This is because accretion may or may not

be adiabatic compared to GW emission, depending on the frequencies at play. We have verified that results do not depend strongly on this assumption.

Accretion will in general be accompanied by a drag force $\vec{F}_{\rm drag}$ due to the fact that the accreted material carries some angular momentum. This effect can be quantified as

$$\vec{F}_{{\rm drag},i} = \dot{m}_i(\vec{v}_{\rm gas} - \vec{v}_i)\,. \tag{2.13}$$

for each mass, where $\vec{v}_i$ is the velocity of the i-th body and $\vec{v}_{\rm gas}$ is the gas velocity. For simplicity we parametrize this effect with a constant factor ξ, fixed by the relative velocity between the gas and the perturber [35, 34, 76],

$$\vec{F}_{{\rm drag},i} \simeq -\xi\,\dot{m}_i\vec{v}_i \quad \to \quad \dot{L}_{\rm drag} = -\xi\,\dot{\mu}\,r^2\omega\,. \tag{2.14}$$

Note that the parameter ξ can be positive (drag) or negative (pull, see, *e.g.*, [123]). At leading order in $f_{\rm Edd}\xi$, the term $\dot{L}_{\rm drag}/\mu M$ should be added to the right-hand side of Eq. (2.12) to take the effect of drag into account.

We can now solve the total angular momentum variation equation for the orbital frequency,

$$\omega_{\rm acc}(t) = 5^{3/8}e^{f_{\rm Edd}\frac{(3\xi+5)}{\tau}t}\left(5\,\omega_0^{-8/3} - \frac{768\,\mu_0\,M_0^{2/3}\tau\left(e^{f_{\rm Edd}\frac{(24\xi+35)}{3\tau}t}-1\right)}{(24\xi+35)f_{\rm Edd}}\right)^{-3/8}\,, \tag{2.15}$$

where M_0 and μ_0 are the initial values of the total and reduced mass, respectively. The quadrupolar radiation emitted by the source under GW emission and accretion is represented in Fig. 2.1 in the time domain. Eq. (2.15) cannot be inverted exactly to find $t = t(\omega)$. We therefore use a perturbative expansion valid when the accretion correction is small, *i.e.*, we assume $t_{\rm acc}(\omega) = t_{\rm GW}(\omega) + f_{\rm Edd}\,t^{(1)}_{\rm acc}(\omega) + \mathcal{O}(f^2_{\rm Edd})$. We verified this to be an excellent approximation in all realistic situations, including when $f_{\rm Edd} \sim 1$–100. This is because the dimensionless parameter always appears in the combination $f_{\rm Edd}\cdot t/\tau$, and the evolution times scales that we consider are always smaller than the Salpeter time scale.

In terms of the GW frequency, we find

$$t^{(1)}_{\rm acc}(f) = -\frac{25\left(\pi^{16/3}f^{16/3}(24\,\xi+35) - 3\pi^{16/3}f_0^{16/3}(8\,\xi+15) + 10\,\pi^{16/3}\,(f f_0)^{\,8/3}\right)}{393216\,\pi^{32/3}\,(f f_0)^{\,16/3}\mu_0^2\,M_0^{4/3}\tau}. \tag{2.16}$$

Finally, we can compute the contribution of accretion to the GW phase in the stationary phase approximation, expanding $\phi = 2\pi f t_{\rm acc} - \int_0^{t_{\rm acc}} 2\,\omega_{\rm acc}\,{\rm d}t = \phi_{\rm GW} + \phi_{\rm acc} + \mathcal{O}(f^2_{\rm Edd})$ to

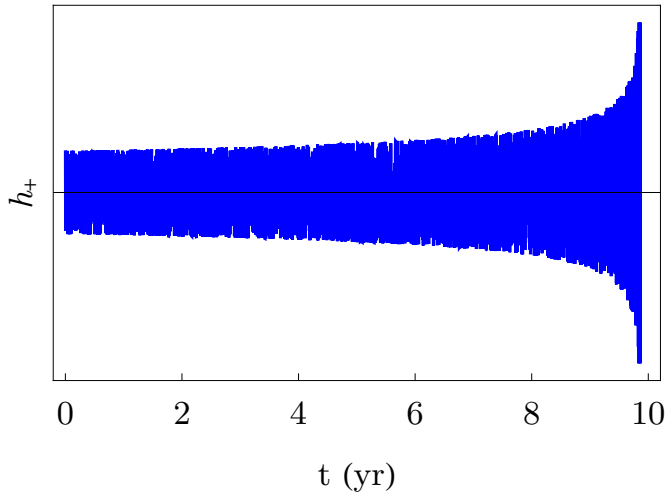

Figure 2.1: Schematic evolution of the gravitational wave signal from an accreting black hole binary, in the ten years before merger and in the presence of accretion. To the eye, the signal resembles vacuum emission.

first order in $f_{\rm Edd}$ to identify $\phi_{\rm acc}$. We find, again as a function of the GW frequency,

$$\begin{aligned}\phi_{\rm acc} = &- f_{\rm Edd}\,(8\,\xi+15)\,\frac{75\,\mathcal{M}_0}{851968\,\tau}\,(\pi f\mathcal{M}_0)^{\,-13/3} + f_{\rm Edd}\,\frac{25}{32768\,\pi^{8/3}\,f_0^{8/3}\,\mathcal{M}_0^{5/3}\,\tau}\,(\pi f\mathcal{M}_0)^{\,-5/3}\\ &+ f_{\rm Edd}\,(3\,\xi+4)\,\frac{25}{19968\,\pi^{13/3}\,f_0^{13/3}\,\mathcal{M}_0^{10/3}\tau}\\ &- f_{\rm Edd}\,(24\,\xi+35)\,\frac{25}{196608\,\pi^{16/3}\,f_0^{16/3}\,\mathcal{M}_0^{13/3}\tau}\,(\pi f\mathcal{M}_0)\ . \end{aligned} \tag{2.17}$$

In the expression above, the terms linear in frequency and independent of frequency can be reabsorbed in the definition of the time to coalescence t_c and the phase at coalescence ϕ_c, respectively. Eq. (2.17) tells us that the GW signal will be dominated by the effect of accretion if the frequency is sufficiently low. By comparing the size of the leading-order phase term in the vacuum waveform – $\sim f^{-5/3}$, 0th order in a post-Newtonian (PN) expansion[2] – and the -4PN term ($f^{-13/3}$) induced by accretion, we find that accretion is

[2]In the GW phase, a nPN correction scales as $v^{2n} \sim f^{2n/3}$ relative to the leading-order general relativistic term.

the dominant effect at frequencies below[3]

$$f_{\rm acc} \simeq \frac{1}{\pi}\left(\frac{25}{3}\frac{45}{6656}\frac{f_{\rm Edd}}{\tau}\right)^{3/8}\mathcal{M}^{-5/8}\,. \tag{2.18}$$

While in Eq. (2.17) we show all the terms of the expansion, we have verified that the -4PN term dominates. The inclusion of the 0PN term changes the results detailed below by less than 1%. This is expected since most of the binary evolution in the LISA band takes place at large separation/low frequencies. In other words, the black hole binaries analyzed in this Section will emit GWs well above the frequency at which accretion becomes subdominant,

$$f \gg 1.1\times 10^{-4}\left(\frac{f_{\rm Edd}}{1}\right)^{3/8}\left(\frac{\mathcal{M}}{10\,M_\odot}\right)^{-5/8}{\rm Hz}\,. \tag{2.19}$$

In the analysis presented below we also discarded the terms proportional to the drag coefficient ξ, which would add an additional parameter in our waveform and require proper modeling of the distribution of the gas and its velocity around the black holes. From the functional form of Eq. (2.17) we can see that neglecting the drag does not affect the frequency dependence of the GW phase, while it might affect the size (and even the sign) of the effect. However, $f_{\rm Edd}$ and ξ enter the two leading terms in Eq. (2.17) in different combinations, which could help disentangle the two effects if both terms are detected and if the two effects are of comparable strength.

2.2.2 First estimate of the effect of accretion

As a result of accretion, the phase evolution accelerates and the binary merges earlier (*i.e.*, in less time and in fewer GW cycles) than in vacuum. In Fig. 2.2 we show the time T needed for a SOBHB to enter the band of ground detectors (top panel), the time difference ΔT in the delay to enter a ground-based detector frequency band ($f = 10$Hz) induced by accretion (middle panel), and the difference $\Delta\phi$ in the total (accumulated) GW phase due to accretion (bottom panel), as functions of the initial GW frequency in the LISA band and for various SOBHB masses. All these quantities can be computed either numerically solving Eq. (2.12) or using the perturbative expansions in Eqs. (2.16–2.17). The two approaches are in excellent agreement because the contribution of accretion is subdominant in all cases.

As a useful rule of thumb, time differences $\Delta T > 10\,$s [215] and phase differences $\gtrsim 1$ rad [109, 157] are large enough to be detectable. For low initial frequency, the effect of

[3] In the absence of other non-vacuum, beyond-general relativity effects.

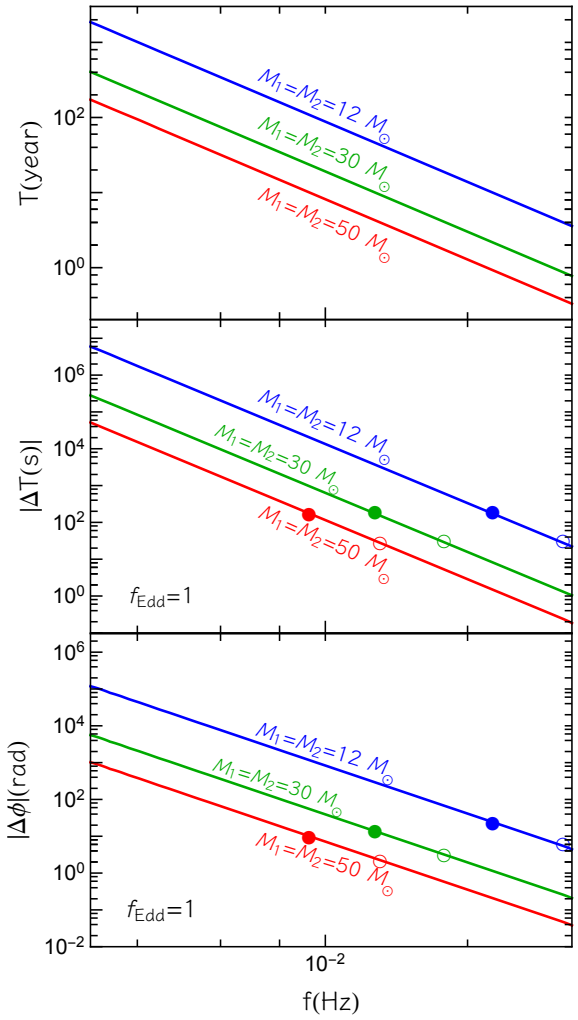

Figure 2.2: Time T needed to enter the band of terrestrial detectors neglecting accretion (top), time difference caused by accretion (middle), and corresponding GW phase difference (bottom), as functions of the initial GW frequency for three equal-mass stellar origin black hole binaries. We choose $f_{\rm Edd} = 1$ as a reference, since the time and phase differences scale linearly with $f_{\rm Edd}$ at leading order. The full (empty) circles mark the points corresponding to $T = 10\,{\rm yr}$ ($T = 4\,{\rm yr}$). The systems to the right of the full (empty) circles therefore have $T < 10\,{\rm yr}$ ($T < 4\,{\rm yr}$).

accretion on ΔT and on the phase is stronger, but the time T is also very large, *i.e.*, multi-wavelength observations will be impossible in practice. One may try to detect accretion

with LISA data alone, but note that the mission's duration will not exceed 10 yr (with a nominal duration of 6 yr), due to the finite consumables carried by the spacecraft. For these reasons, we mark in Fig. 2.2 the phase and time differences for a SOBHB that enters the band of ground detectors in 10 (4) yr by full (empty) circles. The part of the curves to the right of these circles then corresponds to $T < 10\,\mathrm{yr}$ ($T < 4\,\mathrm{yr}$), which would make a joint LISA+ground detection possible in practical terms. Overall, the results of Fig. 2.2 (which scale linearly with $f_{\rm Edd}$) suggest that only $f_{\rm Edd} > 0.1$ would give a potentially detectable effect, *i.e.*, $\Delta T > 10\,\mathrm{s}$ and $\Delta\phi \gtrsim 1$. We will verify this with more rigorous techniques in the following.

2.2.3 Fisher matrix and rates

In order to quantify the ability of multiband SOBHB detections and standalone IMBHB observations to constrain the accretion model, we perform a Fisher matrix analysis to explore the whole parameter space. Note that the Fisher matrix analysis is only valid for large signal-to-noise ratios (SNRs) [226]. Therefore, we expect it to provide only qualitatively correct results for SOBHBs in the LISA band (for which the SNR is at most $15 - 20$ in the most optimistic cases, see below). Nevertheless, we expect the Fisher matrix analysis to be accurate for the IMBHBs we consider, for which $\mathrm{SNR} = \mathcal{O}(100)$.

In the Fisher analysis we only account for the contribution due to accretion in the GW phase, and neglect the subleading contribution to the amplitude. Since accretion is important at low frequency, high-order PN terms (including the spin) should be irrelevant for our analysis, but we include them for completeness and to estimate possible correlations. For simplicity, in the Fisher analysis we also neglect the motion of the antenna during the observation.

Finally, we consider two situations: one (referred to as *LISA+Earth*) in which we simulate a multiband SOBHB detection (LISA combined with a ground-based interferometer) and another (referred to as *LISA-only*) in which we simulate a standalone (either SOBHB or IMBHB) detection by LISA. In the *LISA+Earth* case, to simulate a multiband detection one can follow two options: combine statistically the noise curves of LISA with that of a given ground-based detector or, alternatively (but less rigorously), assume that the merger time can be computed independently by the ground-based detector, so that the dimension of the parameter space of the analysis is effectively reduced. In the Fisher analysis, we follow the latter, simpler approach, and we therefore effectively remove the merger time from the template parameters in the *LISA+Earth* case.

We adopt the LISA noise curve reported by [31], whose high frequency part is based

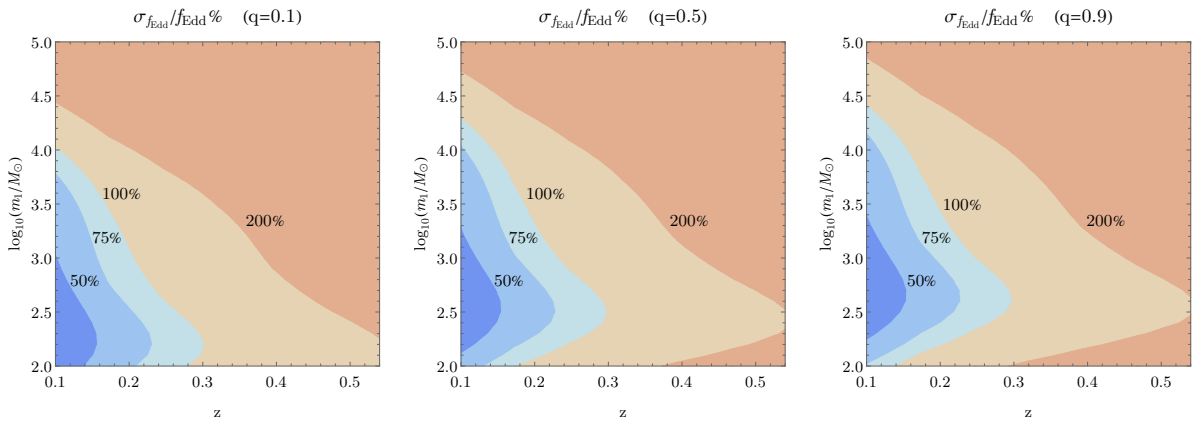

Figure 2.3: Fisher matrix percentage uncertainties on the Eddington ratio for IMBHBs across parameter space. We show different mass ratios ($q = m_1/m_2$, from left to right), redshift z and source-frame mass m_1.

on a single link optical measurement system noise of 10 pm/$\sqrt{\rm Hz}$.We adopt a TaylorF2 template approximant for spinning binaries up to 3.5PN order [98], with the addition of the leading-order accretion term presented in Eq. (2.17). Therefore, our GW template for the Fisher analysis has *seven* parameters (masses, merger time and phase, the two dimensionless spins $\chi_{1,2}$, besides the Eddington accretion ratio $f_{\rm Edd}$).

Given a waveform template $h(\vec{\zeta}, f)$ in the frequency domain and a set of waveform parameters $\vec{\zeta}$, the error associated with the measurement of parameter ζ^a (with all other parameters marginalized upon) is $\sigma_a = \sqrt{\Sigma^{aa}}$, where the covariance matrix Σ^{ab} is given by the inverse of the Fisher matrix, $\Gamma_{ab} = \left(\partial_{\zeta^a} h | \partial_{\zeta^b} h\right)_{\vec{\zeta}=\vec{\zeta}_0}$. Here, $\vec{\zeta}_0$ are the injected values of the parameters, and the inner product is defined by

$$(g|h) = 4\,\mathrm{Re}\int_{f_0}^{f_{\rm max}} df\,\frac{\tilde{h}(f)\tilde{g}^*(f)}{S_h(f)}\ , \tag{2.20}$$

where $S_h(f)$ is the detector noise spectral density.

The results of the Fisher matrix analysis for IMBHBs (in the *LISA-only* scenario) are shown in Figure 2.3. We find that 50% or lower relative uncertainties on Eddington-level accretion could be achieved for binaries with redshift below ~ 0.2, and with primary masses below $\sim 1000 M_\odot$. However, the number (and the very existence) of IMBHBs in the LISA band is very uncertain. We cannot therefore draw conclusions on the number of systems for which LISA could detect accretion.

On the other hand, our Fisher-matrix analysis, coupled with simulated astrophysical populations calibrated to the LIGO/Virgo data, can easily provide estimates of the number of SOBHBs detectable by LISA for which accretion can be measured. The intrinsic number of SOBHBs merging per (source-frame) unit time and (source-frame) masses is given by [127]

$$\frac{\mathrm{d}\dot{N}}{\mathrm{d}m_1\mathrm{d}m_2} = \int \mathrm{d}z\, R \frac{\mathrm{d}d_C}{\mathrm{d}z} \frac{\mathrm{d}^2 p}{\mathrm{d}m_1\mathrm{d}m_2} 4\pi d_C^2, \tag{2.21}$$

where d_C is the comoving distance, $R = 53.2\,\mathrm{Gpc}^{-3}\mathrm{yr}^{-1}$ is the best estimate for the intrinsic merger rate measured by the first and second LIGO/Virgo runs [8], the probability distribution function for the source-frame masses – $\mathrm{d}^2p/\mathrm{d}m_1\mathrm{d}m_2$ – is given by "model B" of [8], while

$$\frac{\mathrm{d}d_C}{\mathrm{d}z} = \frac{1}{H_0\sqrt{\Omega_m(1+z)^3+\Omega_\Lambda}}$$

is computed using a fiducial cosmology $H_0 = 67.9\,\mathrm{km/s/Mpc}$, $\Omega_m = 0.306$, $\Omega_\Lambda = 0.694$ [17]. In order to obtain synthetic astrophysical catalogues of merging as well as inspiraling sources, we use Eq. (2.21) to simulate mergers in a period much longer than the LISA mission duration, by assuming a uniformly distributed merger time t_c. The latter can be easily converted into the initial GW frequency $f_0 = [5/(256\,t_c)]^{3/8}\mathcal{M}^{-5/8}/\pi$, where f_0, t_c, and the chirp mass $\mathcal{M}$ must be computed in the same (detector- or source-) frame.

We constrain the comoving distance in the range $d_C \leq 2\,\mathrm{Gpc}$ and the initial source frame GW frequency in the range $f_0 \in [4\,\mathrm{mHz}, 10\,\mathrm{Hz}]$. For the chosen mass model we generate 20 realizations, and for each realization we consider two LISA mission durations (4 or 10 yr), for a total of 40 catalogues.

In the *LISA-only* case for SOBHBs, we assume that a single event within the catalog is detected if either of the following conditions occurs [186, 223]

$$\begin{aligned} &t_c < 100\,\mathrm{yr} \text{ and } \mathrm{SNR} \geq 15, \text{ or} \\ &t_c > 100\,\mathrm{yr} \text{ and } \mathrm{SNR} \geq 10\,, \end{aligned}$$

where the latter SNR threshold is lower because binaries with long merger times are accurately described by Newtonian waveforms in the LISA band [167] and can be therefore detected by a different search strategy [223], akin, *e.g.*, to the one used for white-dwarf binaries.

In the *LISA+Earth* case, the SNR threshold is lower for events that can be detected on Earth [186, 223]

$$t_c < 10\,\mathrm{yr} \text{ and } \mathrm{SNR} \geq 9.5\,. \tag{2.22}$$

	LISA-only				
$T_{\rm obs}$	All	$f_{\rm Edd}$	100%	50%	10%
4 yr	77 ± 8	1	0	0	0
		10	1.6 ± 1.4	0.6 ± 0.6	0
10 yr	182 ± 10	1	1.5 ± 1.2	0.4 ± 0.7	0
		10	11 ± 3	9.5 ± 2.7	1.5 ± 1.2
	LISA+Earth				
$T_{\rm obs}$	All	$f_{\rm Edd}$	100%	50%	10%
4 yr	88 ± 8	1	0.1 ± 0.2	0	0
		10	4.1 ± 2.3	1.7 ± 1.2	0.1 ± 0.2
10 yr	207 ± 11	1	5.2 ± 1.9	1.1 ± 1.2	0.1 ± 0.2
		10	36 ± 4	32 ± 3	5.2 ± 1.9

Table 2.1: Number of detectable SOBHB events for various configurations. "All" stands for the total number of detectable events, whereas 100%, 50%, and 10% stand for the number of events for which $f_{\rm Edd}$ is measured with a relative error of 100%, 50%, and 10%, respectively, according to the Fisher analysis. All numbers are averaged over 20 catalogues and presented with $1\,\sigma$ errors. Super-Eddington accretion will be detectable for a good fraction of multiband events if the LISA mission duration is 10 years.

These events would indeed be detected through an archival search following their ground-based detection.

For the simulated astrophysical populations we then use a Fisher matrix analysis to quantify the possibility to measure $f_{\rm Edd}$ at a given precision. Table 2.1 shows the average number of detected SOBHBs, and the number of SOBHBs for which $f_{\rm Edd}$ can be measured within a given precision. The results are obtained by averaging the Fisher matrix over sky position and source inclination (while neglecting, as already mentioned, the LISA constellation's motion), for different injected values of $f_{\rm Edd}$. Our results for the total number of detected events are consistent with [223, 215].

In particular, for the *LISA+Earth* case and a 10 yr mission, super-Eddington accretion $f_{\rm Edd} \approx 10$ can be measured within 50% precision in about 15% of the total detectable events (≈ 200), while a measurement within 10% is only possible in $\sim 2\%$ of the events. Note that the statistical errors scale approximately linearly with $f_{\rm Edd}$. Therefore, when

injecting a lower accretion rate the number of events for which accretion is measurable is significantly smaller. For example, $f_{\rm Edd} = 1$ is marginally detectable in $\lesssim 1$ event in the most optimistic scenario, whereas smaller values of the accretion rates are not measurable.

As expected, a multiband observation improves the measurements of a negative-PN term, including the -4PN term due to accretion: the event rates for the *LISA-only* case are thus smaller by a factor of a few relative to the *LISA+Earth* case.

2.2.4 Prospects for multimessenger astronomy and conclusions

In [63] we also performed a more refined Markov Chain Monte Carlo (MCMC) analysis for the best candidate events. According to the MCMC analysis, both SOBHBs and IMBHBs can be localized in the sky to within the fields of view of X-ray and radio instruments such as the Athena Wide Field Imager (WFI) and SKA, $\Delta\Omega_{\rm Athena} = 0.4\,{\rm deg}^2$, $\Delta\Omega_{\rm SKA} = 0.5\,{\rm deg}^2$ [3, 177]. This will allow the relevant region of the sky to be covered in a single viewing[4], thus potentially allowing for the coincident detection of an X-ray and/or radio counterpart to strongly-accreting black hole binaries. Even if the sky localization was biased, as might be the case for IMBHBs, we estimated that the true position would still fall inside the field of view of the instruments. In the following, we compute the X-ray and radio emission of the binaries, and estimate the necessary integration time for detection by single instrument viewing.

We start by estimating the X-ray flux. For this purpose, we assume that the accretion process has radiative efficiency $\eta = 0.1$ (which is good approximation at $f_{\rm Edd} < 1$), and that only a fraction $\eta_X = 0.1$ of the electromagnetic radiation is emitted in X-rays ("bolometric correction"). We find the X-ray flux from a single accreting black hole to be

$$F_X \simeq 1 \times 10^{-13} f_{\rm Edd} \left(\frac{M}{M_\odot}\right)\left(\frac{\rm Mpc}{d_L}\right)^2 {\rm erg\,cm^{-2}\,s^{-1}}\,. \tag{2.23}$$

This should be compared with the flux sensitivity of the Athena WFI for a given integration time, $T_{\rm int}$. Following [174], Athena's flux sensitivity for a 5σ detection is

$$F_X^{\rm Athena} = 1 \times 10^{-15} \left(\frac{10^3\,{\rm s}}{T_{\rm int}}\right)^{1/2} {\rm erg\,cm^{-2}\,s^{-1}}\,. \tag{2.24}$$

[4] In some cases, the correlation between the sky position angles can imprint an asymmetric shape to the localized region, which might therefore partially fall outside the field of view. However, this would still only require $\mathcal{O}(1)$ viewings.

The minimum integration time for a binary where only one black hole is emitting is then given by

$$T_{\rm int} \simeq 8 \times 10^{-2}\, f_{\rm Edd}^{-2} \left(\frac{d_L}{\rm Mpc}\right)^4 \left(\frac{M_\odot}{M}\right)^2 {\rm s}\,. \tag{2.25}$$

Note that if the two black holes have similar mass and are both accreting, the cumulative flux is given by twice the value in Eq. (2.23) and therefore the minimum integration time is one fourth of that in Eq. (2.25).

For the best-candidate SOBHB event in our synthetic astrophysical catalogues, the required exposure time is $T_{\rm int} \gtrsim 1 \times 10^6\, f_{\rm Edd}^{-2}\,{\rm s}$. Thus, even if we were to assume $f_{\rm Edd} \approx 1$, the integration time would have to be of several days. Assuming super-Eddington accretion $f_{\rm Edd} > 1$ is unlikely to help as the radiative efficiency is expected to be considerably lower than our assumed $\eta = 0.1$, *i.e.*, the bolometric luminosity is not expected to significantly exceed the Eddington luminosity [216, 204, 211]. Moreover, as previously discussed, high accretion rates in SOBHBs likely require environments with large gas densities, whose optical thickness further reduces the chances of an electromagnetic detection. For the considered IMBHB systems, the required integration time is between 24 and 2 hours for Eddington-level accretion, for the light and heavy systems, respectively. This estimate suggests that detection of X-ray counterparts will be possible for highly-accreting IMBHBs.

A binary system in external magnetic fields may also launch dual radio jets, which get amplified by the coalescence [195] relative to similar jets observed in isolated black holes [220]. See also [183] for simulations that yield ∼100 times larger (though less collimated) fluxes than [195]. Assuming a fiducial value $\eta = 0.1$ for the radiative efficiency of the process and $\eta_{\rm radio} = 0.1$ for the fraction of emission in the radio band, the corresponding peak flux[5] is [195, 222]

$$F_{\rm flare} \simeq 2 \times 10^{-13}\, f_{\rm Edd}\, q^2 \left(\frac{D_L}{\rm Mpc}\right)^{-2} \left(\frac{M}{M_\odot}\right) \times {\rm erg\,cm^{-2}\,s^{-1}}\,, \tag{2.26}$$

where $q \leq 1$ is the mass ratio. The flare flux can then be compared with the SKA-mid sensitivity in the phase 1 implementation. The required sensitivity at frequency $\nu_{\rm SKA}$ for SKA,

$$F_{\rm SKA} = 5 \times 10^{-16} \left(\frac{10^{-2}\,{\rm s}}{T_{\rm obs}}\right)^{1/2} \left(\frac{\nu_{\rm SKA}}{\rm GHz}\right) {\rm erg\,cm^{-2}\,s^{-1}}\,, \tag{2.27}$$

is reached for an observation time $T_{\rm obs} \sim 10^{-2}\,{\rm s}$ for our best SOBHB event. The observation time should be smaller than the duration of the merger (*i.e.*, the duration of the flare) for

[5]The peak sensitivity is reached when the orbital velocity is equal to that of the innermost circular orbit.

the system [220], $T_{\rm flare} \sim 25\ \frac{M}{100 M_\odot}$ ms. This condition is not satisfied for SOBHBs. There is however the concrete possibility to detect a signal in the radio band for IMBHBs, for which for the light and heavy systems $T_{\rm obs} \approx 40 - 4$ ms $< T_{\rm flare}$. The performance of full SKA should improve by an order of magnitude with respect to Eq. (2.27), reducing the required integration time by a factor 100.

In conclusion, SOBHBs and IMBHBs will provide the opportunity to measure the effect of accretion, which might affect the GW waveform at low frequencies. Our analysis suggests that a multiband detection with LISA and a ground-based detector will be able to measure the accretion parameter of strongly-accreting SOBHBs to within 50% precision for a few events. For these systems, neglecting accretion in the waveform template might lead to biases in the recovered binary parameters. These biases can be alleviated by an accurate measurement of the time of coalescence by a ground-base detector.

IMBHBs in the local universe, if they exist as LISA sources, might also provide very accurate measurements of the accretion rate. Overall, for these systems the effect of accretion should be included in the waveform to avoid bias in the intrinsic binary parameters.

Finally, accretion does not affect sky localization by LISA for SOBHBs and it impacts that of IMBHBs only mildly. In both cases, the measurement errors are typically well within Athena and SKA's fields of view. Furthermore, the X-ray flux expected from strongly-accreting binaries is comparable with Athena's sensitivity and is well above the sensitivity of future missions such as Lynx [4]. Likewise, in the case of jets the radio signal from IMBHBs could be detectable by SKA. Our analysis shows that the simultaneous operation of Athena/SKA and LISA would therefore provide the thrilling opportunity to detect the electromagnetic counterpart of highly accreting black hole binaries.

2.3 Dynamical friction

Gas surrounding a black hole binary, besides being accreted, can also exert a gravitational influence over the moving bodies, an effect known as dynamical friction (DF).

Consider a black hole binary immersed in gas of density ρ. Assuming that the binary's center of mass (CoM) is approximately comoving with the gas, dynamical friction exerts a drag force on each black hole in the direction of the black hole velocity $\vec{v}_i$ in the CoM frame,

$$F_{{\rm DF},i} = 4\pi\rho (G m_i)^2 I(r_i, v_i)/v_i^2\,, \tag{2.28}$$

at Newtonian order, where r_i is the distance of the black hole from the CoM. We assume that the black holes' orbital velocity is much larger than the speed of sound of the gas:

$v_i \gg c_s$. This is supported by the fact that v_i is relativistic when the binary is in the LISA band. We use the analytic expression of the "Coulomb logarithm" $I(r, v)$ at high Mach numbers $\Upsilon_i = v_i/c_s$ provided in [141] for a single perturber in circular orbit in a gas,

$$I(r_i, v_i) = \log\left(\frac{r_i}{r_{\rm min}(0.11\Upsilon_i + 1.65)}\right) , \tag{2.29}$$

where $r_{\rm rim} = 2Gm_i/c^2$ is the smallest scale in the problem, in this case set by the black hole radius (but results depend only mildly on the choice of $r_{\rm min}$). This expression was validated against simulations up to $\Upsilon = 8$, but we extrapolate further taking the limit of large Mach numbers and keeping only the leading term in this expansion (see also [143]), $I(r_i, v_i) \simeq \log\left(r_i/(r_{\rm min}0.11\Upsilon)\right)$. Following [141] (see also [192, 33, 162]), we only include the effect of the wake created by each black hole on itself, and neglect the companion's [142]. For $f \lessapprox 0.3\,{\rm Hz}$ this is a good approximation, since the orbital separation of a typical stellar- and intermediate-mass black hole binary in the LISA band is larger than the wake's size.

We consider here, as an example, the AGN disk claimed to have hosted the GW event GW190521 [10, 12, 118]. From this association, Graham et al. [118] find an AGN disk aspect ratio (height to galactocentric radius) $H/a \sim 0.01$, and gas density $\rho \sim 10^{-10}$ g/cm^3. We assume here that the speed of sound is given by $c_s \approx v_{\rm orb}(H/a) \simeq 50$ km/s [112], where $v_{\rm orb}$ is the speed of the orbit around the supermassive black hole (SMBH) at the center of the AGN assuming that the binary is in a migration trap at $\simeq 700GM_{\rm SMBH}/c^2$, with $M_{\rm SMBH} \simeq 10^{8-9}M_\odot$.

In absence of dynamical friction, the orbital energy of the binary would only decrease as a result of GW emission. If we take into account the energy lost to the gas through dynamical friction, we obtain an equation for the orbital angular velocity as a function of time,

$$\dot{E}_{\rm orb} = P_{\rm GW} + F_{{\rm DF},1}v_1 + F_{{\rm DF},2}v_2 \,, \tag{2.30}$$

where $E_{\rm orb}$ is the binary orbital energy and $P_{\rm GW} = 32/5\, M m_1^2 m_2^2\, (GM/\omega^2)^{-5/3}$ is the power emitted in GWs. Similarly to the case of accretion discussed in Section 2.2, we can assume that gravitational wave emission and DF are adiabatic processes, and solve Eq. (2.30) perturbatively to first order in the subdominant effect. This allows us to compute $\omega_{\rm DF}(t)$, $t_{\rm DF}(f)$ and the GW phase modification. In this approximation, the dynamical friction-induced phase correction first enters at -5.5PN order:

$$\phi_{\rm DF} \simeq -\rho\frac{25\pi(3\nu-1)\mathcal{M}^2(1+z)^2}{739328\,\nu^2}\,\gamma_{\rm DF}\left[\pi f\mathcal{M}(1+z)\right]^{-16/3} , \tag{2.31}$$

with $\gamma_{\rm DF} = -247\log\left(f/f_{\rm DF}\right) - 39 + 304\log(20) + 38\log\left(3125/8\right)$ and $f_{\rm DF} = c_s/[22\pi(m_1+m_2)]$, being $\nu = m_1m_2/(m_1+m_2)^2$ the symmetric mass ratio.

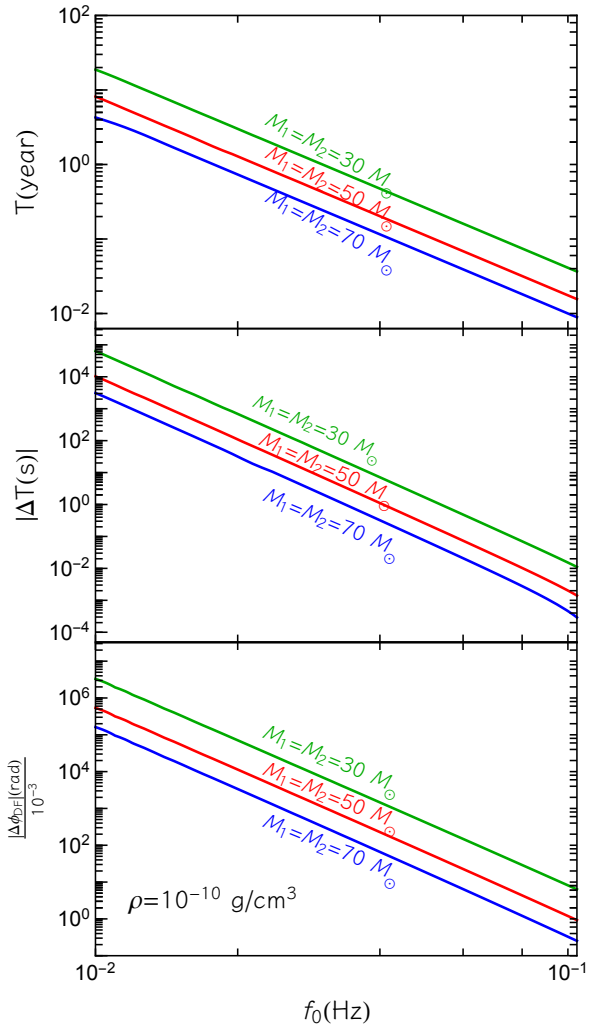

Figure 2.4: Time needed to enter the band of terrestrial detectors neglecting accretion (top), time difference caused by dynamical friction (middle), and GW phase difference induced by friction (bottom), as functions of the initial GW frequency for three equal-mass SOBHBs. We choose $\rho = 10^{-10}$ g/cm^3 as a reference, since the time and phase differences scale linearly with ρ. The final frequency is always $f = 1$ Hz. The phase difference is computed as the difference in the term (2.31) between the initial and final frequencies.

The effect of dynamical friction on the GW signal can again be estimated by computing the delay and the GW phase shift induced by the effect. This is done in Figure 2.4, where the gas density is chosen to match the one inferred from the claimed counterpart

to GW190521. Time differences $\Delta T > 10\,\mathrm{s}$ and phase differences $\gtrsim 1$ rad are again deemed large enough to be detectable. For dynamical friction, inspired by GW190521, we also considered higher system masses. From Figure 2.4, we see that gas densities above $\sim 10^{-10}$ g/cm^3 would be marginally detectable for systems entering the band of ground-based detectors in a year or more. In [224] we also performed a more detailed Fisher matrix exploration of this effect across the system parameters consistent with GW190521, confirming that these densities could be constrained at percent level. We therefore conclude that effect of realistic levels of DF are stronger and easier to detect than reasonable levels of accretion (Eddington level or below). In [224] we also performed an MCMC analysis for a single system with the effects of mass accretion, dynamical friction and a peculiar acceleration all present at the same time, and found that the -4PN (*i.e.*, accretion and peculiar acceleration) and -5.5PN (*i.e.*, DF) terms could be measured separately thanks to their distinct frequency dependence. The MCMC analysis also confirmed that percent level precision on densities of the order of 10^{-10} g/cm^3 could be achieved with a multiband strategy.

2.4 Mass transfer from a stellar companion

Our last topic in this chapter is again a matter-dominated gravitational wave source involving a black hole. In the case of white dwarf–black hole binaries, however, the black hole is not accreting gas from its surroundings, but rather from the binary companion itself.

2.4.1 Evolution of mass transferring white dwarf-black hole binaries

We consider white dwarf-black hole binaries (WDBH) binaries on a circular orbit with separation a. We model their evolution from the onset of mass transfer, when the WD overfills its Roche lobe. Our treatment follows that of [171], with appropriate adjustments for the BH component. We use the zero-temperature mass-radius relation of [228] for the WD[6]. We define the total mass $M = m_{\rm BH} + m_{\rm WD}$ and the mass ratio $q = m_{\rm WD}/m_{\rm BH} \leq 1$.

[6]Note that the accretion disk surrounding the BH can heat the WD. We will discuss this caveat further in the conclusions.

Mass transfer

The overfill factor indicates by how much the donor overfills its Roche lobe, $\Delta = R_{\rm WD} - R_L$. Mass transfer occurs when $\Delta > 0$ and increases monotonically with the overfill. We use the adiabatic approximation of [171] (see also [235]):

$$\dot{M}_{\rm WD} = -F(m_{\rm BH}, m_{\rm WD}, a, R_{\rm WD})\Delta^3 \,. \tag{2.32}$$

See [171] for the definition of F. We assume an accretion disk forms around the BH and that matter is transferred from the innermost stable circular orbit (ISCO) at a radius $R_{\rm ISCO}$ [75]. We account for the limited efficiency of the BH to accrete by setting:

$$\dot{m}_{\rm BH} = \min\left(-\dot{m}_{WD}\ \epsilon_{\rm ISCO}, \dot{m}_{\rm Edd}(m_{\rm BH})\right), \tag{2.33}$$

where $\dot{m}_{\rm Edd} = 2.2\times10^{-8} m_{\rm BH}$ year^{-1} is the Eddington accretion rate and $\epsilon_{\rm ISCO}$ is the specific mass-energy at the ISCO [75]. Therefore mass is not necessarily conserved, accounting for possible loss through winds.

Orbital separation

We assume that the variation of total angular momentum is due to GW emission and loss of matter:

$$\dot{J}_{\rm orb} + \dot{J}_{\rm BH} + \dot{J}_{\rm WD} = -\dot{J}_{\rm GW} - \dot{J}_{\rm loss}, \tag{2.34}$$

with $\dot{J}_{\rm GW} = \frac{32}{5}\frac{G^3}{c^5}\frac{m_{\rm BH} m_{\rm WD} M}{a^4}\, J_{\rm orb}$. Following [227], we assume isotropic re-emission and take $\dot{J}_{\rm loss} = -q\frac{\dot{M}}{M} J_{\rm orb}$. We neglect the angular momentum of the accretion disk surrounding the BH, assuming that $M_{\rm disk} \ll M_{\rm BH}$ throughout the evolution.

We assume that the WD is tidally locked. This is justified in low-mass-ratio systems such as WDBH binaries, since the synchronization time-scale decreases as the mass ratio squared, $\tau_{\rm sync} \sim q^2$ [62]. Moreover, disk accretion can also contribute to synchronizing the star rotation with the orbit [243]. The angular momentum of the donor can then be written as $J_{\rm WD} = I_{\rm WD}\Omega$, Ω being the orbital angular frequency and $I_{\rm WD} = k m_{\rm WD} R_{\rm WD}^2$ the momentum of inertia of the donor. The factor k is a function of the WD mass, for which we use the fit provided in [171]. Using Kepler's law, the variation in angular momentum of the donor is:

$$\dot{J}_{\rm WD} = I_{\rm WD}\Omega\left(\lambda\frac{\dot{m}_{\rm WD}}{m_{\rm WD}} - \frac{3}{2}\frac{\dot{a}}{a} + \frac{\dot{m}_{\rm BH} + \dot{m}_{\rm WD}}{m_{\rm WD}}\frac{1}{2\,(1+1/q)}\right), \tag{2.35}$$

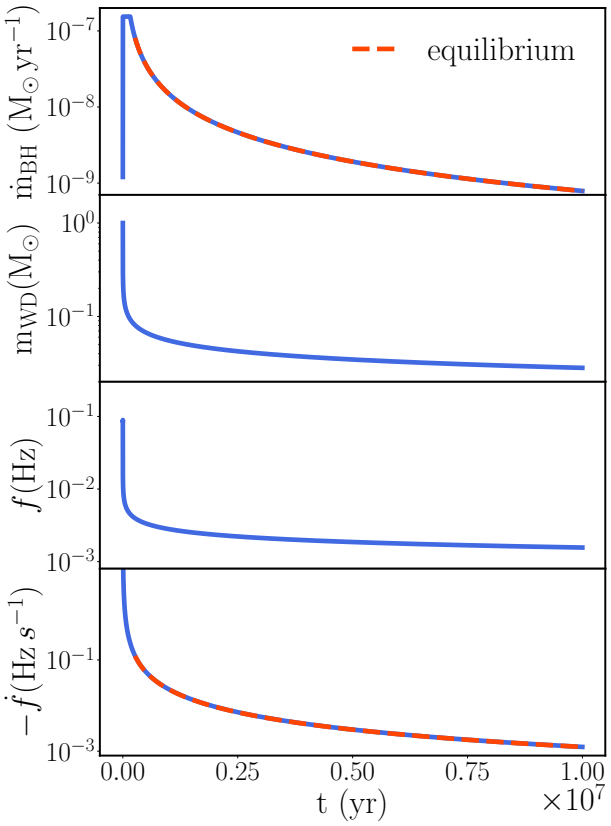

Figure 2.5: Evolution of the mass accretion rate, WD mass, GW frequency and its first derivative. The system has masses $m_{\rm WD} = 1\,M_\odot$ and $m_{\rm BH} = 7\,M_\odot$ at the time of first Roche lobe filling. The overlaid orange dashed line is the equilibrium solution described in Appendix A.

where $\lambda = 1+2\frac{{\rm d}\log R_{\rm WD}}{{\rm d}\log m_{\rm WD}}+\frac{{\rm d}\log k}{{\rm d}\log m_{\rm WD}}$. Note that the variation of the donor angular momentum was not included in the treatment of [171].

We assume no tidal torque acts on the BH, so its angular momentum varies only as a result of the matter accreted at $R_{\rm ISCO}$,

$$\dot{J}_{\rm BH} = j_{\rm ISCO}\dot{m}_{\rm BH}, \tag{2.36}$$

where $j_{\rm ISCO}$ is the specific angular momentum at the ISCO [75].

The equation for the orbital separation of the white dwarf–black hole binary can be derived from Eqs. (2.34), (2.35) and (2.36) and reads

$$\frac{\dot{a}}{2a} = -\frac{1}{1-3(1+q)kr_2^2}\left[\frac{\dot{J}_{\rm GW}}{J_{\rm orb}} + \left(1 - \frac{q}{2(1+q)} + \frac{1}{2}qkr_2^2 + (1+q)\lambda kr_2^2\right)\frac{\dot{M}_{\rm WD}}{M_{\rm WD}} + \left(q - \frac{q}{2(1+q)} + \frac{1}{2}qkr_2^2 + j_{\rm GR}\sqrt{(1+q)r_{\rm ISCO}}\right)\frac{\dot{M}_{\rm BH}}{M_{\rm WD}}\right], \quad (2.37)$$

where $r_i = R_i/a$.

Overfill and black hole spin

We evolve the over-fill factor according to

$$\dot{\Delta} = R_{\rm WD}\left[\left(\zeta_{\rm WD} - \zeta_{r_L}\right)\frac{\dot{m}_{\rm WD}}{m_{\rm WD}} - \frac{\dot{a}}{a}\right], \quad (2.38)$$

where $\zeta_{\rm WD} = \frac{{\rm d}\log R_{\rm WD}}{{\rm d}\log m_{\rm WD}}$ and $\zeta_{r_L} = \frac{{\rm d}\log R_L/a}{{\rm d}\log m_{\rm WD}}$ can be derived using Eggleton's approximation for the mass-radius relationship of cold WDs and Eggleton's Roche lobe fitting formula [101], respectively.

The angular momentum of the BH can be written in terms of the dimensionless spin χ,

$$J_{\rm BH} = \frac{G}{c}m_{\rm BH}^2\chi\,. \quad (2.39)$$

The accreting BH will spin up according to Eq. (2.36), from which we obtain

$$\dot{\chi} = \left(\frac{c}{G}\frac{j_{\rm ISCO}}{m_{\rm BH}} - 2\chi\right)\frac{\dot{m}_{\rm BH}}{m_{\rm BH}}\,. \quad (2.40)$$

The evolution of the BH spin is not our main focus and has little effect on the overall evolution of the binary. We therefore neglect for simplicity other factors affecting the spin evolution, such as radiation emitted by the accretion disk and fix the initial BH spin to $\chi = 0.1$.

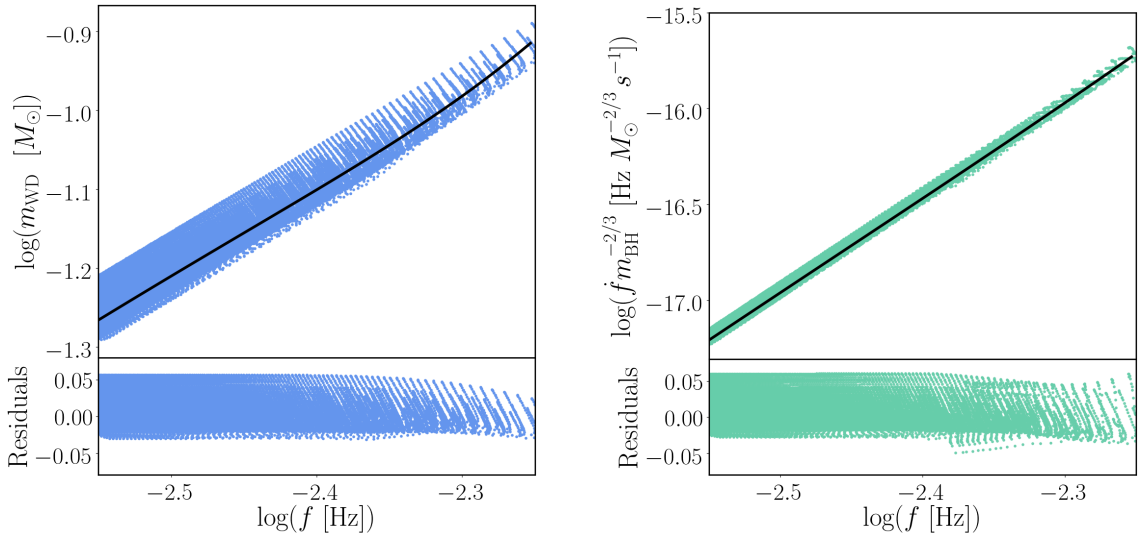

Figure 2.6: Evolutionary tracks of 400 WDBH binaries and their polynomial fits (black line). We focus on frequencies relevant to LISA.

2.4.2 Evolutionary tracks relations

We numerically integrate equations (2.32), (2.33), (2.34), (2.38) and (2.40), starting from the onset of mass transfer. The long term evolution of a typical WDBH binary is shown in Figure 2.5. The cap in the BH accretion rate on the top panel is due to accretion reaching the Eddington limit. As expected for mass-transfer dominated systems where the accretor is much more massive than the donor, the binary outspirals, giving a negative $\dot{f}$.

Mass transfer proceeds rapidly at first, but quickly settles into an equilibrium rate. Equilibrium is attained when the increase in the Roche lobe matches the one in the WD radius. Thus, we obtain the equilibrium mass transfer rate by setting the right hand side (rhs) of Eq. (2.38) to 0, see Appendix A.

Across parameter space, the mass of the WD follows an evolutionary track as a function of the GW frequency, which is approximately independent of the accretor mass and the initial conditions, as displayed in Figure 2.6, left panel. We span initial WD masses between $[0.2, 1.2]\,M_\odot$, initial BH masses in the range $[3, 20]\,M_\odot$ and only keep points from the equilibrium stage. These tracks can be compared with the ones traced by WD accreting binaries in [57]. Our WDBH tracks follow a slightly different trajectory and show a more

		HF			*LF*		
		$\tilde{m}_{\rm BH}$	$\tilde{m}_{\rm WD}$	$\tilde{D}_L$	$\tilde{m}_{\rm BH}$	$\tilde{m}_{\rm WD}$	$\tilde{D}_L$
100%	Fit	$0.99^{+0.01}_{-0.01}$	$0.99^{+5.7\times10^{-8}}_{-5.8\times10^{-8}}$	$1.05^{+0.11}_{-0.14}$	$1.04^{+0.40}_{-0.36}$	$0.97^{+2.8\times10^{-7}}_{-2.8\times10^{-7}}$	$0.98^{+0.35}_{-0.29}$
	Full	$1.01^{+0.08}_{-0.04}$	$0.99^{+0.02}_{-0.04}$	$1.06^{+0.11}_{-0.15}$	$1.03{+}0.44_{-0.38}$	$0.98^{+0.04}_{-0.05}$	$0.98^{+0.35}_{-0.29}$
75%	Fit	$0.99^{+0.01}_{-0.01}$	$0.99^{+7.7\times10^{-8}}_{-7.8\times10^{-8}}$	$1.39^{+0.16}_{-0.20}$	$1.05^{+0.55}_{-0.47}$	$0.97^{+3.8\times10^{-7}}_{-3.8\times10^{-7}}$	$1.28^{+0.59}_{-0.47}$
	Full	$1.01^{+0.08}_{-0.04}$	$0.99^{+0.02}_{-0.04}$	$1.05^{+0.13}_{-0.16}$	$1.03^{+0.61}_{-0.49}$	$0.98^{+0.05}_{-0.05}$	$0.96^{+0.44}_{-0.35}$

Table 2.2: Uncertainties on individual masses and distances normalized to the injected values, obtained with the fit to the global evolutionary tracks relations (Fit) and with the full results of numerical simulations (Full). The GW frequency f and $\dot{f}$ are measured within 5×10^{-7} Hz and 5×10^{-18} Hz s^{-1} for the *HF* system, assuming a duty cycle of 75%. These measurements are an order of magnitude worse for the *LF* system.

pronounced dependence on the accretor mass, resulting in a larger spread in the tracks (and hence fit residuals).

The absence of tidal interactions yields an additional relation between $\dot{f}m_{\rm BH}^{-2/3}$ and f. We show this relation in Figure 2.6, right panel. Once again, the relation is roughly independent of the accretor mass and initial conditions. In Appendix A we explain how this relation can be derived from the equilibrium solution.

We fit both evolutionary track relations with a quartic polynomial

$$\log(y) = \sum_{i=0}^{n} a_i \log(f[Hz])^i \,, \tag{2.41}$$

see Figure 2.6. The fit coefficients are listed in Appendix B.

2.4.3 Parameter estimation with LISA

In the case of almost monochromatic sources such as WDBH and double WD binaries, the two GW polarizations take the simple form:

$$h_+ = A_0 \frac{1}{2}\left(1+\cos^2(\iota)\right)\cos\Big(\phi_0 + 2\pi f t + \pi \dot{f} t^2\Big), \tag{2.42}$$

$$h_\times = A_0 \cos(\iota)\sin\Big(\phi_0 + 2\pi f t + \pi \dot{f} t^2\Big), \tag{2.43}$$

where $A_0 = \frac{\mathcal{M}_c}{D_L}(\pi \mathcal{M} f)^{2/3}$ is the amplitude of the signal, $\mathcal{M} = m_{\rm BH}^3 m_{\rm WD}^3/M$ is the chirp mass of the binary, ι is the inclination of the binary with respect to the line of sight, and ϕ_0 is the initial phase. Thus, GW observations provide us A_0, f and $\dot{f}$ and we cannot infer the individual masses without further assumptions. In order to assess how the universal relations we derived can be combined with LISA measurements, we consider an accreting WDBH system at two different stages of its evolution:

- "high frequency" (*HF*): $m_{\rm BH} = 7.02 M_\odot$, $m_{\rm WD} = 0.10\ M_\odot$, $f = 5$ mHz, $\dot{f} = -3.8 \times 10^{-16}$ Hz s^{-1};
- "low frequency" (*LF*): $m_{\rm BH} = 7.02 M_\odot$, $m_{\rm WD} = 0.06\ M_\odot$, $f = 3$ mHz, $\dot{f} = -3.2 \times 10^{-17}$ Hz s^{-1};

We compute LISA's response following [87, 209] to generate mock data and perform a full Bayesian analysis to infer the posterior distribution of the parameters of the source. For the noise level, we use the SciRdv1 curve [158] including a confusion noise due to the galactic foreground in addition to the instrument noise [166]. The parameter estimation is performed with the nested sampling algorithm `Multinest` [108]. We assume a mission duration of 6 years and two values of the duty cycle: 100% and 75%. We set the distance to $D_L = 10$ kpc and simulate the effect of a reduced duty cycle by placing the source further. For almost monochromatic sources, the angles essentially affect the signal to noise ratio (SNR) and have little impact on our analysis. For a duty cycle of 100%, the *HF* and *LF* systems have SNRs of 91 and 26 respectively. Systems at frequencies below 3 mHz, although more numerous, have little chance of being detected due to the galactic foreground. With a duty cycle of 75%, f and $\dot{f}$ are measured within 5×10^{-7} Hz and 5×10^{-18} Hz.s^{-1} for the *HF* system and an order of magnitude worse for the *LF* system.

In Table 2.2 we report the estimates of the binary masses (normalized to the injected values) directly using the fits to the evolutionary tracks of Figure 2.6. We can use these results to infer the chirp mass and, from the measurement of A_0, the distance to the source. We find a reasonable agreement with the injected values (within 5%). However for the *HF* system, the injected values lie outside the 90% confidence intervals. This is because the systematics of the model dominate over the statistical uncertainty. In particular, the very narrow range for $M_{\rm WD}$ is due to the extremely good measurement of f. To correct for this, we estimate numerically the values of α_1 and α_2 that best align the evolutionary tracks, $m_{\rm WD}\, m_{\rm BH}^{-\alpha_1}$ and $\dot{f}_{\rm WD}\, m_{\rm BH}^{-2/3-\alpha_2}$ as functions of f. The exponents α_1 and α_2 are frequency dependent and are determined for each system in the frequency range of observation. We then convolve LISA posteriors with the aligned tracks to infer $m_{\rm BH}$ and $m_{\rm WD}$.

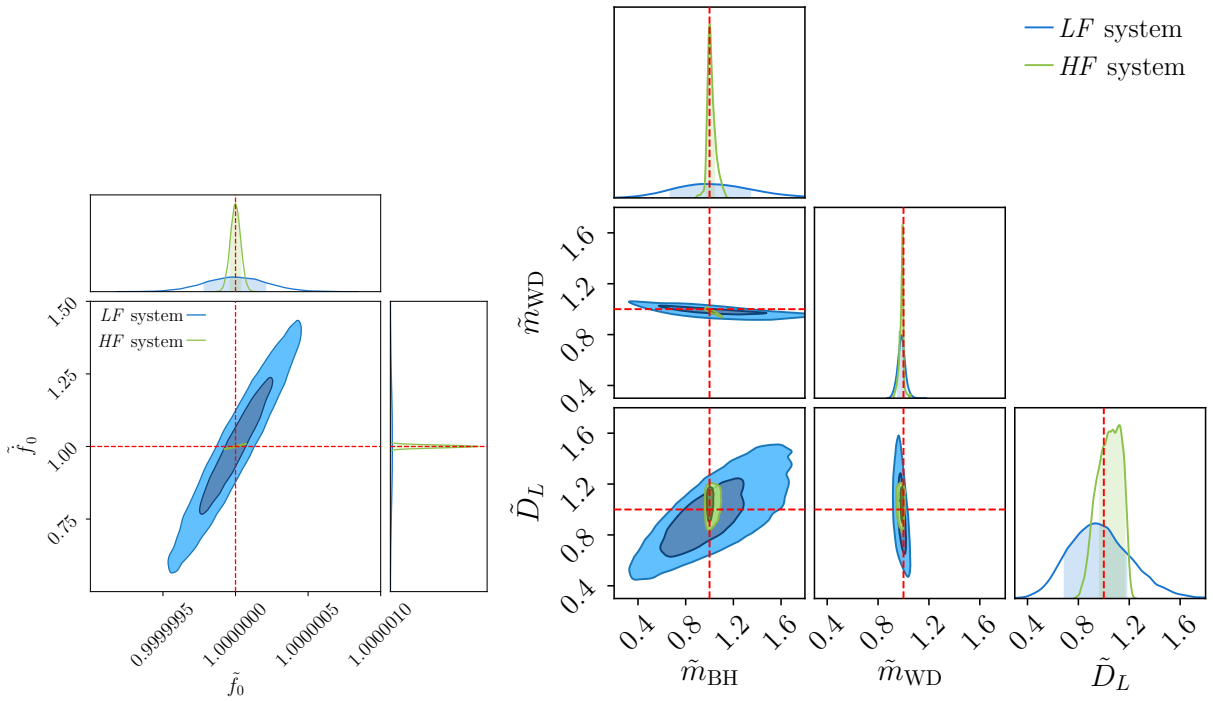

Figure 2.7: Left: Posterior distributions of the GW frequency and its first derivative normalized to the injected values. We show posteriors for the high (HF) and low frequency (LF) systems, at 75% duty cycle. The contours indicate the 50 and 90% confidence regions and the dashed lines represent the true values (equal to 1 in our normalization). Right: Posterior distributions for binary masses and luminosity distance, obtained with the rescaled universal relations, as described in Sec. 2.4.3.

In Figure 2.7, we show how the measurement of f and $\dot{f}$ together with this procedure translates into a measurement of the WD and BH masses for the two systems assuming a 75% duty cycle. Table. 2.2 also shows the improvement as compared to fit-based measurements and the very good agreement between the injected and the inferred values obtained with this procedure. $M_{\rm BH}$ is less well constrained than $M_{\rm WD}$ because it relies on the measurement of $\dot{f}$. The measurement is worse for the *LF* system due to the lower value of $\dot{f}$ which results in it being measured not as well during the 6 year mission. We note that the results are less affected by a reduced duty cycle. Finally, even in the worst scenario the uncertainty on $M_{\rm BH}$ is sufficiently small to unambiguously identify the accretor as a BH.

2.4.4 Conclusions

Mass-transferring binaries containing a BH and a WD have been an elusive target, despite being predicted by population synthesis models. In this Chapter we show that combining LISA observations with semi-analytic evolution models provides an estimate of the masses of both binary components as well as the distance to the source, which is information not usually accessible from galactic binary GW observations.

WDBH binaries are potential sources of electromagnetic radiation, in particular X-ray emission. The *HF* and *LF* systems considered in this work would have respectively X-ray luminosity of $9 \times 10^{38}\,\mathrm{erg\,s^{-1}}$ and $1 \times 10^{38}\,\mathrm{erg\,s^{-1}}$ for radiative efficiency of 0.1, well within the capabilities of current facilities. The fact that we are yet to convincingly identify WDBH binaries among X-ray sources could be explained by the lower rates of these systems, and the difficulty to classify the binary components from electromagnetic emission alone. GW observations such as the ones described in this work, on the other hand, could unequivocally identify the BH companion. The very good localization of the source by LISA, $\mathcal{O}(1\,\mathrm{deg}^2)$, could then provide the opportunity to observe an electromagnetic counterpart. In future work, we will explore the potential synergy between LISA and future electromagnetic surveys (Athena+, Square Kilometer Array) and the detectability of both GW and electromagnetic emission in the Milky Way and nearby galaxies.

To detect and learn the most from these systems with LISA, more detailed modeling will be crucial. This work did not take into account, for instance, the potentially disruptive effect of accretion winds on the accretion stream itself, and its potential variability on short timescales. Moreover, the use of Eggleton's approximation for the Roche lobe radius, which was derived for stars made of incompressible fluids, could introduce a bias in our result. Such bias is hard to quantify because the true relation is unknown. However, our methodology is robust to changes in the Roche lobe radius relation, and we expect our main finding to hold, *i.e.*, LISA could be the first observatory to unambiguously identify WDBH binaries.

Assuming a simple black body law for the BH and the WD, we estimate that emission from the BH disk could heat up the WD to $\mathcal{O}(10^5)$ K. Such low temperatures, if interpreted as core temperatures, have very little impact on the mass-radius relation [37] and therefore the cold WD assumption remains a good approximation. A caveat is that the results of [37] were obtained for cooling sequences of isolated WDs. More simulations of heated WDs as in [200] could provide further insight on the effect of illumination on the evolution of WDBH binaries. WDs with masses lower then the ones considered in this work might also exhibit a stronger dependence on the temperature, see, *e.g.*, [91]. Recent hydrodynamical simulations [78] have suggested that mass tranfer in WDBH binaries could be unstable

above WD masses 0.2 $M_\odot$, leading the binary to merge. It would be interesting to extend our model to lighter WDs, in a mass range where finite temperature effects might become relevant.

Finally, we checked that the presence of tidal torques would not affect our results significantly for small synchronization timescales ($\tau \lesssim 100$ yrs). This study could therefore apply to broader classes of galactic binaries.

Chapter 3

Black hole ringdown

3.1 The problem: why so linear?

The ringdown is the final phase of a black hole binary merger, beginning (approximately) at the formation of the binary's common horizon. During the first few dynamical times, the merger product is extremely deformed. The ringdown is the process of relaxation of this deformed object through the emission of gravitational waves.

The response of a black hole to an external perturbation, if we exclude very early and late times, is characterized in general relativity by a spectrum of ringing, decaying modes, known as quasi normal modes (QNMs). More specifically, QNMs are solutions of the linear perturbation equations with ingoing and outgoing (in asymptotically flat spacetimes) conditions at the horizon and at infinity, respectively. These boundary conditions imply that QNMs are discrete modes with complex frequencies,

$$h_{\rm QNM} \sim e^{-i\omega t}, \quad \omega = \omega_{\rm R} + i\omega_{\rm I}\,, \tag{3.1}$$

where h is the metric perturbation, although similar arguments apply to perturbations of other fields. This can be understood in analogy to quantum mechanics, where an outgoing probability flux at one or more boundaries implies that the total probability inside the system must decay over time. This decay is associated with the frequency of the modes acquiring an imaginary part, corresponding to the inverse decay time of the mode.

The QNM frequencies of a black hole are identified by their angular quantum numbers l, $|m| \leq l$ and an overtone number n, so that $n = 0$ corresponds to the least rapidly decaying mode (the fundamental mode). QNMs do not form, in general, a complete basis, because

the system of linearized equations and boundary conditions do not define a self-adjoint problem. QNMs were however recently found to be orthogonal under a specific symmetric bilinear form [121]. For a more complete review of the topic, see [41] or [189].

Because QNMs are a property of the linearized general relativistic equations for the gravitational field, and because they do not form a complete basis, we might have expected a sum of QNMs to provide only a poor fit to the gravitational wave signal very close to merger. The binary merger, roughly corresponding to the peak in the luminosity of the gravitational wave signal, is the most nonlinear stage of the evolution of the binary, and requires numerical relativity simulations for an accurate description. It was suggested early on that QNMs could however provide accurate fits very early in the ringdown [153], and renewed interest in this question was stirred in 2019 by Giesler et al. [116].

Fig. 3.1 and Table 3.1 summarize the findings of [116]. The ringdown signal of a numerical simulation from the SXS catalog [2, 55] is modeled with a finite sum of QNMs with angular numbers $l = 2$, $m = 2$ and overtone number up to $N = 7$, *i.e.*, the metric perturbation

$$h_{2,2} = \sum_{n=0}^{N-1} A_n e^{i\phi_n} e^{-i\omega_n (t - t_{\text{peak}})}. \tag{3.2}$$

Here ω_n are the QNM frequencies predicted by general relativity for the mass and spin of the remnant, while A_n and ϕ_n are the amplitudes and phases determined by a least squares fit. The residuals of the fit, shown in Fig. 3.1, are small, but above the numerical noise (measured as the residuals of two simulations with different resolution). This indicates a good fit and supports the absence of over-fitting, or fitting of numerical noise.

Reference [116] shows that an increasing number of QNMs fits the data better at earlier times, with the $N = 7$ model (used in Fig. 3.1) fitting the full ringdown after the peak luminosity of the GW signal. These results were later confirmed [46] and extended to counter-rotating modes ($\omega_R < 0$) [93] and other harmonics [86], and a similar analysis was recently performed at the black hole horizon (rather than at infinity) [187].

The implications of these analyses are still being debated. These results might indicate either that linear theory is an excellent approximation even very close to the time of merger, or that QNMs form a sufficiently good basis that a large enough combination of these modes can fit even nonlinear features. Despite some attempts to rule out the latter possibility, the evidence is still not conclusive [187][1].

[1] Giesler et al. [116] as well as Baibhav et al. [32] argue that the inclusion of more overtones improves the precision with which they can recover the properties of the remnant (mass and spin), and that this would suggest that their model is physically justified.

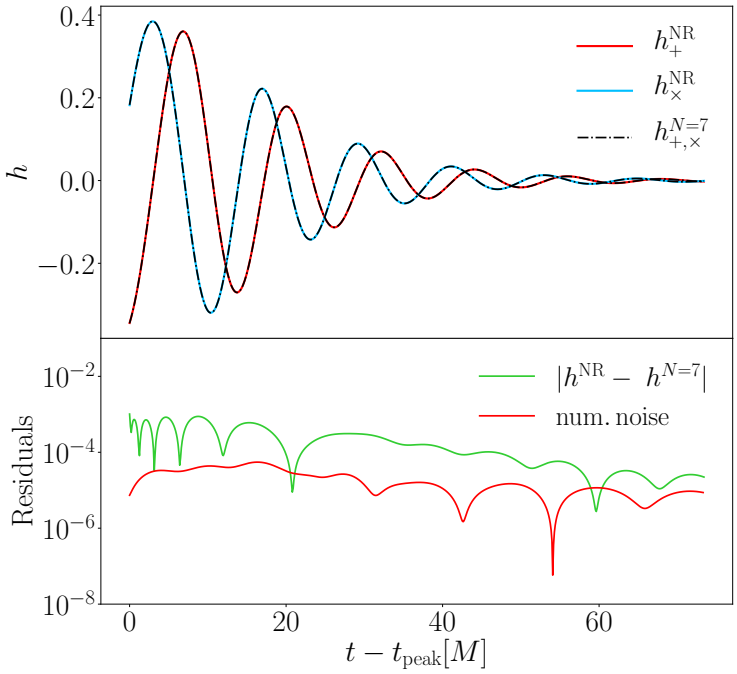

Figure 3.1: Fit and residuals for the numerical ringdown waveform SXS:BBH:0305 $h = h_+^{\rm NR} - ih_\times^{\rm NR}$ and the fit model (3.2). The simulation remnant has mass M equal to 0.952 of the total system mass $M_{\rm tot}$, and remnant dimensionless spin $\chi = 0.692$. Results are reproduced following [116]. Notice that, thanks to the scale invariance of the Einstein equations in vacuum, the results are invariant under simultaneous rescaling of the time and space units and the total system mass. The amplitude of the gravitational wave is to be interpreted as $h(t) \sim r/M_{\rm tot} \times h(t, r)$.

These questions are not simply of theoretical interest. The ringdown is currently used to test general relativity and in particular the no-hair theorem, which predicts that the perturbations of a black hole should only depend on its mass and spin (and charge). Currently, these tests are limited by the signal-to-noise ratio of current gravitational-wave detections, which only allow for one or two modes to be measured. Black hole spectroscopy, a proposed tool to test the no-hair theorem in future detections, will do so by comparing the inferred frequencies of multiple harmonic or overtone modes [97, 42]. Harmonic or overtone modes can be better suited for black hole spectroscopy depending on the mass ratio and signal-to-noise ratio of the event [193, 135]. This program relies on the idea

n	ωM	A	ϕ
0	$0.529 - i0.081$	0.97	1.47
1	$0.517 - i0.245$	4.17	-0.68
2	$0.496 - i0.414$	11.0	2.86
3	$0.467 - i0.587$	21.3	-0.27
4	$0.436 - i0.758$	27.7	2.67
5	$0.419 - i0.924$	20.4	-0.73
6	$0.419 - i1.103$	6.20	2.16

Table 3.1: Frequency of the QNMs (in units of the inverse remnant BH mass) of the remnant black hole of the simulation SXS:BBH:0305, together with the amplitudes and phases returned by the fit of Fig. 3.1. The QNM frequencies were computed with a Python package of the Black Hole Perturbation Toolkit [219]. Ref. [116] only included positive frequency modes, and we do the same here – for an analysis including negative frequency modes, see [93].

that QNMs are physical properties of the black hole emission, rather than mere fitting functions. Understanding this distinction and sharpening the theoretical predictions of the ringdown signal in general relativity are therefore important to our ability to test the theory in the future. Null tests of general relativity are possible without a detailed theoretical understanding of the nonlinear contributions to the ringdown, being based on numerical waveforms [7, 84]. However, the interpretation of a potential deviation from the numerical prediction would require detailed modeling, and the latter could also allow for more stringent tests—*e.g.*, by allowing one to "stack" several detections [239].

In the following sections, we investigate the nonlinear properties of the ringdown in a simplified setting: a gravitating scalar field in a black hole spacetime, with Anti de Sitter (AdS) asymptotics and spherical symmetry. Our strategy will be to perturb the system with a variety of initial conditions, and study its nonlinear response. The linear properties of Schwarzschild-AdS black holes have been studied at length for their relevance to holography, starting from [74, 130, 69, 68] (with a focus on black holes that are large compared to the AdS length-scale). Because the AdS boundary (equipped with reflecting boundary conditions) does not allow modes to dissipate at infinity, AdS spacetimes have been used as an ideal testing ground for nonlinearities in general relativity, see, *e.g.*, [120]. In our analysis, we will focus on small black holes, where the reflection effects associated with the AdS boundary can be neglected (at least at early times) and the evolution more

closely resembles the one in asymptotically flat black holes, although with longer QNM decay times. We describe the system and the analysis in Sections 3.2.1, 3.2.2 and 3.2.3. We present our results in Sections 3.2.4 (for QNM perturbations) and 3.2.5 (for compact pulse perturbations), and describe the backreaction on the black hole in Section 3.2.6. Finally, we discuss possible future developments in Section 3.3. In this Chapter, we use units in which $8\pi G = c = 1$.

3.2 An investigation in a simplified setting

3.2.1 Scalar field in a Schwarzschild-Anti de Sitter spacetime

We study the ringdown of a massless scalar field ϕ in a Schwarzschild-AdS spacetime in spherical symmetry. This system is described by the equations of motion

$$G_{ab} - \frac{3}{L^2} g_{ab} = T_{ab}, \tag{3.3}$$

$$\nabla^a \nabla_a \phi = 0, \tag{3.4}$$

where G_{ab} is the Einstein tensor, L is the AdS length scale, related to the cosmological constant by $3/L^2 = -\Lambda$. The scalar field stress-energy tensor T_{ab} reads

$$T_{ab} = \frac{1}{16\pi} \left[\partial_a \phi^* \partial_b \phi + \partial_a \phi \partial_b \phi^* - g_{ab} \partial^c \phi^* \partial_c \phi \right] . \tag{3.5}$$

We restrict the problem to spherical symmetry by using the following ansatz for the metric,

$$ds^2 = -A(v,r) dv^2 + 2 dv dr + \Sigma(v,r) d\Omega_2^2. \tag{3.6}$$

In the absence of perturbations and for a vanishing scalar field, the solution to the equations of motion is the Schwarzschild-AdS spacetime,

$$ds^2 = -f_{\rm SAdS}(r) dt^2 + f_{\rm SAdS}(r)^{-1} dr^2 + r^2 d\Omega_2^2 \tag{3.7}$$

with $f_{\rm SAdS}(r) = 1 - \frac{2M}{r} + \frac{r^2}{L^2}$. Scalar field perturbations in this background are characterized by scalar QNMs, which solve the linearized scalar field equation. For the ansatz $\phi = e^{-i\omega t} R(r) Y_l^m(\theta, \varphi)$ (in terms of the spherical harmonics Y_l^m), the linearized equation reduces to an equation for the radial function

$$\frac{d}{dr} \left(r^2 f_{\rm SAdS}(r) \frac{d}{dr} R \right) + \left(\frac{\omega^2 r^2}{f_{\rm SAdS}(r)} - l(l+1) \right) R = 0 \, . \tag{3.8}$$

This equation can be reduced to a Schroedinger-like equation by introducing the tortoise coordinate $\frac{dr_*}{dr} = f^{-1}_{\rm SAdS}(r)$, and redefining the radial function $R = r^{-1}X(r)$,

$$\frac{d^2}{dr_*^2}X + (\omega^2 - V_{\rm SAdS}(r))X = 0, \tag{3.9}$$

where $V_{\rm SAdS}(r) = -f_{\rm SAdS}(r)\left(\frac{l(l+1)}{r^2} + \frac{f'_{\rm SAdS}(r)}{r}\right)$. The potential goes to zero at the horizon, *i.e.*, $r \to r_+$ or $r_* \to -\infty$, and goes to infinity at spatially infinity as a consequence of the AdS asymptotics of the background. The boundary conditions for the scalar field QNMs are therefore the standard ingoing conditions at the horizon,

$$\phi \sim e^{-i\omega(t+r_*)}, \quad r_* \to -\infty, \tag{3.10}$$

while near spatial infinity the radial function has two solutions, behaving as $\phi \sim$ const. and $\phi \sim r^{-3}$ respectively. The latter asymptotic behavior is consistent with reflective boundary conditions at the AdS boundary, and is therefore picked as the second condition identifying QNM solutions of the scalar field.

In what follows, the QNM frequencies and QNM radial profiles were computed numerically using Leaver's method [152, 114] with a Mathematica notebook developed by the authors of [52]. The full system of equations (3.3–3.4) was solved in spherical symmetry with the numerical code developed by Bosch, Green, and Lehner in [51] and used in [52] to study the dynamical excitation of hairy black holes in AdS. The code uses ingoing Eddington-Finkelstein coordinates (v, r) and a finite difference scheme with mixed second and fourth order radial derivative operators, and fourth order Runge-Kutta discretization for the time evolution. The radial domain is compactified to reach the AdS boundary, by using the radial coordinate $\rho = 1/r$, $0 < \rho < 1/r_0$, with r_0 lying just inside the black hole horizon. The black hole singularity is excised from the domain. Numerical simulations are provided boundary data (the ADM mass M) and initial data, *i.e.*, the initial value of the scalar field ϕ along the slice $v = 0$.

3.2.2 Excitation coefficients and perturbation theory beyond linear order

Before we move on to the analysis of the numerical results, let us take a closer look at the system described by Eqs. (3.3–3.4) through the lens of perturbation theory. The QNM excitation coefficients for Kerr black holes, predicting the amplitude and phase of QNMs as a function of the initial perturbation, were first introduced and computed by Berti and

Cardoso [40], building on the theoretical framework of Refs. [152, 153, 151]. Here we adapt the treatment of [40] to the case of a scalar perturbation of a SAdS black hole.

As explained above Eq. (3.9), the equation for the scalar field can be reduced, at first order in perturbation theory, to a Klein Gordon-like equation,

$$-\frac{d^2}{dt^2}X+\frac{d^2}{dr_*^2}X-V_{\rm SAdS}(r)X=0, \tag{3.11}$$

where we have momentarily re-introduced the time dependence. We can define a Laplace-Fourier transform of the field variable X,

$$\hat{X}(\omega,r)=\int_0^{+\infty}dtX(t,r)e^{+i\omega t}. \tag{3.12}$$

This is a Laplace transform in the sense that we are only interested in times $t\geq t_0$, but the Laplace variable $s=i\omega$ is taken to be complex. The inverse transform is

$$X(t,r)=\frac{1}{2\pi}\int_{-\infty+ic}^{+\infty+ic}d\omega\hat{X}(\omega,r)e^{-i\omega t}. \tag{3.13}$$

where the contour of integration is taken to run above the real line in the complex ω plane ($c>0$). The transform must satisfy

$$\frac{d^2}{dr_*^2}\hat{X}(\omega,r)+(\omega^2-V_{\rm SAdS}(r))\hat{X}(\omega,r)=I(\omega,r), \tag{3.14}$$

where the function $I(\omega,r)$ is related to the initial conditions of the field[2] at $t=0$, $\phi(0,r)=r^{-1}X^{(0)}(r)$ and $\dot{\phi}(0,r)=r^{-1}\dot{X}^{(0)}(r)$, by the properties of the derivative of the transform[3],

$$I(\omega,r)=\left[i\omega X^{(0)}(r)-\dot{X}^{(0)}(r)\right]. \tag{3.17}$$

[2]The perturbations equations are invariant under time translation and we are therefore free to set the initial time to $t=0$.

[3]Let us compute the transform of the time derivative,

$$\int_0^\infty dt\dot{X}(t,r)e^{i\omega t}=X^{(0)}(r)-i\omega\int_0^\infty dtX(t,r)e^{i\omega t}, \tag{3.15}$$

assuming $X(r)\to 0$ for $t\to\infty$. The transform of the second time derivative is then

$$\int_0^\infty dt\ddot{X}(t,r)e^{i\omega t}=\dot{X}^{(0)}(r)-i\omega\int_0^\infty dt\dot{X}(t,r)e^{i\omega t}=\dot{X}^{(0)}(r)-i\omega X^{(0)}(r)-\omega^2\int_0^\infty dtX(t,r)e^{i\omega t}. \tag{3.16}$$

This tells us that the transform of $-d^2X/dt^2$ is $-\dot{X}^{(0)}+i\omega X^{(0)}+\omega^2\hat{X}$.

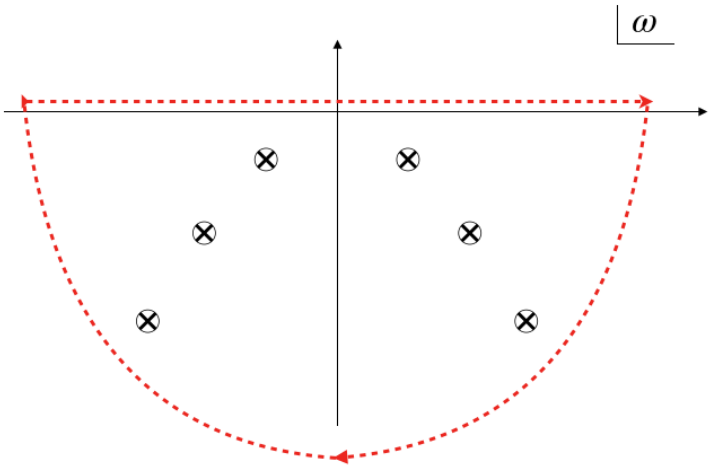

Figure 3.2: Integration contour used to evaluate the transform of (3.20). The integral is originally defined with a contour running above the real line from left to right. The crossed circles mark zeros of the Wronskian, or the QNM frequencies, and the semicircle at infinity carries a non-zero contribution, associated with the direct propagation of the perturbation to the observer along null geodesics.

The general solution to Eq. (3.14) can be found via the Green's function of the homogeneous equation, defined in terms of two independent solutions $\hat{X}_{r_+}$, $\hat{X}_\infty$. These are defined by their behavior at the horizon and at infinity,

$$\lim_{r\to r_+} \hat{X}_{r_+} \sim e^{-i\omega r_*}, \qquad \lim_{r\to+\infty} \hat{X}_{r_+} \sim B_\infty(\omega) r + A_\infty(\omega)/r^2, \tag{3.18}$$

and

$$\lim_{r\to+\infty} \hat{X}_\infty \sim 1/r^2. \tag{3.19}$$

We can then write the solution to (3.14) in terms of the Green's function

$$\hat{X}(\omega,r) = \hat{X}_\infty(\omega,r)\int_{-\infty}^{r_*} dr'_* \frac{\hat{X}_{r_+}(\omega,r'_*)I(\omega,r'_*)}{W(\omega)} + \hat{X}_{r_+}(\omega,r)\int_{r_*}^{0} dr'_* \frac{\hat{X}_\infty(\omega,r'_*)I(\omega,r'_*)}{W(\omega)}, \tag{3.20}$$

where $W = 3B_\infty(\omega)$ is the Wronskian of the two solutions (3.18), (3.19). From the asymptotic behavior of $\hat{X}_{r_+}$, Eq. (3.18), we realize that the QNM frequencies are defined as the values of ω for which $B_\infty(\omega) = 0$.

To go back to the time domain, we need to plug this solution in the inverse transform, Eq. (3.13). The integrand exhibits poles at the QNM frequencies, where the Wronskian

W is zero. However, the integrand does not present any branch cuts (which are present, *e.g.*, in asymptotically flat spacetimes), thanks to the asymptotic behavior of the potential. The integral along a closed contour (represented in Fig. 3.2) would therefore receive contributions from the semi-circle at infinity and the original integral above the real line, and is equal to the sum of the residuals associated with all the poles, located in the lower-half plane at the QNM frequencies. In this work, we focus on the QNM contribution to the response, and neglect the contribution of the semicircle at large $|\omega|$ enclosing the poles in the complex plane. The contribution of the semicircle corresponds to the direct propagation of the perturbation to the observer. We therefore only evaluate the residuals, finding

$$\begin{aligned} X(t,r) &= \sum_n iA_\infty(\omega_n) \left(\frac{dW}{d\omega}\right)^{-1}\Bigg|_{\omega_n} \left[\int_{-\infty}^{0} \mathrm{d}r'_* I(\omega_n, r'_*)\hat{X}_{\omega_n}(\omega_n, r'_*)\right] \hat{X}_{\omega_n}(\omega_n, r) e^{-i\omega_n t} \\ &\sim \sum_n iA_\infty(\omega_n) \left(\frac{dW}{d\omega}\right)^{-1}\Bigg|_{\omega_n} \left[\int_{-\infty}^{0} \mathrm{d}r'_* I(\omega_n, r'_*)\hat{X}_{\omega_n}(\omega_n, r'_*)\right] \frac{1}{r^2}\, e^{-i\omega_n t}, \end{aligned} \tag{3.21}$$

where we defined the QNM radial profile $\hat{X}_{\omega_n} = \hat{X}_\infty\Big|_{\omega_n} = \hat{X}_{r_+}/A_\infty\Big|_{\omega_n}$, normalized to unity at the AdS boundary. In the second line, we approximated the profile away from the black hole, $\hat{X}_{\omega_n} \sim r^{-2}$. Here we are not making any assumptions about how the initial perturbation $I(\omega, r)$ is localized, and we are integrating over the whole spacetime outside the horizon.

From this expression, the QNM *excitation coefficients* are defined as

$$C_n = iA_\infty(\omega_n) \left(\frac{dW}{d\omega}\right)^{-1}\Bigg|_{\omega_n} \left[\int_{-\infty}^{0} \mathrm{d}r'_* I(\omega_n, r'_*)\hat{X}_{\omega_n}(\omega_n, r'_*)\right], \tag{3.22}$$

and are therefore proportional to the overlap integral of the initial condition with the relevant QNM profile. The prefactors, which are independent of the initial condition and only depend on the properties of the background geometry and the type of perturbation considered, are known as the *excitation factors*,

$$B_n = iA_\infty(\omega_n) \left(\frac{dW}{d\omega}\right)^{-1}\Bigg|_{\omega_n}. \tag{3.23}$$

The discussion above applies to the leading linearized order in the scalar perturbations, and neglects the backreaction on the black hole geometry. We now briefly explore the equations governing perturbations beyond leading order, reviewing and extending the

results of [69, 130]. With our investigations of ringdown nonlinearities in mind, we study the dynamical response of the system (3.3), (3.4), to a scalar, spherically symmetric QNM perturbation, $\phi(t=0,r)=\phi_n(r)$. We assume this produces a small perturbation of the background SAdS solution $g^{(0)}_{ab}=g^{\rm SAdS}_{ab}$. Schematically, we can write

$$g_{ab}=g^{(0)}_{ab}+\epsilon h^{(1)}_{ab}+\epsilon^2 h^{(2)}_{ab}+\dots, \tag{3.24}$$

$$\phi=0+\epsilon\phi^{(1)}+\dots, \tag{3.25}$$

where ϵ is a small parameter used to keep track of the order of the perturbations.

The metric perturbations can be reduced, in spherical symmetry, to spherically symmetric modes, which are also even-parity modes. The metric perturbation at order n is first written in the Regge-Wheeler gauge,

$$h^{(n)}_{ab}=\begin{bmatrix} H^{(n)}_0(t,r)f_{\rm SAdS}(r) & H^{(n)}_1(t,r) & 0 & 0\\ H^{(n)}_1(t,r) & H^{(n)}_2(t,r)f^{-1}_{\rm SAdS}(r) & 0 & 0\\ 0 & 0 & r^2K^{(n)}(t,r) & 0\\ 0 & 0 & 0 & r^2K^{(n)}(t,r)\sin^2\theta \end{bmatrix}. \tag{3.26}$$

After a series of manipulations involving the Bianchi identities, all four free metric functions $H^{(n)}_0$, $H^{(n)}_1$, $H^{(n)}_2$, $K^{(n)}$ can be written in terms of a single master variable, $\Psi^{(n)}_g$. For the scalar field these manipulations are not required, because the scalar field coincides with its master variable up to a factor of r, $X^{(n)}=\Psi^{(n)}_s$. These steps allow us to write the perturbation theory equations at all orders as

$$\left(-\frac{d^2}{dt^2}+\frac{d^2}{dr_*^2}-V_{{\rm SAdS},i}(r)\right)\Psi^{(n)}_i(t,r)=S^{(n)}_i(t,r)\quad \text{with } i=s,g. \tag{3.27}$$

The potential $V_{{\rm SAdS},i}$ [4] takes a different shape for scalar and gravitational perturbations, but is the same at all orders: perturbations of the same type are governed by the same differential operator on the left-hand side at all orders. The source, on the right-hand side, can contain all lower order perturbations and their derivatives, with r_*-dependent coefficients. What we need to solve, order by order, are therefore decoupled wave equations with a given potential and a given source. Notice that we can only separate the time and radial variables in the absence of a source, *i.e.*, at leading order in the perturbation.

From the structure of the equations of motion (3.3–3.4) we realize that the leading order perturbation $\phi^{(1)}$ is not sourced, and only depends on the background solution and

[4] The potential of even-parity spin-2 perturbations of SAdS is given in Ref. [69].

the initial conditions. Thus, it satisfies the standard equations for the spin-0 QNMs of a SAdS black hole, Eq. (3.9), and can be solved using the Green's function method, as explained at the beginning of this section. The initial conditions of our choice imply a non-zero first order scalar perturbation, whose QNM content is set by the QNM excitation coefficients of Eq. (3.22).

At order $\mathcal{O}(\epsilon)$, the metric is not sourced by the scalar field, which enters the stress-energy tensor (and therefore the Einstein equation) quadratically. We can thus set this term, not directly sourced by the initial condition, to zero. The first order at which the metric perturbation is sourced by the scalar field is $\Psi_g^{(2)}$. The latter satisfies an equation of the form

$$\left(-\frac{d^2}{dt^2}+\frac{d^2}{dr_*^2}-V_{\mathrm{SAdS},g}(r)\right)\Psi_g^{(2)}=a(r)\,\phi^{(1)*}\phi^{(1)}+b(r)\,\phi^{(1)*}_{,r}\phi^{(1)}_{,r}+c(r)\,\phi^{(1)*}_{,t}\phi^{(1)}_{,t}, \tag{3.28}$$

where a, b, c are given functions of r (we omit the explicit expressions for brevity). To solve this equation, we could transform the master variable and the source, $\Psi_g^{(2)}(\omega,r)=\int_{t_0}^{+\infty}dt\,e^{i\omega t}\Psi_g^{(2)}(t,r)$, $S_g^{(2)}(\omega,r)=\int_{t_0}^{+\infty}dt\,e^{i\omega t}S_g^{(2)}(t,r)$[5]. This reduces Eq. (3.28) to

$$\left(\partial_{r_*}^2+\omega^2-V_g\right)\Psi_g^{(2)}(\omega,r)=S_g^{(2)}(\omega,r) \tag{3.29}$$

This expression allows us to conclude that second order gravitational perturbations will be a sum of the same QNMs characterizing the leading order perturbations, as they are governed by the same differential operator.

3.2.3 The analysis

In the following Sections, we study the scalar field at the AdS boundary – hereafter $\phi(t)\sim\phi(t,r)r^3$ – as well as the black hole horizon area as a function of time, produced with numerical simulations of the fully nonlinear (although spherically symmetric) equations (3.3–3.4). We study the system for different initial scalar field configurations, starting from a QNM initial perturbation of overtone number n,

$$\phi(v=0,r)=A_{\mathrm{pert}}\phi_n(r). \tag{3.30}$$

We normalize the QNM radial profiles so that $\max_r\phi_n=1$ and vary the overall perturbation amplitude A_{pert}. We also consider more generic compact pulse perturbations,

$$\phi(v=0,x=1/r)=\begin{cases}-A_{\mathrm{pert}}(x-x_{\mathrm{min}})^3(x-x_{\mathrm{max}})^3 & \text{for } x\in[x_{\mathrm{min}},x_{\mathrm{max}}]\\ 0 & \text{otherwise,}\end{cases}, \tag{3.31}$$

[5]The initial condition for $\Psi_g^{(2)}$ vanishes, so there is no term analogous to $I(\omega,r)$ in Eq. (3.14)

In order to understand the QNM content of the scalar field ringdown induced by the initial perturbation, we fit the boundary data with the model

$$\phi^{N_+,N_-} = \sum_{n=0}^{N_+-1} A_{+n} e^{i\omega_n(t-t_0)+\varphi_{+n}} + \sum_{n=0}^{N_--1} A_{-n} e^{-i\omega_n^*(t-t_0)+\varphi_{-n}}, \tag{3.32}$$

where the two sums contain the positive and negative frequency modes respectively, $\omega_{+n} = \omega_{n,\mathrm{R}} + i\omega_{n,\mathrm{I}}$ and $\omega_{-n} = -\omega_n^* = -\omega_{n,\mathrm{R}} + i\omega_{n,\mathrm{I}}$, where $\omega_{n,R} > 0$. We perform least square fits of the boundary data, where we hold all frequencies fixed to their true values and determine the value of the amplitudes A and phases φ. The true frequencies are taken to be the scalar QNM frequencies (computed according to [52]) for a black hole of mass equal to the final mass, or ADM mass of the system. The fits are performed between times t_0 and T, which might not coincide with the start and end time of the simulation.

We estimate the numerical noise as the residuals between our main datasets and higher resolution simulations, $|\phi - \phi^{\text{ higher res.}}|$. In order to estimate the global goodness of the fit, we compute the mismatch,

$$\mathcal{M} = 1 - \frac{\langle \phi, \phi^{\mathrm{fit}} \rangle}{\sqrt{\langle \phi, \phi \rangle \langle \phi^{\mathrm{fit}}, \phi^{\mathrm{fit}} \rangle}}, \tag{3.33}$$

where $\langle f, g \rangle = \int_{t_0}^{T} f(t) g^*(t)\, dt$. The lower the mismatch, the better the fit reproduces the data over the entire time series. Finally, we estimate the trade-off between a better fit and a higher number of parameters, *i.e.*, the over-fitting, by computing the Akaike Information Criterion (AIC) [173],

$$\mathrm{AIC} = 2k + n \log(RSS) \tag{3.34}$$

where n is the number of data points, k is the number of parameters and $\mathrm{RSS} = \sum_i |\phi_i - \phi_{i\,\mathrm{fit}}|^2$ is the residual sum of squares. The AIC allows to compare different statistical models (in this case, with a different overtone content), weighing both the increase in parameters and the decrease in residuals. A model with lower AIC is preferred relative to a model with higher AIC.

For concreteness, we focus on a small black hole in AdS, $r_+ \ll L$, and set $L = 1$, $M_{\mathrm{ADM}} = 0.104$ (unless stated otherwise).

3.2.4 Results: quasi normal mode perturbations

Typical ringdown data is shown in Fig. 3.3 for an initial perturbation composed of the first overtone, $n = 1$. We notice that the ringdown starts directly from the perturbing mode,

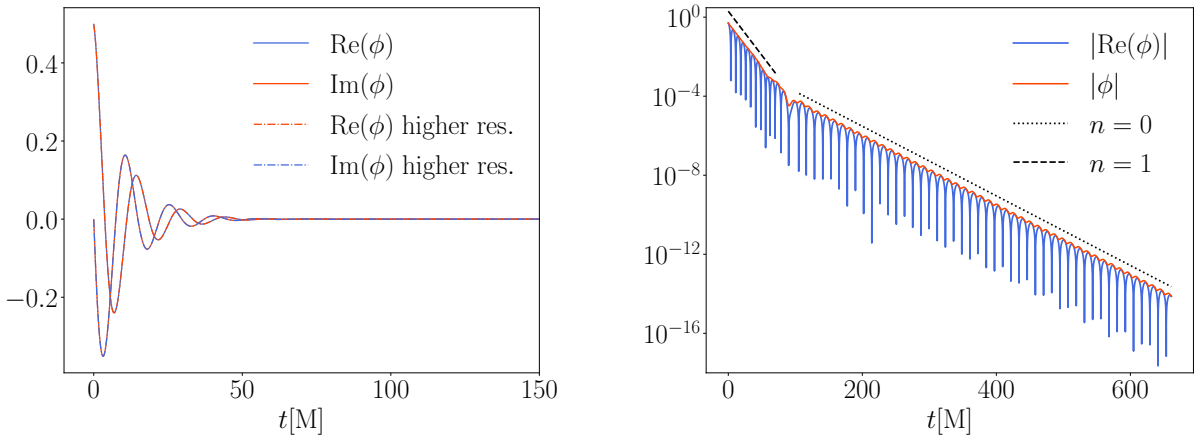

Figure 3.3: Scalar field ringdown to a $n = 1$ perturbation with $A_{\rm pert} = 0.1$. *Left*: real and imaginary part of the scalar field at the AdS boundary. Dashed lines indicate higher resolution data. *Right*: absolute value of the real part and of the full scalar field at the AdS boundary. This plot reveals the nonlinear feature, *i.e.*, the emergence of two lower-n quasi normal modes. For visual comparison, we plot the slopes of the fundamental (dotted) and first overtone (dashed).

with no sign of an "immediate response" phase. This can be explained by the fact that the QNM radial profile extends up to the black hole horizon and the AdS boundary from the very first slice of the simulation. For this reason, we can start fitting the data with our QNM models at $t_0 = 0$. The data does not present significant features at late times – and indeed we do not expect power law tails in SAdS. We can therefore fit up to $T \simeq 300M$.

By inspecting the right panel in Fig. 3.3, we can identify the first overtone (*i.e.*, the perturbing mode) in the initial segment of the data and a mix of the positive and negative frequency fundamental modes ($\pm\omega_{0,r} + i\omega_{0,i}$, with a longer decay time) in the later segment. This simple model suggested by visual inspection is confirmed by a least square fit. Fig. 3.4 shows how the residuals significantly decrease from well above the numerical noise as we add the modes $n = +0$, $n = -0$ and $n = 1$ to the fit model. The evidence for overtones above the perturbing mode, $n > 1$, is very weak, as can be seen from Fig. 3.4 and Table 3.2. The residuals do not improve significantly when increasing the total number of overtones N. From Table 3.2, we see that the amplitudes of the first three modes remain consistent with the minimal model as overtones are added, while the amplitudes of the $n = 2$ mode has a 100% variation when going from $N = 2$ to $N = 3$. The mismatch decreases significantly

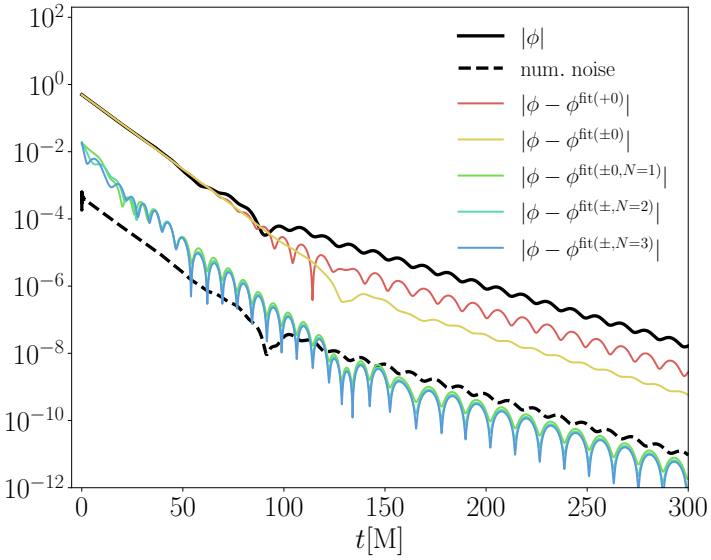

Figure 3.4: Scalar field ringdown to an $n = 1$ perturbation with $A_{\mathrm{pert}} = 0.1$. The minimal model is composed of the two fundamental modes and the first overtone (the perturbation), in green. For the minimal model, the fit residuals run below the numerical noise only in the late ringdown, indicating some over-fitting The residuals do not decrease significantly when higher overtones $n > 1$ are added, meaning that there is weak evidence supporting their presence in the data.

when reaching the minimal model $N = 1$, but fluctuates around the minimum value for $N = 2, 3$. The variation of the AIC seems to indicate slight preference for models with higher N. For simplicity,we omit the negative frequency first overtone, $n = -1$, which also does not lower the residuals significantly.

Generalizing to other overtone perturbations, we find strong evidence that the perturbing mode sources at a lower amplitude all modes with $n < n_{\mathrm{pert}}$, with positive and negative frequency. For instance, a $n = 1$ perturbation sources $n = \pm 0$, a $n = 2$ perturbation sources $n = \pm 0$, $n = \pm 1$, etc. The fundamental mode also follows this pattern, and does not source any modes, not even its negative frequency companion, at least not at a level detectable by our methods and with our level of numerical noise.

To identify the mechanism that sources lower n modes, we perturb the system with initial QNM perturbations with different amplitudes. We generically find that the perturbing

	$\lvert\mathcal{M}\rvert$	δAIC	A_{+0}	A_{-0}	A_1	A_2	A_3
$+0$	0.9338	0.0000	0.0031	0.0000	0.0000	0.0000	0.0000
± 0	0.9690	0.0001	0.0032	0.0006	0.0000	0.0000	0.0000
$\pm 0, N = 1$	0.0040	-1.3914	0.0033	0.0006	0.5139	0.0000	0.0000
$\pm 0, N = 2$	0.0074	-1.4936	0.0033	0.0006	0.5148	0.0140	0.0000
$\pm 0, N = 3$	0.0065	-1.5895	0.0033	0.0006	0.5152	0.0208	0.0186

Table 3.2: Analysis of the scalar field ringdown to an $n = 1$ perturbation with $A_{\rm pert} = 0.1$. We consider fit models with different overtone content. We show, in order, the mismatch between the data and the fit, the variation of the Akaike information criterion, and the amplitudes of the overtones resulting from the least-squares fit.

mode sources lower modes cubically,

$$A_{n<n_{\rm pert}} \sim A^3_{\rm pert}, \tag{3.35}$$

with $\mathcal{O}(10 - 0.1)$ prefactors. This is shown in Fig. 3.5 for $n = 1$ and $n = 2$ perturbations, but we confirmed this pattern up to $n = 10$[6]. A cubic relation clearly indicates the presence of a nonlinear effect. In our perturbative analysis of Eqs. (3.3–3.4) in Section 3.2.2, we saw that a perturbation $\delta\phi$ enters the equation for the metric quadratically through the stress energy tensor, $\delta g \sim \delta\phi^2$. A higher order perturbation of the scalar field is then sourced (at leading order) by a product of the original perturbation and the metric perturbation, $\delta\phi\delta g \sim \delta\phi^3$, which explains the cubic dependence found in the numerical data.

The cubic relation is equally consistent with two types of nonlinearities:

- a dynamical nonlinearity;
- a nonlinearity on the initial slice (*i.e.*, in the initial conditions). The perturbing mode is constructed as a scalar QNM of the background black hole, originally set to have mass equal to the ADM mass of the system. However, the constraint equations require that the ADM mass must be distributed between the black hole and the scalar field at $v = 0$ (or the very next time step), and the true initial mass of the black hole is therefore lower then the ADM mass. For this black hole, our initial perturbation is not exactly a quasi normal mode. In this sense, other modes can be

[6]At higher n, the number of parameters to fit increases as $4(n-1)$, and we are less confident in the amplitudes of high-n overtones recovered by the fit.

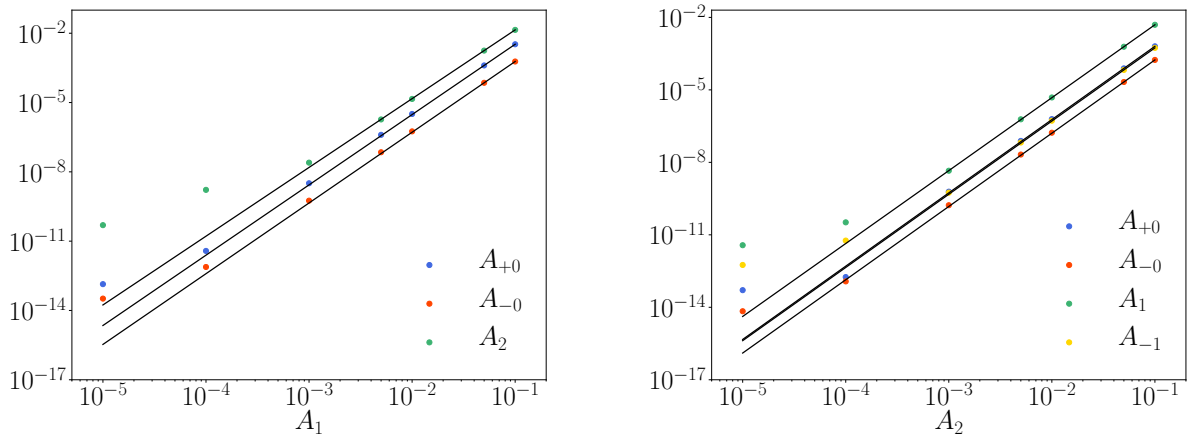

Figure 3.5: *Left*: amplitudes of sourced modes as a function of the perturbation amplitude ($n = 1$), superposed with a cubic fit, in black. The amplitudes deviate from the cubic relation when the perturbation is too weak compared to numerical noise, and this happens at higher amplitudes for higher modes. *Right*: second overtone perturbation, $n = 2$.

directly sourced by the initial conditions, eluding the fact that in linear theory, QNMs cannot source modes with different overtone numbers because of their orthogonality properties [121].

Our results are compatible with both explanations, and we have not found a way, so far, to distinguish between them. In some sense, these are two aspects of the nonlinear equations, and will both come into play for more generic perturbations, as we discuss in the next Section.

For completeness, we also studied larger black holes ($r_+ \gg L$) perturbed with single QNMs. We omit these results for brevity. We find that lower overtones are excited nonlinearly (cubically) also in larger black holes, at least at early times. Our late-times numerical data is more affected by numerical noise for larger black holes.

Building up to more general perturbations, we also perturb the system with a mix of scalar QNMs. As an example, we consider a perturbation composed of the $n = 2$ and $n = 3$ overtones, in a 30%–70% mix, with total amplitude $A_{\rm pert} = 0.05$. We fit the data with models with an increasing number of other modes, and find that the fit residuals decrease significantly when the positive and negative first overtone and fundamental modes

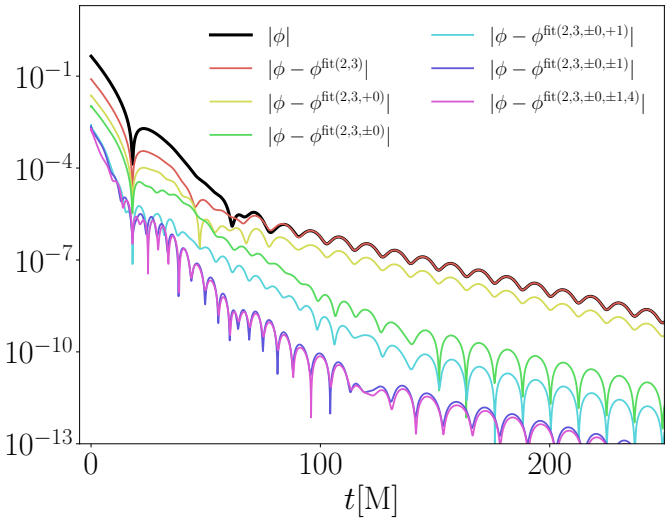

Figure 3.6: Scalar field ringdown to a perturbation composed of a mix of the $n = 2$ and $n = 3$ modes. We compare the fit residuals for different fit models. The fit improves substantially with the inclusion of the $n = \pm 1$ and $n = \pm 0$ modes, absent in the initial data and generated nonlinearly.

are included, in addition to the perturbing modes; see Fig. 3.6. The presence of these modes, not contained (at the linear level) in the initial perturbation, signals again that nonlinearities are at play. In particular, the amplitudes of the nonlinearly generated modes are consistent with being sourced by both the $n = 3$ and $n = 2$ initial perturbations (as a sum, at the order of magnitude level). This is seen by comparing the amplitudes of the modes resulting from the fit with the ones predicted by a cubic fit of five $n = 2$ and $n = 3$ perturbation datasets (along the lines of Fig. 3.5), see Table 3.3. We find again only small evidence for the presence of higher modes, $n > 3$, in the form of a small decrease of the AIC value, the residuals and the mismatch.

3.2.5 Results: compact pulse perturbations

We now consider a more realistic class of perturbations: compact pulses. Compact pulse perturbations introduce a new feature in the scalar field ringdown: a prompt response, caused by the delay with which the pulse reaches the AdS boundary (where we extract the scalar field value over time). The prompt response is not a superposition of QNMs, as

	A_2	A_3	A_{+0}	A_{-0}	A_{+1}	A_{-1}
pert $= 2 + 3$	0.11	0.34	$3.3\,10^{-5}$	$1.2\,10^{-5}$	$2.3\,10^{-4}$	$3.7\,10^{-5}$
pert $= 2$	0.11	0.00	$2.3\,10^{-6}$	$0.6\,10^{-6}$	$1.8\,10^{-5}$	$0.2\,10^{-5}$
pert $= 3$	0.00	0.34	$8.9\,10^{-6}$	$3.4\,10^{-6}$	$6.0\,10^{-5}$	$1.1\,10^{-5}$

Table 3.3: Scalar field ringdown sourced by a mix of the second and third overtones. The table compares the amplitudes found by a fit of the ringdown data (first row) with the predictions obtained by perturbing the black hole with one mode of varying amplitude at a time, and fitting the nonlinear (cubic) generation of lower modes (see Fig. 3.5 and discussion in the text).

understood from the analysis of the Green's function of the linearized equation[7]. Therefore, we start our fits after this feature has passed and QNMs are clearly identifiable, see Fig. 3.7, left panel.

We fit for the amplitudes of low n overtones as described in the previous sections, and vary the amplitude of the compact pulse perturbation. By comparing the amplitudes of the QNMs with the amplitude of the pulse (Fig. 3.7, right panel), we find a predominantly linear relation between them. In this case, the dominant phenomenon is therefore a direct excitation of QNMs by the initial perturbation, allowed by the linear order equations.

This is however not the whole story. Modes are also excited nonlinearly, although at lower amplitude. The best way to explore the purely nonlinear features of the ringdown is to subtract the linear response from the nonlinear data. We therefore generate both full nonlinear data (NL), and data produced with a modification of the numerical code where the interaction with gravity is switched off by setting $G = 0$. This produces what we call linear data (L). We checked that this is the best way to remove the linear response (at least for the range of perturbation amplitudes explored) as follows. We compared the linear subtraction with two other candidates: the subtraction of data generated with a black hole mass given by solving the constraint equation for the given initial scalar data ("initial mass" data), and with the subtraction of the Cowling approximation, which consists in solving the constraint on the initial slice and evolving forward with $G = 0$. We compare these three possibilities in Fig. 3.8, left panel, which shows that the linear data achieves the largest subtraction.

We therefore subtract the linear data from the nonlinear, and fit the difference for the

[7] As mentioned in Section 3.2.2, while QNM can be associated with the poles of the Green's function in the complex ω plane, the prompt response is associated with the contribution of the semicircle at infinity.

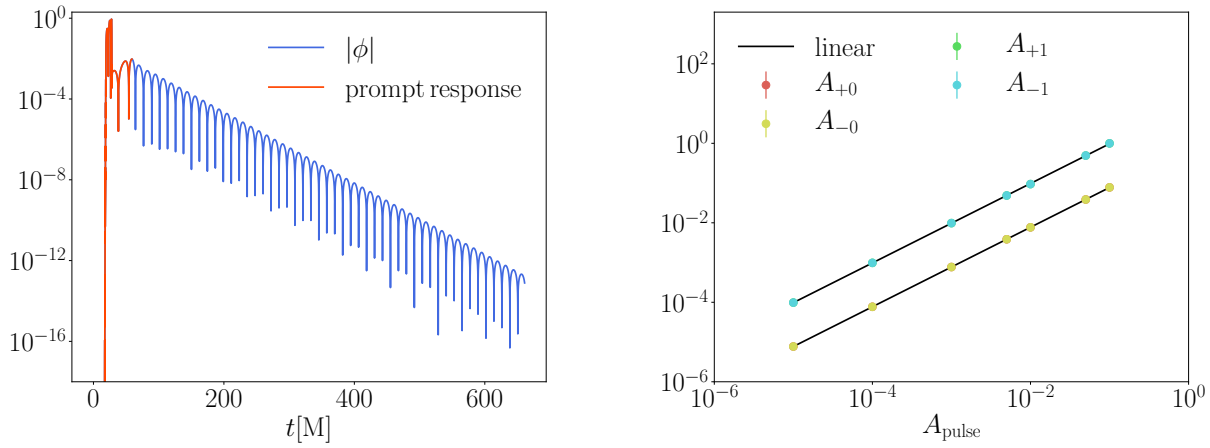

Figure 3.7: *Left*: Amplitude of the scalar field in response to a compact pulse perturbation of amplitude $A = 0.05$. The prompt response part of the data is highlighted in red. *Right*: The amplitude of first overtone and fundamental modes (positive and negative frequency) versus the compact pulse amplitude, overlaid with a linear fit. Note that positive and negative frequency modes have almost identical amplitudes and are overlaid in the plot.

QNM amplitudes and phases. As displayed in Fig. 3.8, right panel, the amplitudes in the subtracted data have approximately cubic relations with the pulse amplitude: we find best fits $A \sim A_{\rm pert}^{2.5}$ and $A \sim A_{\rm pert}^{3.2}$ for the first overtone and fundamental modes, respectively. This shows that also for generic and realistic initial data nonlinear interactions have the effect of further exciting QNMs, extending the results of the previous Section. In either case, we find no evidence of the presence of nonlinear features that cannot be described by QNMs.

3.2.6 Theoretical predictions: area increase

We now take a step back from the numerical data, and study how QNMs can backreact on the black hole spacetime. We start by writing the black hole metric in ingoing Eddington-Finkelstein coordinates, which are horizon-penetrating,

$$ds^2 = -f dv^2 + 2 dv dr + r^2 d\Omega^2 \,, \tag{3.36}$$

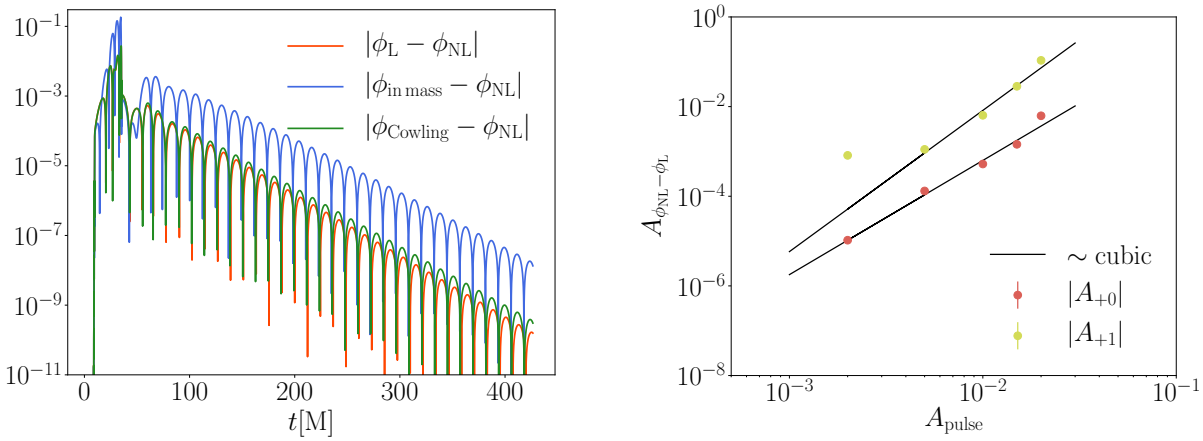

Figure 3.8: *Left*: Comparison between three methods for subtracting the linear response of the perturbed scalar field. The linear approximation subtracts the most out of the full nonlinear data. *Right*: Approximately cubic relation between the QNM amplitudes in the subtracted data and the pulse amplitude.

where $v = t + r^*$, with the tortoise coordinate defined by $\frac{dr^*}{dr} = f^{-1}$. Close to the horizon, a scalar QNM can be approximated as

$$\phi \sim A_{r_+}\, e^{-i\omega v} Y_l^m(\theta, \varphi)\,, \tag{3.37}$$

with $\omega = \omega_{\rm R} + i\omega_{\rm I}$ the complex mode frequency, $\omega_{\rm I} < 0$, and A_{r_+} the complex horizon amplitude (dimensionless in units in which the AdS length is set to $L = 1$). This approximation applies to both Schwarzschild-AdS as well as Schwarzschild black holes, as the behavior of the scalar field at the horizon is independent of the properties of the spacetime far away. For a static black hole, the time-like Killing vector can be written as

$$t^a = \left(\frac{\partial}{\partial t}\right)^a = \left(\frac{\partial}{\partial v}\right)^a - \left(\frac{\partial}{\partial r^*}\right)^a = \left(\frac{\partial}{\partial v}\right)^a - f\left(\frac{\partial}{\partial r}\right)^a . \tag{3.38}$$

This vector defines a conserved scalar field energy current,

$$J^a = -T^{ab} t_b\,, \tag{3.39}$$

where the scalar field stress-energy tensor was defined in Eq. (3.5). The integrated energy flux across the event horizon is then given by

$$\Phi(v) = \int_{\rm horizon} d\Omega\, n_a J^a \tag{3.40}$$

where n_a is the inward normal to the horizon, $n_a = -t_a$[8]. Focusing on spherically symmetric perturbations, $l = m = 0$, and using the normalization $Y_0^0 = 1/2\sqrt{\pi}$, we find

$$\Phi(v) = \frac{|\omega|^2}{8\pi}|A_{r_+}|^2 e^{2v\omega_{\rm I}}. \tag{3.41}$$

We find a positive flux, meaning that energy is being dumped into the black hole. In geometric units, we expect an energy per unit time to be dimensionless, and indeed the dimensions of ω and A would cancel out. Energy is falling into the black hole at an exponential rate, with a time scale given by half of the mode decay time, $\tau \simeq (2\omega_{\rm I})^{-1}$. We stress again that this result is valid for scalar QNMs of both Schwarzschild-AdS and Schwarzschild black holes, and really any spherically symmetric, static black hole. The amplitude measured at the horizon, A_{r_+} is in general a complicated function of the amplitude measured at infinity, as this relation depends on the full radial QNM profile.

A positive flux of energy through the horizon causes the latter (and therefore the black hole mass) to grow over time. The horizon area $\mathcal{A}$ is related to the irreducible mass by

$$\mathcal{A} = 16\pi M_{\rm irr}^2 \,. \tag{3.42}$$

For a Schwarzschild black hole, the irreducible mass is equal to the black hole mass, $M_{\rm irr} = M$, and the area varies according to[9]

$$\left.\frac{d\mathcal{A}}{dv}\right|_{\rm S} = 32\pi M\Phi(v)\,. \tag{3.43}$$

For a single QNM we find that the area will grow over time as

$$\mathcal{A}(v) = \mathcal{A}(0) + \frac{2M|\omega|^2\left|A_{r_+}\right|^2}{\omega_{\rm I}} e^{2v\omega_{\rm I}}\,. \tag{3.44}$$

In AdS, the black hole mass and the irreducible mass are related by $M = M_{\rm irr}(1 + 4M_{\rm irr}^2)$. Inverting this relation for $M > M_{\rm irr} > 0$, we find (for $L = 1$)

$$M_{\rm irr} = \frac{3^{2/3} - \sqrt[3]{3}\left(\sqrt{3}\sqrt{27M^2+1} - 9M\right)^{2/3}}{6\sqrt[3]{\sqrt{3}\sqrt{27M^2+1} - 9M}}\,. \tag{3.45}$$

The area variation is then given by

$$\left.\frac{d\mathcal{A}}{dv}\right|_{\rm SAdS} = 32\pi M_{irr}\frac{dM_{irr}}{dM}\Phi\,, \tag{3.46}$$

[8] We follow Wald's convention [232], Eq. (12.3.20), page 320.

[9] On the horizon, we can use interchangeably v or t.

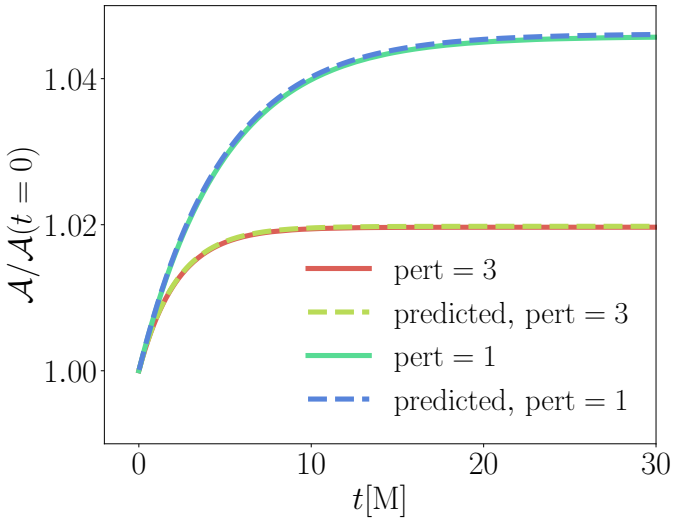

Figure 3.9: The area variation caused by QNM perturbations of amplitude $A = 0.05$ ($n = 1$ and $n = 3$). The analytical prediction (for a numerically determined QNM horizon amplitude) is overlaid as a dashed line.

which implies

$$\mathcal{A}(v) = \mathcal{A}(0) + \frac{2M_{\rm irr}|\omega|^2 \left|A_{r_+}\right|^2}{\omega_{\rm I}} \frac{dM_{irr}}{dM} e^{2v\omega_{\rm I}} \,. \tag{3.47}$$

The formulas above can be used to predict the change in mass of the BH in our numerical simulations. Using numerical QNM profiles, we can find a numerical relation between the QNM amplitude at infinity (the simulation output) and the amplitude at the horizon appearing in Eq. (3.47). This is shown in Fig. 3.9 for two examples, initialized with a $n = 1$ and a $n = 3$ perturbation. Fig. 3.9 shows excellent agreement between the predicted and the numerical evolution of the horizon area, which grows by 2–4 %. In particular, it confirms that the area variation timescale is set by the imaginary part of the frequency of the dominant (the perturbing) QNM. The numerical data therefore confirms the backreaction mechanism identified analytically in this Section.

3.3 Future prospects

The results of the previous sections point at two conclusions: that 1) nonlinearities in the scalar field–black hole system contribute to the amplitude of modes belonging to the linear spectrum and that 2) the absorption of QNMs can change the black hole mass over time at percent level, whit a timescale set by the dominant mode's decay time. These results, although limited to scalar perturbations in AdS black holes in spherical symmetry, might explain why models with a sufficient number of overtones can fit the ringdown signal close to merger, as in the recent study by Giesler et al. [116].

In the future, in order to further connect these two observations, we could make use of the Laplace-transform formalism outlined in Section 3.2.2 and Refs. [152, 153, 151]. This formalism predicts that, at linear level, the QNM amplitudes are given by the black hole excitation coefficients. In turn, these are given by the product of the excitation factors, which only depend on the black hole parameters, and an overlap integral between the QNM radial profile and the Laplace transform of the initial condition. Excitation factors and coefficients have been computed for Schwarzschild and Kerr black holes [40, 244], but the numerical methods could be easily extended to asymptotically AdS ones. Some nonlinear effects – such as the change in the black hole mass – could also be accounted for in the formalism, *e.g.*, by studying the overlap of QNM profiles associated with the initial and final mass, or by applying the formalism of the QNM excitation coefficients to higher order perturbations sourced by lower order ones.

More importantly, it remains to be seen whether the two conclusions mentioned above apply to gravitational perturbations of Kerr black holes, which describe the sources observed by gravitational wave detectors. To answer analogous questions in more realistic settings, it will be necessary

- to identify the initial conditions of the black hole ringdown in a binary merger. This step is complicated by the fact that numerical simulations use coordinates that are not easily mapped to the ones used in, *e.g.*, the Teukolsky formalism for perturbations of Kerr. Recently, there has been interest in the numerical study of nonlinearities surrounding the black hole horizon after a binary merger [190], and in the dynamical formation of the binary's common horizon [201, 202]; these investigations could prove useful to identify the initial conditions of the ringdown following a binary merger. The authors of [159, 208] also suggest using the close limit approximation [205] or the extreme-mass-ratio limit [27, 156] to black hole mergers to gain insight into the initial conditions of the ringdown;

- to investigate QNM interactions beyond linear order. A first step in this direction was taken by Ripley et al. [208], who studied second order perturbations of Kerr neglecting the backreaction on the black hole mass and spin. These preliminary investigations support a conclusion similar to the one of this thesis, *i.e.*, that the predominant effect of perturbations beyond linear order is to excite modes belonging to the QNM spectrum (although these results have not yet been compared to fully nonlinear numerical evolution). The formalism and publicly available code of Ripley et al. [208] could be extended to allow for the reconstruction of the full metric at second order (not just the radiation at null infinity) and even go beyond second order, by using the steps outlined by Green, Hollands and Zimmerman [122].

Chapter 4

Semiclassical approximation in gravity

4.1 The standard approach

The semiclassical approximation is a technique originally designed for applications in non-relativistic quantum mechanics, where it is known under the WKB acronym (after Wentzel, Kramers and Brillouin [58, 146, 238]). In particular, it is commonly used to solve problems involving quantum tunneling. The approximation relies on taking the mathematical limit $\hbar \to 0$. This limit requires care, as $\hbar$ will appear both in the dynamical equations and in the wave function[1]. Although it is more correct to talk about the limit of dimensionless parameters (such as the ratio of the action and $\hbar$), rather than natural constants, keeping track of the powers of $\hbar$ is a useful trick in many practical calculations. Expansions in $\hbar$ rarely converge, but can be seen as asymptotic expansions.

The semiclassical approximation is widely used in the context of quantum theories of gravity. It has been applied widely, with the more promising applications being the early universe and black hole spacetimes. In absence of a full quantum theory of gravity, which would allow for a self-consistent derivation of this approximation, the semiclassical formalism in the presence of gravity is commonly built from the bottom up. A bottom-up semiclassical theory is built to satisfy some of the principles of the classical theory, together with principles of quantum mechanics or quantum field theory. However, a bottom-up approach

[1]For instance, when considering the classical limit of the state of a particle, the state must become localized in *phase space* in such a limit.

to semiclassical gravity has its limitations: many of the guiding principles of quantum field theory, which we might have liked to carry over to the semiclassical approximation, are incompatible with general relativity. This is the case for Poincaré invariance, which in turn allows us to choose a unique representation of the commutation relations.

Despite these obstacles, it is still possible to construct a semiclassical theory that preserves all the principles of general relativity and some of the principles of quantum field theory. This is attempted by the algebraic approach to quantum field theory on curved spacetimes, as summarized by Hollands and Wald in [129]. In the presence of (non-conformally invariant) matter fields, both in gravitational and non-gravitational settings, the physical problem acquires multiple scales and one may consider different approximations: one in which all fields are treated as quantum, one in which some fields are treated classically and some are quantized, or the limit in which all fields are treated classically. Since we do not yet agree on a quantum theory of matter and gravity, we will be interested in the intermediate case, with matter fields quantized and the gravitational field treated as classical. Rather than expanding in $\hbar$, one uses the separation of scales between heavy (background) fields – like the homogeneous degrees of freedom of the gravitational field, associated with the volume of the universe (in a spatially closed model) – and light fields (gravitons and other matter fields). The heavy fields are treated classically, while the light fields are quantized. One should however always bear in mind that this procedure does not lead to a consistent stand-alone theory, and will only be a good description within its regime of validity.

The semiclassical approximation will in most cases correspond to what is known as quantum field theory in curved spacetime [47, 113, 233]. This is unless non-perturbative effects of gravity are relevant, *i.e.*, unless the relevant saddle point solution for the gravitational field is not a classical, real, metric. This is the case for the line of investigation initiated by the no-boundary proposal of Hartle and Hawking [126] and Vilenkin's tunneling proposal [230]. In these proposals for the early universe, the metric (in minisuperspace models, the scale factor) behaves inherently non-classically. When such non-classical backgrounds are considered, the semiclassical limit for the matter fields can give unexpected results: see, *e.g.*, [94] for an application to inflation.

Consider the case of quantum electrodynamics, which has often been used as a toy model to understand the semiclassical limit of gravity (see, *e.g.*, [49, 140]). In the semiclassical approximation, the backreaction of a quantum field ϕ (giving rise to a current J_μ) onto a background electromagnetic field A_μ can be derived within the effective action formalism. This derivation can be found in many quantum field theory textbooks, such as Schwartz's [213]. One first defines – through a path integral – the generating functional of

in-out expectation values of the current operator,

$$Z[A_\mu] = \int \mathcal{D}\phi\, e^{iS[\phi,A_\mu]} \sim \sum_n \frac{1}{n!} \frac{\langle 0_{\rm out}|(iJ^\mu)^n|0_{\rm in}\rangle}{\langle 0_{\rm out}|0_{\rm in}\rangle} A_\mu^n, \tag{4.1}$$

where the action S is the action of the field ϕ (including self-interactions) plus the interaction term $\sim J_\mu A^\mu$. The integration is over all field configurations ϕ. Ideally, the contour would be deformed in the complex field space so that the integral becomes absolutely convergent. This definition of the path integral (which would involve Picard-Lefschetz theory) has not yet been succesfully applied to infinite dimensional integrals, and is beyond the scope of this introduction. The integral can alternatively be made convergent with the addition of a small convergence factor in the action, $\sim i\epsilon\phi^2$ with $\epsilon > 0$.

In the expression above, we can expand the integration variable around the classical solution, $\phi = \phi_{\rm cl} + \delta\phi$, with $\delta S/\delta\phi|_{\phi_{\rm cl}} = 0$,

$$Z = e^{iS[\phi_{\rm cl},A_\mu]} \int \mathcal{D}\delta\phi\, e^{i\,\delta S[\delta\phi]} = e^{iS[\phi_{\rm cl},A_\mu]}\, N. \tag{4.2}$$

Notice that after the split the remaining integral over the fluctuations is independent of the background field (which only appeared in terms quadratic in ϕ). The remaining integral can therefore be identified with the vacuum normalization $N = \langle 0_{\rm out}|0_{\rm in}\rangle^{-1}$. Comparing (4.1) and (4.2), we can define the effective action, $\Gamma[A_\mu] = S[\phi_{\rm cl}, A_\mu]$, and from this the expectation value of the current,

$$\left.\frac{\delta\Gamma[A_\mu]}{\delta A_\mu}\right|_{A_\mu=0} = \langle 0_{\rm out}|J^\mu|0_{\rm in}\rangle. \tag{4.3}$$

The in-in (out-out) vacuum expectation values can be derived, at zero loops in the interaction strength, from the in-out expressions by substituting the classical solution defined by the retarded (advanced) propagator rather than the Feynman one [237]. Weinberg discussed how the in-in formalism is complicated by the presence of interactions in [237].

We now have all the ingredients to derive the semiclassical equation describing the backreaction of the quantized field onto the background. We first define the reduced action for the background field by integrating out the quantized one,

$$\int \mathcal{D}A_\mu\, e^{iS_{\rm red}[A_\mu]} = \int \mathcal{D}A_\mu \int \mathcal{D}\phi\, e^{iS[\phi,A_\mu]+iS_B[A_\mu]} = \int \mathcal{D}A_\mu\, N\, e^{i\Gamma[A_\mu]+iS_B[A_\mu]} \tag{4.4}$$

where S_B is the action of the background, in this case the standard action for the electromagnetic field. The classical equation of motion for the background is then

$$\frac{\delta S_{\rm red}}{\delta A_\mu} = \frac{\delta\Gamma}{\delta A_\mu} + \frac{\delta S_B}{\delta A_\mu} = 0, \tag{4.5}$$

which reads

$$\partial_\nu F^{\mu\nu} = \langle 0_{\rm in}|\ J^\mu |0_{\rm in}\rangle\,, \tag{4.6}$$

once we ensure causality by substituting the in-in expectation value, as explained above.

By analogy, the backreaction of quantized matter fields onto the gravitational one can be computed via a semiclassical Einstein equation,

$$\frac{1}{8\pi G} G_{\mu\nu} + \rho_\Lambda g_{\mu\nu} = \langle \hat{T}_{\mu\nu} \rangle\,. \tag{4.7}$$

In this Chapter, we use units in which $c = \hbar = 1$ but G is a dimensionful constant. The expectation value of the stress-energy tensor is evaluated on a chosen state – the choice of state will be a central topic in the remainder of this Chapter. This equation will be discussed further in Section 4.3. We stress again that Eq. (4.7) is usually postulated, rather than being derived from a complete theory.

In this Chapter, we present a proposal to modify the semiclassical Einstein equation (4.7), in an attempt to resolve or at least shed new light on the cosmological constant problem. In the next Section, we briefly review modern and historical views on the cosmological constant problem. We present our proposal in detail in Section 4.3, and draw our conclusions and discuss potential improvements to the proposal in Section 4.4.

4.2 The cosmological constant problem

Clear expositions of the cosmological constant problem can be found in many reviews (see in particular [236, 61, 194, 172]). In this Section we give a brief overview of the problem, with emphasis on the subtleties of its very definition.

Several observations have now confirmed that our universe is filled with a vacuum energy density. The analysis of the Planck 2018 datasets found [20]

$$\rho_\Lambda = 7.2583 \times 10^{-121} M_{\rm Pl}^4, \tag{4.8}$$

From quantum field theory, we learned that constants of nature are related to infinities in perturbative calculations by renormalization,

$$\rho_{\Lambda\,\rm obs} = \rho_{\Lambda\,\rm bare} + \rho_{\Lambda\,\rm vacuum}, \tag{4.9}$$

where the contributions to $\rho_{\Lambda\,\rm vacuum}$ arise from the right hand side of (4.7), and can be thought of as radiative corrections from bubble diagrams. This standard argument can

already be questioned: is the semiclassical expansion involving gravity convergent, or at least asymptotic, and therefore a reliable approximation? What is the appropriate scale at which we should compute this contribution, and therefore which background metric should we use, a cosmological metric or a Minkowski metric? Do results depend on the background metric of choice? If we use a cosmological metric, is the non-uniqueness of the vacuum going to affect the result? What regularization scheme should we use to preserve the covariance of the semiclassical Einstein equation? Cut-off regularization, often used in back-of-the-envelope arguments on the cosmological constant problem, is not covariant and leads to inconsistencies, as mentioned in Chapter 1.

Even once these questions are addressed, two fundamental problems with the cosmological constant remain: its radiative instability and the coupling between ultraviolet (UV) and infrared (IR) physics. The cosmological constant is said to be radiatively unstable because vacuum terms in (4.9) do not die away as we consider more interaction terms in the theories contributing to the stress-energy tensor (such as quartic interactions in a scalar field theory). In other words, higher loop terms are not suppressed compared to lower ones, and renormalization would be equally important at each step (see, *e.g.*, Padilla's review [194]). The coupling of UV and IR is manifested in the fact that fields with heavier masses, which we would normally associate with high energies (UV physics), dominate over light (IR physics) fields in their contributions to the vacuum energy, as the latter go like $\rho_{\Lambda\,\text{vacuum}} \sim m^4$ even in covariant regularization schemes such as dimensional regularization or Pauli-Villars. If renormalization is carried out at low energies, when only light fields are relevant, the match between the renormalized quantity and the observed one is lost at higher energies, when more massive fields need to be taken into account [61].

The literature contains a long list of proposals claiming to resolve the cosmological constant problem. We can recognize two categories of solutions: ones that challenge the standard calculation of the radiative contributions to the cosmological constant, and ones that work within the standard framework, but find ways to make the radiative contributions small. Solutions in the first category might claim that vacuum fluctuations do not exist at all or challenge the standard appeal to experimental evidence around the Casimir effect [182, 50] or the Lamb shift, see [133], often claimed to prove the existence of vacuum fluctuations. Proposals in the second category might rely on symmetries (such as supersymmetry), alternative quantum formulations of gravity (such as unimodular gravity [26]), modifications of gravity (at short [19] or long distance [79]), or dynamical effects (such as Coleman's universe multiplication [80], membrane nucleation [59]). Some of these proposals have already been disproved formally (Coleman's theory) or experimentally (supersymmetry[2]), while others are still being tested and debated.

[2]Supersymmetry has been excluded at sufficiently low scales to be incompatible with a straightforward

In the following Sections, we work within the relatively well established framework of the semiclassical Einstein equation and its renormalization, and we propose a small modification to the way renormalization is performed in curved spacetimes.

4.3 An effective stress-energy tensor

4.3.1 Proposal

We begin by considering the semiclassical Einstein equation (4.7). The metric is treated as a classical background field, while matter fields are quantized. We regard (4.7) as an effective field theory that arises as the low energy limit of a more fundamental theory of gravity [96]. We also neglect higher order curvature terms that, in the ultraviolet, would arise on either sides of the equation. The expectation value of the stress-energy tensor $\langle \hat{T}_{\mu\nu} \rangle_\Psi = \langle \Psi | \, \hat{T}_{\mu\nu} \, | \Psi \rangle$ in the quantum state of the field, $|\Psi\rangle$, is a divergent quantity which we assume to be covariantly regularized.

In Minkowski spacetime, if the Hamiltonian has a ground state $|0_{\rm M}\rangle$, one can chose it as a gravitational reference state. One postulates that it is only the stress-energy above the stress-energy of this state that gravitates:

$$\langle \hat{T}_{\mu\nu} \rangle_\Psi^{\rm ren.} = \langle \hat{T}_{\mu\nu} \rangle_\Psi - \langle \hat{T}_{\mu\nu} \rangle_{\rm M} \, . \tag{4.10}$$

Even in flat spacetime, there might exist several ground states. However, one can choose the ground state $|0_{\rm M}\rangle$ of the Hamiltonian that respects the Poincaré symmetry of the background. This state also plays the role of the vacuum state, in the sense that it is the no-particle state.

As discussed in the introduction, in a generic curved spacetime, there is no unique notion of a vacuum state or a gravitational reference state. In this work, we therefore specialize to homogeneous and isotropic (FLRW) spacetimes in n-dimensions.

Assumption 1. *The background metric is that of an n-dimensional FLRW spacetime.*

In order to preserve the symmetries of FLRW spacetimes, the expectation value $\langle \hat{T}_{\mu\nu} \rangle$ can only have two independent non-zero components: the energy density $\rho = n^\mu n^\nu \langle \hat{T}_{\mu\nu} \rangle$, where n^μ is the unit normal to the homogeneous hyper-surfaces, and the pressure p defined by the relation $\langle \hat{T} \rangle = (n-1)\, p - \rho$. For most of this section, we will use the preferred

resolution of the cosmological constant problem.

foliation that exists on an FLRW spacetime such that the homogeneous hyper-surfaces are parametrized by the time coordinate $t \equiv x^0$ and $n^\mu = \sqrt{-g^{00}}\,(1, 0, ..., 0)$.

Similarly to the case of a Minkowski spacetime in (4.10), we propose to define an *effective*[3] expectation value of the stress-energy tensor by subtracting the expectation value on a *gravitational reference state*, in a way that also ensures that the resulting *effective* energy density that contributes to the Einstein equation is positive. The obvious choice is to subtract the stress-energy of the state with lowest energy density in the same background. In homogeneous spacetimes, minimizing the energy density is of course equivalent to minimizing the total energy, at any given time. We call the states that satisfy this property *ground states*[4] and we define them formally as follows.

Definition 1. *Given a quantum field theory on an FLRW spacetime, the* ***(instantaneous) ground state at time*** t *is defined as the vacuum state* $\left|0_{\mathrm{GS}(t)}\right\rangle$ *that respects the symmetries of the background metric and satisfies*

$$\delta_\psi \left(n^\mu n^\nu \left\langle \psi \right| \hat{T}_{\mu\nu}(t) \left| \psi \right\rangle \right) \Big|_{t;\, \psi = 0_{\mathrm{GS}(t)}} = 0 \,, \tag{4.11}$$

where the domain of variation δ_ψ *is the set of all vacuum states that respect the symmetries of the FLRW background.*

We assume the existence of ground states in the following and we discuss this assumption in Section 4.4.

Assumption 2. *An instantaneous ground state exists uniquely at each moment of time.*

The immediate concern in subtracting the stress-energy of the ground state is, however, that generically no single state minimizes the energy density $\rho(t)$ at all times simultaneously, in a non-stationary spacetime. The ground state at one time t_0 is an energetically excited state at another time t_1. One can only speak of an *instantaneous* ground state $\left|0_{\mathrm{GS}(t)}\right\rangle$ that minimizes the energy at a given time t, while the ground states at different times are generically different states – see the explicit example of ground state vacua provided in Appendix C.

[3] The reason for calling this quantity *effective* instead of *renormalized* will be explained in Section 4.3.4.

[4] In the literature, the term ground state is reserved for the eigenstate of the Hamiltonian operator with lowest eigenvalue, which might be different from the state with lowest energy density that we consider here. This distinction is particularly important if the quantum field is coupled to the curvature. The fact that we minimize the energy density will turn out to be important to preserve the Bianchi identity.

What we are proposing, therefore, is to define for each time, t, its own gravitational reference state, namely the energetic ground state at that time. Using this family $\left\{\left|0_{\mathrm{GS}(t)}\right\rangle, t \in \mathbb{R}\right\}$ of instantaneous ground states, we can define the *effective* expectation value of the stress-energy tensor by subtracting the ground state expectation value at every time, as measured by an inertial observer with no peculiar velocity,

$$\langle \hat{T}_{\mu\nu} \rangle_{\Psi}^{\text{eff.}}(t) \equiv \langle \hat{T}_{\mu\nu}(t) \rangle_{\Psi} - \langle \hat{T}_{\mu\nu}(t) \rangle_{\mathrm{GS}(t)} \, . \tag{4.12}$$

The counter-intuitive fact that this quantity is covariantly conserved is one of the main results of this Chapter and it will be proven in the next section as Theorem 1. We then propose that the source to the semiclassical Einstein equation for an FLRW background is the effective part (4.12) of the stress-energy tensor expectation value,

$$\boxed{\frac{1}{8\pi G} G_{\mu\nu} - \rho_{\Lambda} \, g_{\mu\nu} = \langle \hat{T}_{\mu\nu} \rangle_{\Psi}^{\text{eff.}} \, .} \tag{4.13}$$

4.3.2 Covariant conservation law

When we choose a time-dependent vacuum family for the subtraction as in (4.12), the major concern is preserving the consistency of the semiclassical Einstein equation.The left-hand side in (4.13) consists of covariantly conserved tensors. For any individual state, the expectation value $\langle \hat{T}_{\mu\nu} \rangle$ of the stress-energy tensor is also covariantly conserved by diffeomorphism invariance. However, this argument does not apply to the vacuum family expectation value $\langle \hat{T}_{\mu\nu} \rangle_{\mathrm{GS}(t)}$ because of the parametric time dependence of the state. The reader might expect the conservation law to be broken for this quantity.

This turns out not to be the case. We find that this is a non-trivial property of the ground state family on an FLRW background and summarize this result in the following theorem.

Theorem 1. *The ground state family expectation value of the stress-energy tensor is covariantly conserved on an FLRW spacetime,*

$$\nabla^{\mu} \langle \hat{T}_{\mu\nu}(t) \rangle_{\mathrm{GS}(t)} = 0 \, . \tag{4.14}$$

Proof. The line element on an n-dimensional FLRW spacetime is given by

$$\mathrm{d}s^2 = -\mathrm{d}t^2 + a(t)^2 \, \mathrm{d}\Sigma_{n-1}^2 \, . \tag{4.15}$$

where $\mathrm{d}\Sigma^2_{n-1}$ is the line element on each spatial section. For any time-parametrized family $\{|\psi_t\rangle\,, t \in \mathbb{R}\}$ of states that respect the homogeneity of the FLRW background, such as the ground states, we can write

$$\langle\psi_t|\,\hat{T}_{\mu\nu}(t)\,|\psi_t\rangle\,\mathrm{d}x^\mu\,\mathrm{d}x^\nu = \rho(t;\psi_t)\,\mathrm{d}t^2 + p(t;\psi_t)\,a(t)^2\,\mathrm{d}\Sigma^2_{n-1}\,, \tag{4.16}$$

where $\rho(t;\psi_t)$ is the energy density and $p(t;\psi_t)$ is the pressure at time t for each state $|\psi_t\rangle$. Writing the components of the covariant derivative explicitly for the ground state expectation values, we find

$$\begin{aligned}\nabla^\mu\langle\hat{T}_{\mu 0}(t)\rangle_{\mathrm{GS}(t)} &= (n-1)\,\frac{a'(t)}{a(t)}\left[\rho(t;0_{\mathrm{GS}(t)}) + p(t;0_{\mathrm{GS}(t)})\right] + \frac{\partial}{\partial t}\,\rho(t;0_{\mathrm{GS}(t)})\,, \\ \nabla^\mu\langle\hat{T}_{\mu j}(t)\rangle_{\mathrm{GS}(t)} &= 0\,.\end{aligned} \tag{4.17}$$

Since the spatial components of the covariant derivative vanish identically, we will focus on the time component.

There are two kinds of time-dependence in $\rho(t;0_{\mathrm{GS}(t)})$. Firstly, for each fixed ground state $\left|0_{\mathrm{GS}(u)}\right\rangle$ at time $u \in \mathbb{R}$, the expectation value $\rho(t;0_{\mathrm{GS}(u)}) \equiv \langle\hat{T}_{00}(t)\rangle_{\mathrm{GS}(u)}$ is a function of time t, since the operator $\hat{T}_{00}(t)$ evolves over time. The second one is the choice of the parameter u that specifies the time at which the state minimizes the energy density. Our proposal sets these two parameters equal, $u = t$. The same discussion applies to $p(t;0_{\mathrm{GS}(u)})$.

Let's distinguish between the parameters t and u for a moment and define $\theta = t - u$. The quantity $\rho(t;0_{\mathrm{GS}(u)})$ depends on two of these variables independently. The first term in (4.17) is understood as first setting $u = t$ and then taking the derivative with respect to t. This is equivalent to taking the partial derivative with respect to t while holding θ fixed and then setting $\theta = 0$,

$$\nabla^\mu\langle\hat{T}_{\mu 0}(t)\rangle_{\mathrm{GS}(t)} = \left[\frac{\partial\rho(t;0_{\mathrm{GS}(u)})}{\partial t}\bigg|_\theta + (n-1)\,\frac{a'(t)}{a(t)}\left(\rho(t;0_{\mathrm{GS}(u)}) + p(t;0_{\mathrm{GS}(u)})\right)\right]\bigg|_{u=t}\,. \tag{4.18}$$

On the other hand, the standard conservation law gives $\nabla^\mu\langle\hat{T}_{\mu 0}(t)\rangle_{\mathrm{GS}(u)} = 0$ for every fixed state, *i.e.*, for every fixed u. If we first evaluate the covariant derivative for fixed u and then set $u = t$, this becomes

$$0 = \left[\frac{\partial\rho(t;0_{\mathrm{GS}(u)})}{\partial t}\bigg|_u + (n-1)\,\frac{a'(t)}{a(t)}\left(\rho(t;0_{\mathrm{GS}(u)}) + p(t;0_{\mathrm{GS}(u)})\right)\right]\bigg|_{u=t}\,. \tag{4.19}$$

A simple calculation for the derivatives on the t-u-space shows that

$$\left.\frac{\partial f(t,u)}{\partial t}\right|_{\theta} = \left.\frac{\partial f(t,u)}{\partial t}\right|_{u} + \left.\frac{\partial f(t,u)}{\partial u}\right|_{t}, \tag{4.20}$$

for every scalar function f. Hence, if we subtract (4.18) from (4.19) and use (4.20), we get

$$\nabla^{\mu}\langle\hat{T}_{\mu 0}(t)\rangle_{\mathrm{GS}(t)} = \left.\frac{\partial\rho(t;0_{\mathrm{GS}(u)})}{\partial u}\right|_{t;\,u=t}. \tag{4.21}$$

Note that we have not used any properties of the ground states up to this point; thus (4.21) holds for any time-dependent family of states. The defining property of an instantaneous ground state $\left|0_{\mathrm{GS}(t)}\right\rangle$ at time t is that it minimizes the energy density $\rho(t)$ at that time among all states as in (4.11). This implies that $\left|0_{\mathrm{GS}(t)}\right\rangle$ also minimizes the instantaneous energy density $\rho(t)$ among the family $\left\{\left|0_{\mathrm{GS}(u)}\right\rangle, u\in\mathbb{R}\right\}$ of ground states at different times. Therefore, the right-hand side of (4.21) vanishes. □

In conclusion, Theorem 1 ensures that our proposal for the semiclassical Einstein equation in (4.12) and (4.13) is consistent with diffeomorphism invariance, *i.e.*, with the Bianchi identity. Note that the proof of Theorem 1 relies on diffeomorphism invariance for fixed states, since we use (4.19) to convert the time derivative at step (4.18) into a derivative over the state parameter at step (4.21).

4.3.3 Vacua in cosmology

Naively, one might expect that the momentary ground state is the vacuum state, *i.e.*, the no-particle state. However, in this case, the predicted amount of particle creation would exceed the upper bound from astrophysical observations (see [47, p. 73] and references therein). As a result, the instantaneous ground state and the related *Hamiltonian diagonalization* were ruled out as vacuum identification criteria. The lowest energy state and the physical no-particle state must be, therefore, distinct states for quantum field theories in generic curved backgrounds. For recent discussions on the topic of vacuum states in cosmology, see [125, 28, 90].

The physical vacuum states that are generally considered to be most plausible for cosmological backgrounds belong to the family of *adiabatic vacuum states*. These vacua are obtained by solving a certain perturbative expansion up to a finite number of derivatives of the metric components. See, *e.g.*, [160] for a rigorous definition of the concept. Originally, the adiabatic vacuum states were introduced in [196]. The basic idea is that the criterion

for identifying which state is the vacuum state at any given time, t, should be such that the amount of cosmological particle creation which is predicted as a consequence of applying this criterion is minimized.

The adiabatic vacuum identification criterion may also be motivated in a new way that is based on first-principles, *i.e.*, without the need to appeal to data. To this end, we begin with the intuition that, when the universe either expands or shrinks, any field state that possesses a nonzero particle content must in some way change over time, the change being due to the fact that the particle content of the state has to either dilute or concentrate. This yields a criterion for identifying the no-particle state. Namely, whatever the criterion for singling out the vacuum state at time t is, it should be such that, when applied over a range of times, the so-obtained vacuum states, parametrized by t, should change as little as possible - as determined via Bogoliubov β coefficients. This then implies the conventional adiabatic vacuum identification criterion: the amount of particle production should be minimal. In this new way, the vacuum is identified as the state that is most immune to dilution and concentration, so that all particle creation or annihilation that does happen due to expansion or shrinkage is solely due to quantum parametric excitation.

Technically, the procedure for identifying the adiabatic vacua is to solve a condition on the Wronskian of the mode function[5] by a WKB-type ansatz and to approach a solution of the equation of motion iteratively around a Minkowski-like 0-th order solution. A finite number s of iterations gives an approximate solution failing to be exact only by terms with at least $2s+2$ derivatives of the metric. The mode functions for the adiabatic vacua are then found by evaluating the initial conditions for the equation of motion along the approximate solutions. Hence, similarly to the ground state family, the adiabatic vacuum states $\left\{\left|0_{\mathrm{AV}(t)}\right\rangle, t \in \mathbb{R}\right\}$ are parametrized by the time at which they are defined. An explicit example of the adiabatic vacuum solution is provided in Appendix C.

The rigorous definition of adiabatic vacua in the literature has focused mostly on free theories, and might become non-trivial for generic quantum field theories. While we did not need to specify a physical vacuum state for our main proposal (4.13), we will rely on this concept in the following for discussing renormalization. Therefore, we include it here as our final assumption.

Assumption 3. *The adiabatic vacua exist at every time and are chosen as the physical vacuum states.*

[5]The Wronskian condition is obtained from the consistency requirement between the canonical commutation relations of the field operators and those of the annihilation and creation operators. More details can be found in the example in Appendix C.

Subtracting the physical – here taken to be the adiabatic – vacuum family expectation value should already give a renormalized (finite) stress-energy tensor, corresponding to the quantum and classical sources from observed fields,

$$\langle \hat{T}_{\mu\nu} \rangle_{\Psi}^{\text{ren.}}(t) \equiv \langle \hat{T}_{\mu\nu}(t) \rangle_{\Psi} - \langle \hat{T}_{\mu\nu}(t) \rangle_{\text{AV}(t)} \, . \tag{4.22}$$

Clearly, this is different from the *effective* part defined in (4.12). We can say that, while the effective part measures the gravitating stress-energy excitation, the renormalized part measures the stress-energy in particle excitation over the adiabatic vacuum. The difference between the two,

$$\begin{aligned} \langle \hat{T}_{\mu\nu} \rangle^{\text{vac.}}(t) &\equiv \langle \hat{T}_{\mu\nu} \rangle_{\Psi}^{\text{eff.}}(t) - \langle \hat{T}_{\mu\nu} \rangle_{\Psi}^{\text{ren.}}(t) \\ &= \langle \hat{T}_{\mu\nu}(t) \rangle_{\text{AV}(t)} - \langle \hat{T}_{\mu\nu}(t) \rangle_{\text{GS}(t)} \, , \end{aligned} \tag{4.23}$$

is independent of the particle content, *i.e.*, it is a purely geometrical contribution. It will be discussed in more detail in Section 4.3.4. Therefore, we can re-write the effective expectation value as the sum of two contributions,

$$\langle \hat{T}_{\mu\nu} \rangle_{\Psi}^{\text{eff.}} = \langle \hat{T}_{\mu\nu} \rangle_{\Psi}^{\text{ren.}} + \langle \hat{T}_{\mu\nu} \rangle^{\text{vac.}} \, . \tag{4.24}$$

See also the schematic representation in Figure 4.1. The first term, $\langle \hat{T}_{\mu\nu} \rangle_{\Psi}^{\text{ren.}}$, should match the observed sources of gravitation. This term should be finite, because the divergence in the expectation value on a state is the same as the divergence in its corresponding no-particle state [47]. We are therefore assuming that the particles described by Ψ are excitations of the adiabatic vacuum, *i.e.*, that the adiabatic vacuum is the physical no-particle state.

The second term in (4.24), the divergent piece $\langle \hat{T}_{\mu\nu} \rangle^{\text{vac.}}$, measures the elevation of the vacuum energy of the no-particle state above the ground state. After making this split in (4.12), we write the semiclassical Einstein equation (for an FLRW spacetime) as

$$\frac{1}{8\pi G} G_{\mu\nu} - \rho_{\Lambda} \, g_{\mu\nu} - \langle \hat{T}_{\mu\nu} \rangle^{\text{vac.}} = \langle \hat{T}_{\mu\nu} \rangle_{\Psi}^{\text{ren.}} \, . \tag{4.25}$$

The vacuum part $\langle \hat{T}_{\mu\nu} \rangle^{\text{vac.}}$ acts as a counter-term in this equation.

4.3.4 Renormalization

Both $\langle \hat{T}_{\mu\nu} \rangle_{\text{GS}(t)}$ and $\langle \hat{T}_{\mu\nu} \rangle_{\text{AV}(t)}$ only depend on the metric, *i.e.*, they are purely geometric quantities. The former is also covariantly conserved by Theorem 1. The only covariantly

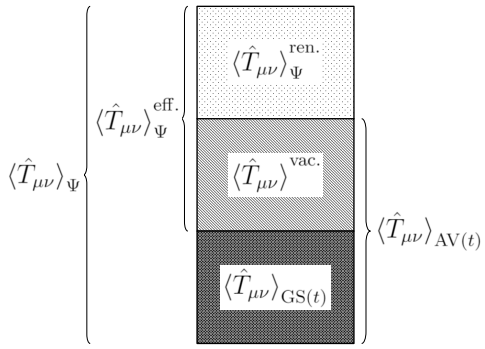

Figure 4.1: The total expectation value $\langle \hat{T}_{\mu\nu} \rangle_{\Psi}$ of the stress-energy tensor is split into various parts based on its ground state value and the (adiabatic) vacuum value. Note that $\langle \hat{T}_{\mu\nu} \rangle^{\text{vac.}}$ and $\langle \hat{T}_{\mu\nu} \rangle_{\text{GS}(t)}$ are infinite quantities.

conserved geometric tensors up to second order in derivatives of the metric are the metric itself $g_{\mu\nu}$ and the Einstein tensor $G_{\mu\nu}$. We can hence write

$$\langle \hat{T}_{\mu\nu} \rangle_{\text{GS}(t)} = \mathcal{A}_{\text{GS}}\, g_{\mu\nu} + \mathcal{B}_{\text{GS}}\, G_{\mu\nu} + \text{higher curv. terms} \,. \tag{4.26}$$

The quantity $\langle \hat{T}_{\mu\nu} \rangle_{\text{AV}(t)}$, on the other hand, is *not* exactly covariantly conserved. Nevertheless, we prove the following result:

Theorem 2. *For adiabatic vacua of at least 2nd order (at least $s \geq 1$ iteration), the adiabatic vacuum family expectation value of the stress-energy tensor ceases to be covariantly conserved only by terms that contain at least 4 derivatives of the metric. Schematically, we write this as*

$$\nabla^{\mu} \langle \hat{T}_{\mu\nu} \rangle_{\text{AV}(t)} = 0 + \mathcal{O}(\partial^4) \,. \tag{4.27}$$

Proof. Similarly to the proof of Theorem 1, we distinguish between the time parameter t on which the operator $\hat{T}_{\mu\nu}$ depends and the time parameter u at which an adiabatic vacuum state is defined, before setting $\theta \equiv t - u = 0$. Using again diffeomorphism invariance and

the relation (4.20) between derivatives, we obtain

$$\begin{aligned}\nabla^\mu \langle \hat{T}_{\mu\nu} \rangle_{\mathrm{AV}(t)} &= \nabla_\mu \langle \hat{T}^\mu{}_\nu(t) \rangle_{\mathrm{AV}(u)} \Big|_{\theta;\, u=t} \\ &= \left[\nabla_\mu \langle \hat{T}^\mu{}_\nu(t) \rangle_{\mathrm{AV}(u)} \Big|_u + \frac{\partial}{\partial u} \langle \hat{T}^0{}_\nu(t) \rangle_{\mathrm{AV}(u)} \Big|_t \right] \Big|_{u=t} \\ &= \frac{\partial}{\partial u} \langle \hat{T}^0{}_\nu(t) \rangle_{\mathrm{AV}(u)} \Big|_{t;\, u=t} . \end{aligned} \tag{4.28}$$

Now, recall that the approximate solution at s-th iteration, which is used to define the initial conditions for the adiabatic vacua, ceases to be an exact vacuum solution only at the order $\mathcal{O}(\partial^{2s+2})$. Hence, the adiabatic vacuum at $u + \delta u$ differs from the one at u at the equal time $t = u$ only by $\mathcal{O}(\partial^{2s+2})\, \delta u + \mathcal{O}(\delta u^2)$,

$$\nabla^\mu \langle \hat{T}_{\mu\nu} \rangle_{\mathrm{AV}(t)} = \mathcal{O}(\partial^{2s+2}) \, . \tag{4.29}$$

If we consider the adiabatic vacua at iteration $s \geq 1$, the statement of the theorem is proven. □

Using Theorem 2, we can write

$$\langle \hat{T}_{\mu\nu} \rangle_{\mathrm{AV}(t)} = \mathcal{A}_{\mathrm{AV}}\, g_{\mu\nu} + \mathcal{B}_{\mathrm{AV}}\, G_{\mu\nu} + \text{higher curv. terms}, \tag{4.30}$$

for the adiabatic vacuum family at iteration $s = 1$. The failure of conservation is completely contained in the higher curvature terms, which contain four derivatives of the metric.

The constant coefficients $\mathcal{A}_{\mathrm{GS}}$, $\mathcal{B}_{\mathrm{GS}}$, $\mathcal{A}_{\mathrm{AV}}$ and $\mathcal{B}_{\mathrm{AV}}$ are independent of the background geometry and can only depend on the parameters of the theory, such as the field mass. Moreover, we can prove the following result:

Theorem 3. *The instantaneous ground states and the adiabatic vacua coincide at the zero-th adiabatic order, i.e.,* $\mathcal{A}_{\mathrm{GS}} = \mathcal{A}_{\mathrm{AV}}$.

Proof. We smoothly flatten the FLRW background as follows: we replace the scale factor $a(t)$ with $a(t_0 + \epsilon(t - t_0))$ for arbitrary $t_0 \in \mathbb{R}$ and send ϵ to 0. The coefficients $\mathcal{A}_{\mathrm{GS}}$, $\mathcal{B}_{\mathrm{GS}}$, $\mathcal{A}_{\mathrm{AV}}$ and $\mathcal{B}_{\mathrm{AV}}$ are independent of ϵ. When ϵ reaches 0, the spacetime becomes flat and all curvature terms in (4.26) and (4.30) vanish. The Minkowski vacuum serves as both the ground state and the adiabatic vacuum on a Minkowski spacetime. Therefore, the expectation values $\langle \hat{T}_{\mu\nu} \rangle_{\mathrm{GS}(t)}$ and $\langle \hat{T}_{\mu\nu} \rangle_{\mathrm{AV}(t)}$ coincide with $\langle \hat{T}_{\mu\nu} \rangle_{\mathrm{M}}$ in the flat limit $\epsilon \to 0$. Since the two expectation values also converge to $\mathcal{A}_{\mathrm{GS}}\, g_{\mu\nu}$ and $\mathcal{A}_{\mathrm{AV}}\, g_{\mu\nu}$, respectively, we conclude that $\mathcal{A}_{\mathrm{GS}} = \mathcal{A}_{\mathrm{AV}}$. □

By Theorem 3, (4.23) becomes

$$\langle \hat{T}_{\mu\nu} \rangle^{\text{vac.}} = (\mathcal{B}_{\text{AV}} - \mathcal{B}_{\text{GS}})\, G_{\mu\nu} + \text{higher curv.} \tag{4.31}$$

Then, we may define the renormalized couplings for the semiclassical Einstein equation (4.25) as

$$\rho_{\Lambda}^{\text{ren.}} = \rho_{\Lambda} \quad \text{and} \quad G^{\text{ren.}} = \frac{G}{1 - 8\pi G\,(\mathcal{B}_{\text{AV}} - \mathcal{B}_{\text{GS}})}\,. \tag{4.32}$$

In accordance with the truncation of the Einstein-Hilbert action, we neglect the higher curvature terms in (4.31). After the renormalization of the parameters, the semiclassical Einstein equation (4.25) can finally be written as:

$$\frac{1}{8\pi G^{\text{ren.}}}\, G_{\mu\nu} - \rho_{\Lambda}^{\text{ren.}}\, g_{\mu\nu} = \langle \hat{T}_{\mu\nu} \rangle_{\Psi}^{\text{ren.}}\,. \tag{4.33}$$

By neglecting higher curvature terms, we are neglecting two features of the equation: firstly, higher curvature terms would contribute to the renormalization of the parameters of a higher curvature gravity theory, beyond the Einstein-Hilbert action. This problem is related to the perturbative non-renormalizability of gravity and is beyond the scope of this thesis. Secondly, the right-hand side of (4.33) fails to be covariantly conserved at higher-than-second adiabatic order, *i.e.*, at the neglected higher curvature terms. This violation of the Bianchi identity in the finite part is due entirely to the choice of adiabatic vacua to separate the finite part of the stress-energy tensor from the vacuum contribution, and does not appear if we consistently drop all terms beyond the selected level of adiabatic approximation.

The proposed scheme has direct consequences for the renormalization of the cosmological constant. Recall that the counter-term in (4.25) is a difference of the stress-energy tensor expectation values in the physical (adiabatic) vacuum and in the ground state. As we have shown in Section 4.3.4, and in (4.32) in particular, this counter-term does not affect the value of the parameter $\rho_{\Lambda} = \frac{1}{8\pi G}\Lambda$. This particular combination of parameters that is linearly related to the cosmological constant becomes protected from vacuum fluctuations. In this sense, our proposal contributes to the resolution of the cosmological constant problem, under the aforementioned assumptions.

4.4 Outlook

We have argued that the expectation value of the stress-energy in the instantaneous ground state, $\langle \hat{T}_{\mu\nu} \rangle_{\text{GS}(t)}$, is the good choice for the subtraction from the full stress-energy of the

actual state of the matter fields. We have put forward two reasons. Firstly, this subtraction, as in Eq. (4.12), ensures that the difference has a positive energy density, consistent with the weak energy condition. Secondly, the subtraction term $\langle \hat{T}_{\mu\nu} \rangle_{\mathrm{GS}(t)}$ is covariantly conserved exactly, as we have shown in Theorem 1.

We should note that, in our proposal, ground states and adiabatic vacua have different coefficients, $\mathcal{B}_{\mathrm{GS}}$ and $\mathcal{B}_{\mathrm{AV}}$, at second adiabatic order. This is due to the local curvature ambiguities in the definition of the stress-energy expectation value, as discussed in Wald's book [234]. Therefore, when we subtract the ground state family expectation value, we do not remove the vacuum contribution completely: $\langle \hat{T}_{\mu\nu} \rangle^{\mathrm{vac.}} \neq 0$. In this sense, we still allow vacuum fluctuations to play a role in the renormalization of gravity in curved backgrounds.

Throughout our exposition, we assumed that the universe is well described by an FLRW metric at cosmological scales, and that instantaneous ground states exist. Furthermore, we assumed the existence of adiabatic vacua as physical vacua in discussing the renormalization of the Einstein equation. In Appendix C, we analyze a free quantum field theory, where Assumptions 2 and 3 are shown explicitly to hold. For interacting theories, the definition and existence of ground states and adiabatic vacua might be more challenging. In specific theories, the one-loop order can be worked out following the techniques in [170]. Other free theories (spin-2, massive spin-1) were discussed in detail in our paper [240]. These results are not included in this thesis, as they mirror the ones obtained for a scalar field theory and presented in Appendix C. Gravitons (massless spin-2 fields) on a fixed curved background could also be quantized along the same lines, at least in the limit in which we can neglect their interactions. Free theories still provide important insights on the renormalization of the cosmological constant at different scales, *e.g.*, when considering new degrees of freedom that might come into play as the renormalization scale is dialed. In our proposal, the contribution of higher energy degrees of freedom to the cosmological constant will be canceled by the ground state expectation value, similarly to their low energy companions.

Another important approximation made in this proposal is that the universe is well described by an FLRW metric. The most striking result of this Chapter is perhaps Theorem 1, where we prove that the ground state family expectation value of the stress-energy tensor, $\langle \hat{T}_{\mu\nu} \rangle_{\mathrm{GS}(t)}$, is covariantly conserved on an FLRW background. It is tempting to search for a generalization of this result on arbitrarily curved spacetimes. Let us try to speculate on how this might be achieved. We specialize to $n = 4$ dimensions for convenience.

Since our Definition 1 of ground states already relies on cosmological backgrounds, we raise here the following question: what are the essential properties of ground states that are necessary for Theorem 1 to hold and that can be generalized to an arbitrary curved

spacetime?

We look for a generalization of ground states that shall extremize the local energy density. Since the local energy density will in general be extremized by a different state at each spacetime point when spacetime is not homogeneous, the generalized ground state family needs to be parametrized by 4 parameters instead of one. Given any spacetime manifold $\mathcal{M}$, we therefore look for a map $\mathcal{M} \to \mathcal{F}$, $u \mapsto |\psi_u\rangle$, where $\mathcal{F}$ is the Fock space for the quantum field theory under consideration and u is the vector of parameters spanning the states in the ground state family.

We want to define the states $|\psi_u\rangle$ in such a way that $\nabla_\mu \langle\psi_x| \hat{T}^{\mu\nu}(x) |\psi_x\rangle = 0$ holds in an open neighborhood of every point $x \in \mathcal{M}$. Using the methods outlined in the proof of Theorem 1, we get

$$\begin{aligned}
\nabla_\mu \langle \hat{T}^{\mu\nu}(x) \rangle_{\psi_x} &= \nabla_\mu \langle \hat{T}^{\mu\nu}(x) \rangle_{\psi_u} \Big|_{x-u;\, u=x} \\
&= \left(\nabla_\mu \langle \hat{T}^{\mu\nu}(x) \rangle_{\psi_u} \Big|_{x-u} - \nabla_\mu \langle \hat{T}^{\mu\nu}(x) \rangle_{\psi_u} \Big|_{u} \right) \Big|_{u=x} \\
&= \left(\frac{\partial \langle \hat{T}^{\mu\nu}(x) \rangle_{\psi_u}}{\partial x^\mu} \Big|_{x-u} - \frac{\partial \langle \hat{T}^{\mu\nu}(x) \rangle_{\psi_u}}{\partial x^\mu} \Big|_{u} \right) \Big|_{u=x} \\
&= \frac{\partial \langle \hat{T}^{\mu\nu}(x) \rangle_{\psi_u}}{\partial u^\mu} \Big|_{x;\, u=x} .
\end{aligned} \tag{4.34}$$

In the first line, we distinguished between the spacetime coordinate x, on which the operators depend in the Heisenberg picture, and the parameter u, which specifies the spacetime point where the generalized ground state $|\psi_u\rangle$ is defined. In the second line, we subtracted the covariant derivative at a fixed state, which is known to be zero by diffeomorphism invariance. The connection terms canceled in the third line. Finally, in the last line, we used the relation (4.20) between partial derivatives for each pair of parameters $(x^\mu, u^\mu)_{\mu=0,1,2,3}$.

If the last line in (4.34) is well-defined and equals zero, then $\langle\psi_x| \hat{T}^{\mu\nu}(x) |\psi_x\rangle$ is covariantly conserved. This could be taken as the definition of a ground state family in a generic spacetime. Hence, we could generalize Theorem 1 to hold for the states $\{|\psi_x\rangle\,,\, x \in \mathcal{M}\}$ in the image of any extremal map, and propose

$$\frac{1}{8\pi G}\, G_{\mu\nu}(x) - \rho_\Lambda\, g_{\mu\nu}(x) = \langle \hat{T}_{\mu\nu}(x) \rangle_\Psi - \langle \hat{T}^{\mu\nu}(x) \rangle_{\psi_x} \tag{4.35}$$

for the semiclassical Einstein equation on any curved background.

However, the definition of the generalized ground state family provided by Eq. (4.34) is highly non-restrictive. In particular, every constant map $|\psi_u\rangle = |\psi\rangle$ is extremal by definition. Recall that another feature of the ground states in FLRW spacetime was that the difference on the right hand side of the Einstein equation maintained a positive energy density for any state Ψ that respected the homogeneity of the background. One possible way to replace this additional condition and determine a unique generalized ground state among all extremal states would be to demand that the difference on the right-hand side of (4.35) satisfies the weak energy condition for any state Ψ in a suitable set. This is a subject for future research.

Chapter 5

Conclusions

In this thesis, we tackled a series of problems in gravitational physics, all relevant to current and future observations. The first part of the thesis focused on modeling the astrophysical phenomena expected to be relevant for low-frequency gravitational wave sources. We showed that accretion and dynamical friction induced by realistic gaseous environments (such as AGNs) could be detected in the gravitational-wave signal of stellar- and intermediate-mass black hole binaries with LISA. Our results were based on a Newtonian description, but relativistic effects could be included – Barausse derived the relativistic dynamical friction force, for instance, in Ref. [33]. The latter might become important at low or intermediate frequencies (accessible to the proposed mission DECIGO), and could help distinguish effects that are degenerate at leading order by their distinct contributions to higher order post-Newtonian terms. Our work, moreover, focused on the effect of the relative motion of the binary components on the gravitational wave phase. It would be interesting to explore the detectability of other effects, such as kicks imparted to the binary's center of mass [70], or modifications of the gravitational wave amplitude. Dark matter in the environment can also contribute in a similar way, through accretion and friction, to the evolution of black hole binaries. Further numerical simulations and analytic modeling will be required to asses the detectability of dark matter effects with gravitational waves, along the lines of Ref. [136].

One context, not explored in this thesis, where environmental effects might play a significant role is the inspiral of extreme-mass-ratio (EMRI) binaries. Pure gravitational models of the gravitational wave signal of EMRIs, based on the self-force approach, are on track to reaching second order accuracy in the mass ratio [203] for the LISA mission. At this level of accuracy, the numerous effects connected to the environment could become relevant for EMRIs spiraling in geometrically thin accretion disks [34]. These effects should

therefore be incorporated in self-force models, to ensure that these models realize their full potential for testing gravity at unprecedented levels.

In our explorations of the interplay of gravitational wave emission and environmental effects, we also discussed a class of binary systems where matter effects are not subleading contributions, but rather dominate the dynamics. We identified a new universal relation characterizing the long term evolution of white dwarf–black hole binaries, and used it to infer the binary parameters with (mock) LISA observations. The simple model neglected some of the features of the system, such as potential short-term disruptions in the accretion flow and potential tidal interactions between the black hole accretion disk and the star. We plan to explore how these uncertainties affect gravitational wave inference in the future. More importantly, we would like to identify similar universal relations in double white dwarf binaries, where the direct tidal coupling between the stars cannot be neglected. LISA (paired with electromagnetic follow-ups) has in general the potential to advance our understanding of many binary phases and astrophysical processes. Another interesting and little explored target are, in this sense, common envelope binaries.

The second part of this thesis was dedicated to the study of nonlinear effects in the culminating phase of black hole binary mergers, *i.e.*, the ringdown. We found that, at least for a scalar field coupled to gravity in AdS in spherical symmetry, nonlinearities predominantly affect the amplitude of linear modes. This might safeguard the standard analysis of the ringdown signal, which is based on linear mode combinations. Further explorations will however be necessary to understand how (and if) more exotic nonlinear behavior might set in for sufficiently strong perturbations, or when zero-damped modes emerge in the spectrum of extremal black holes. The analysis of the ringdown following binary mergers in numerical simulations has highlighted other little understood properties of quasi normal mode excitations. The modes identified by Giesler et al. [116], for instance, have amplitudes increasing with the overtone number. The single QNM amplitudes are also much higher than the total signal amplitude, to which they reduce via a coherent cancellation. This might indicate that the modes are excited in a somehow coherent way, something that has not been explored so far in the literature, except for extremal black holes [119].

Environmental effects can also affect the ringdown signal, providing an interesting link between the first and second part of this thesis. Plasma in particular, a common environment for astrophysical black holes, can influence the spectrum of linear perturbations of the electromagnetic field. Ref. [85] proposed that this phenomenon could lead to superradiant instabilities in astrophysical black holes, and speculated that these instabilities could be connected to fast radio bursts (FRBs). It was recently suggested, however, that nonlinear effects will quench the development of the instability [65].

The third and final part of the thesis developed a new renormalization scheme for the stress-energy tensor contributing to the semiclassical Einstein equation. This was shown to lead to a cancellation of the large contributions to the cosmological constant. The proposal was developed in the context of purely gravitating quantum fields on a homogeneous and isotropic (FLRW) background. A natural extension of this work would be therefore aimed at generalizing these results to less symmetrical backgrounds, and to interacting field theories.

The semiclassical approximation has received renewed attention in recent years, thanks to the development of a formalism to handle Lorentzian path integrals for gravity [107]. This approach promises to bring further insight into the implications of semiclassical gravity for cosmology, and could be perhaps used to derive (or invalidate) the results of this thesis from a Lagrangian perspective. Other interesting applications include the nucleation of black holes in a spacetime with a positive cosmological constant [53].

References

[1] http://rhcole.com/apps/GWplotter/.

[2] http://www.black-holes.org/waveforms.

[3] Ska white paper, 2014.

[4] The Lynx Mission Concept Study Interim Report. 2018.

[5] Kevork N. Abazajian and et al. Cmb-s4 science book, first edition, 2016.

[6] B. P. Abbott, R. Abbott, T. D. Abbott, F. Acernese, K. Ackley, C. Adams, T. Adams, P. Addesso, R. X. Adhikari, V. B. Adya, and et al. Gw170817: Observation of gravitational waves from a binary neutron star inspiral. *Physical Review Letters*, 119(16), Oct 2017.

[7] B. P. Abbott, R. Abbott, T. D. Abbott, F. Acernese, K. Ackley, C. Adams, T. Adams, P. Addesso, R. X. Adhikari, V. B. Adya, and et al. Tests of general relativity with gw170817. *Physical Review Letters*, 123(1), Jul 2019.

[8] B. P. Abbott et al. Binary Black Hole Population Properties Inferred from the First and Second Observing Runs of Advanced LIGO and Advanced Virgo. *The Astrophysical Journal*, 882(2):L24, sep 2019.

[9] B.P. Abbott, R. Abbott, T.D. Abbott, M.R. Abernathy, F. Acernese, K. Ackley, C. Adams, T. Adams, P. Addesso, R.X. Adhikari, and et al. Tests of general relativity with gw150914. *Physical Review Letters*, 116(22), May 2016.

[10] R. Abbott et al. GW190521: A Binary Black Hole Merger with a Total Mass of 150 $M_{\odot}$. *Phys. Rev. Lett.*, 125(10):101102, 2020.

[11] R. Abbott and et al. Gwtc-2: Compact binary coalescences observed by ligo and virgo during the first half of the third observing run, 2020.

[12] R. Abbott et al. Properties and astrophysical implications of the 150 Msun binary black hole merger GW190521. *Astrophys. J. Lett.*, 900:L13, 2020.

[13] R. Abbott et al. Tests of General Relativity with Binary Black Holes from the second LIGO-Virgo Gravitational-Wave Transient Catalog. 10 2020.

[14] R. Abuter, A. Amorim, N. Anugu, M. Baubck, M. Benisty, J. P. Berger, N. Blind, H. Bonnet, W. Brandner, and et al. Detection of the gravitational redshift in the orbit of the star s2 near the galactic centre massive black hole. *Astronomy & Astrophysics*, 615:L15, Jul 2018.

[15] R. Abuter, A. Amorim, M. Baubck, J. P. Berger, H. Bonnet, W. Brandner, V. Cardoso, Y. Clnet, P. T. de Zeeuw, and et al. Detection of the schwarzschild precession in the orbit of the star s2 near the galactic centre massive black hole. *Astronomy & Astrophysics*, 636:L5, Apr 2020.

[16] P. A. R. Ade, Z. Ahmed, R. W. Aikin, K. D. Alexander, D. Barkats, S. J. Benton, C. A. Bischoff, J. J. Bock, R. Bowens-Rubin, J. A. Brevik, and et al. Constraints on primordial gravitational waves using planck , wmap, and new bicep2/ keck observations through the 2015 season. *Physical Review Letters*, 121(22), Nov 2018.

[17] P. A. R. Ade et al. Planck 2015 results. XIII. Cosmological parameters. *Astron. Astrophys.*, 594:A13, 2016.

[18] Peter Ade, James Aguirre, Zeeshan Ahmed, Simone Aiola, Aamir Ali, David Alonso, Marcelo A. Alvarez, Kam Arnold, Peter Ashton, Jason Austermann, and et al. The simons observatory: science goals and forecasts. *Journal of Cosmology and Astroparticle Physics*, 2019(02):056056, Feb 2019.

[19] Y. Aghababaie, C.P. Burgess, S.L. Parameswaran, and F. Quevedo. Towards a naturally small cosmological constant from branes in 6d supergravity. *Nuclear Physics B*, 680(1-3):389414, Mar 2004.

[20] N. Aghanim, Y. Akrami, M. Ashdown, J. Aumont, C. Baccigalupi, M. Ballardini, A. J. Banday, R. B. Barreiro, N. Bartolo, and et al. Planck 2018 results. *Astronomy and Astrophysics*, 641:A6, Sep 2020.

[21] Ivan Agullo, Vitor Cardoso, Adrian del Rio, Michele Maggiore, and Jorge Pullin. Gravitational-wave signatures of quantum gravity, 2020.

[22] Romina Ahumada and et al. The 16th Data Release of the Sloan Digital Sky Surveys: First Release from the APOGEE-2 Southern Survey and Full Release of eBOSS Spectra. *The Astrophysical Journal, Supplement*, 249(1):3, July 2020.

[23] Yashar Akrami, Renata Kallosh, Andrei Linde, and Valeri Vardanyan. The landscape, the swampland and the era of precision cosmology. *Fortschritte der Physik*, 67(1-2):1800075, Nov 2018.

[24] Ahmed Almheiri, Donald Marolf, Joseph Polchinski, and James Sully. Black holes: complementarity or firewalls? *Journal of High Energy Physics*, 2013(2), Feb 2013.

[25] Luca Amendola, Stephen Appleby, Anastasios Avgoustidis, David Bacon, Tessa Baker, Marco Baldi, Nicola Bartolo, Alain Blanchard, Camille Bonvin, and et al. Cosmology and fundamental physics with the euclid satellite. *Living Reviews in Relativity*, 21(1), Apr 2018.

[26] James L. Anderson and David Finkelstein. Cosmological constant and fundamental length. *American Journal of Physics*, 39(8):901–904, 1971.

[27] Anuj Apte and Scott A. Hughes. Exciting black hole modes via misaligned coalescences. i. inspiral, transition, and plunge trajectories using a generalized ori-thorne procedure. *Physical Review D*, 100(8), Oct 2019.

[28] C. Armendariz-Picon and Eugene A. Lim. Vacuum choices and the predictions of inflation. *JCAP*, 0312:006, 2003.

[29] Zaven Arzoumanian and et al. The nanograv 12.5-year data set: Search for an isotropic stochastic gravitational-wave background, 2020.

[30] Gregory Ashton, Kendall Ackley, Ignacio Magaña Hernandez, and Brandon Piotrzkowski. Current observations are insufficient to confidently associate the binary black hole merger GW190521 with AGN J124942.3+344929. 9 2020.

[31] Heather Audley et al. Laser Interferometer Space Antenna. 2017.

[32] Vishal Baibhav, Emanuele Berti, Vitor Cardoso, and Gaurav Khanna. Black Hole Spectroscopy: Systematic Errors and Ringdown Energy Estimates. *Phys. Rev. D*, 97(4):044048, 2018.

[33] Enrico Barausse. Relativistic dynamical friction in a collisional fluid. *Mon. Not. Roy. Astron. Soc.*, 382:826–834, 2007.

[34] Enrico Barausse, Vitor Cardoso, and Paolo Pani. Can environmental effects spoil precision gravitational-wave astrophysics? *Phys. Rev.*, D89(10):104059, 2014.

[35] Enrico Barausse and Luciano Rezzolla. The Influence of the hydrodynamic drag from an accretion torus on extreme mass-ratio inspirals. *Phys. Rev.*, D77:104027, 2008.

[36] Enrico Barausse, Nicols Yunes, and Katie Chamberlain. Theory-Agnostic Constraints on Black-Hole Dipole Radiation with Multiband Gravitational-Wave Astrophysics. *Phys. Rev. Lett.*, 116(24):241104, 2016.

[37] A. Bédard, P. Bergeron, P. Brassard, and G. Fontaine. On the Spectral Evolution of Hot White Dwarf Stars. I. A Detailed Model-Atmosphere Analysis of Hot White Dwarfs from SDSS DR12. *arXiv e-prints*, page arXiv:2008.07469, August 2020.

[38] J. D. Bekenstein. The quantum mass spectrum of the Kerr black hole. *Lett. Nuovo Cim.*, 11:467, 1974.

[39] Jacob D. Bekenstein and V.F. Mukhanov. Spectroscopy of the quantum black hole. *Physics Letters B*, 360(1-2):7–12, Oct 1995.

[40] Emanuele Berti and Vitor Cardoso. Quasinormal ringing of kerr black holes: The excitation factors. *Physical Review D*, 74(10), Nov 2006.

[41] Emanuele Berti, Vitor Cardoso, and Andrei O. Starinets. TOPICAL REVIEW: Quasinormal modes of black holes and black branes. *Classical and Quantum Gravity*, 26(16):163001, August 2009.

[42] Emanuele Berti, Vitor Cardoso, and Clifford M. Will. On gravitational-wave spectroscopy of massive black holes with the space interferometer LISA. *Phys. Rev. D*, 73:064030, 2006.

[43] Gianfranco Bertone, Djuna Croon, Mustafa A. Amin, Kimberly K. Boddy, Bradley J. Kavanagh, Katherine J. Mack, Priyamvada Natarajan, Toby Opferkuch, Katelin Schutz, Volodymyr Takhistov, Christoph Weniger, and Tien-Tien Yu. Gravitational wave probes of dark matter: challenges and opportunities, 2019.

[44] B. Bertotti. On gravitational motion. *Nuovo Cim.*, 4(4):898–906, 1956.

[45] B. Bertotti and J. Plebanski. Theory of gravitational perturbations in the fast motion approximation. *Annals of Physics*, 11(2):169–200, October 1960.

[46] Swetha Bhagwat, Xisco Jimenez Forteza, Paolo Pani, and Valeria Ferrari. Ringdown overtones, black hole spectroscopy, and no-hair theorem tests. *Phys. Rev. D*, 101(4):044033, 2020.

[47] N. D. Birrell and P. C. W. Davies. *Quantum Fields in Curved Space*. Cambridge Monographs on Mathematical Physics. Cambridge Univ. Press, Cambridge, UK, 1984.

[48] Diego Blas and Samuel J. Witte. Quenching mechanisms of photon superradiance, 2020.

[49] Miles Blencowe. Semiclassical electrodynamics: A model for semiclassical gravity. *Phys. Rev. D*, 48:4800–4809, Nov 1993.

[50] M. Bordag, U. Mohideen, and V.M. Mostepanenko. New developments in the casimir effect. *Physics Reports*, 353(1-3):1205, Oct 2001.

[51] Pablo Bosch, Stephen R. Green, and Luis Lehner. Nonlinear evolution and final fate of charged antide sitter black hole superradiant instability. *Physical Review Letters*, 116(14), Apr 2016.

[52] Pablo Bosch, Stephen R. Green, Luis Lehner, and Hugo Roussille. Excited hairy black holes: Dynamical construction and level transitions. *Physical Review D*, 102(4), Aug 2020.

[53] Raphael Bousso and Stephen W. Hawking. Pair creation of black holes during inflation. *Physical Review D*, 54(10):6312–6322, Nov 1996.

[54] Michael Boyle et al. The SXS Collaboration catalog of binary black hole simulations. *Class. Quant. Grav.*, 36(19):195006, 2019.

[55] Michael Boyle, Daniel Hemberger, Dante A B Iozzo, Geoffrey Lovelace, Serguei Ossokine, Harald P Pfeiffer, Mark A Scheel, Leo C Stein, Charles J Woodford, Aaron B Zimmerman, and et al. The sxs collaboration catalog of binary black hole simulations. *Classical and Quantum Gravity*, 36(19):195006, Sep 2019.

[56] Katelyn Breivik, Scott Coughlin, Michael Zevin, Carl L. Rodriguez, Kyle Kremer, Claire S. Ye, Jeff J. Andrews, Michael Kurkowski, Matthew C. Digman, Shane L.

Larson, and et al. Cosmic variance in binary population synthesis. *The Astrophysical Journal*, 898(1):71, Jul 2020.

[57] Katelyn Breivik, Kyle Kremer, Michael Bueno, Shane L. Larson, Scott Coughlin, and Vassiliki Kalogera. Characterizing accreting double white dwarf binaries with the laser interferometer space antenna and gaia. *The Astrophysical Journal*, 854(1):L1, feb 2018.

[58] Léon Brillouin. La mécanique ondulatoire de Schrödinger; une méthode générale de resolution par approximations successives. *Compt. Rend. Hebd. Seances Acad. Sci.*, 183(1):24–26, 1926.

[59] J.David Brown and Claudio Teitelboim. Dynamical neutralization of the cosmological constant. *Physics Letters B*, 195(2):177 – 182, 1987.

[60] T S Bunch. Adiabatic regularisation for scalar fields with arbitrary coupling to the scalar curvature. *J. Phys. A: Mathematical and General*, 13(4):1297, 1980.

[61] C. P. Burgess. The Cosmological Constant Problem: Why it's hard to get Dark Energy from Micro-physics. In *Proceedings, 100th Les Houches Summer School: Post-Planck Cosmology: Les Houches, France, July 8 - August 2, 2013*, pages 149–197, 2015.

[62] C. G. Campbell. Tidal effects in twin-degenerate binaries. *Monthly Notices of the Royal Astronomical Society*, 207(3):433–443, 04 1984.

[63] Andrea Caputo, Laura Sberna, Alexandre Toubiana, Stanislav Babak, Enrico Barausse, Sylvain Marsat, and Paolo Pani. Gravitational-wave detection and parameter estimation for accreting black-hole binaries and their electromagnetic counterpart. *The Astrophysical Journal*, 892(2):90, Apr 2020.

[64] Andrea Caputo, Laura Sberna, Alexandre Toubiana, Stanislav Babak, Enrico Barausse, Sylvain Marsat, and Paolo Pani. Gravitational-wave detection and parameter estimation for accreting black-hole binaries and their electromagnetic counterpart. *Astrophys. J.*, 892(2):90, 2020.

[65] Vitor Cardoso, Wen di Guo, Caio F. B. Macedo, and Paolo Pani. The tune of the universe: the role of plasma in tests of strong-field gravity, 2020.

[66] Vitor Cardoso, Valentino F. Foit, and Matthew Kleban. Gravitational wave echoes from black hole area quantization. *Journal of Cosmology and Astroparticle Physics*, 2019(08):006?006, Aug 2019.

[67] Vitor Cardoso, Leonardo Gualtieri, Carlos Herdeiro, and Ulrich Sperhake. Exploring New Physics Frontiers Through Numerical Relativity. *Living Rev. Relativity*, 18:1, 2015.

[68] Vitor Cardoso, Roman Konoplya, and Jos P. S. Lemos. Quasinormal frequencies of schwarzschild black holes in antide sitter spacetimes: A complete study of the overtone asymptotic behavior. *Physical Review D*, 68(4), Aug 2003.

[69] Vitor Cardoso and Jos P. S. Lemos. Quasinormal modes of schwarzschild–anti-de sitter black holes: Electromagnetic and gravitational perturbations. *Physical Review D*, 64(8), Sep 2001.

[70] Vitor Cardoso and Caio F B Macedo. Drifting through the medium: kicks and self-propulsion of binaries within accretion discs and other environments. *Monthly Notices of the Royal Astronomical Society*, 498(2):1963–1972, Aug 2020.

[71] Vitor Cardoso, Caio F. B. Macedo, and Rodrigo Vicente. Eccentricity evolution of compact binaries and applications to gravitational-wave physics. *Phys. Rev. D*, 103:023015, 2021.

[72] Sean M. Carroll, William H. Press, and Edwin L. Turner. The cosmological constant. *Annual Review of Astronomy & Astrophysics*, 30:499–542, January 1992.

[73] Zack Carson and Kent Yagi. Multi-band gravitational wave tests of general relativity. 2019.

[74] J. S. F. Chan and Robert B. Mann. Scalar wave falloff in asymptotically anti-de Sitter backgrounds. *Phys. Rev. D*, 55:7546–7562, 1997.

[75] S. Chandrasekhar. The mathematical theory of black holes. pages 5–26, 1984.

[76] Xian Chen and Zhe-Feng Shen. Retrieving the True Masses of Gravitational-wave Sources. *MDPI Proc.*, 17(1):4, 2019.

[77] S. L. Cherkas and V. L. Kalashnikov. Determination of the UV cut-off from the observed value of the Universe acceleration. *J. Cosmol. Astropart. Phys.*, 0701:028, 2007.

[78] Ross P. Church, Jay Strader, Melvyn B. Davies, and Alexey Bobrick. Formation constraints indicate a black-hole accretor in 47 Tuc X9. *Astrophys. J. Lett.*, 851:L4, 2017.

[79] Timothy Clifton, Pedro G. Ferreira, Antonio Padilla, and Constantinos Skordis. Modified gravity and cosmology. *Physics Reports*, 513(1-3):1189, Mar 2012.

[80] Sidney R. Coleman. Why There Is Nothing Rather Than Something: A Theory of the Cosmological Constant. *Nucl. Phys. B*, 310:643–668, 1988.

[81] DESI Collaboration. The desi experiment part i: Science,targeting, and survey design, 2016.

[82] KAGRA Collaboration. Overview of kagra : Kagra science, 2020.

[83] The LIGO Scientific Collaboration and the Virgo Collaboration. Population properties of compact objects from the second ligo-virgo gravitational-wave transient catalog, 2020.

[84] The LIGO Scientific Collaboration and the Virgo Collaboration. Tests of general relativity with binary black holes from the second ligo-virgo gravitational-wave transient catalog, 2020.

[85] Joseph P. Conlon and Carlos A.R. Herdeiro. Can black hole superradiance be induced by galactic plasmas? *Physics Letters B*, 780:169–173, May 2018.

[86] Gregory B. Cook. Aspects of multimode Kerr ringdown fitting. *Phys. Rev. D*, 102(2):024027, 2020.

[87] Neil J. Cornish and Tyson B. Littenberg. Tests of Bayesian Model Selection Techniques for Gravitational Wave Astronomy. *Phys. Rev. D*, 76:083006, 2007.

[88] National Research Council. *New Worlds, New Horizons in Astronomy and Astrophysics*. The National Academies Press, Washington, DC, 2010.

[89] Curt Cutler and Éanna E. Flanagan. Gravitational waves from merging compact binaries: How accurately can one extract the binary's parameters from the inspiral waveform? *Phys. Rev. D*, 49:2658–2697, Mar 1994.

[90] Ulf H. Danielsson. A Note on inflation and transPlanckian physics. *Phys. Rev.*, D66:023511, 2002.

[91] Christopher J. Deloye and Lars Bildsten. White dwarf donors in ultracompact binaries: The stellar structure of finite-entropy objects. *The Astrophysical Journal*, 598(2):12171228, Dec 2003.

[92] G. Desvignes and et al. High-precision timing of 42 millisecond pulsars with the European Pulsar Timing Array. *Monthly Notices of the Royal Astronomical Society*, 458(3):3341–3380, 03 2016.

[93] Arnab Dhani. Importance of mirror modes in binary black hole ringdown waveform. 10 2020.

[94] Alice Di Tucci, Job Feldbrugge, Jean-Luc Lehners, and Neil Turok. Quantum Incompleteness of Inflation. *Phys. Rev.*, D100(6), 2019.

[95] Yi-Ze Dong, Wei-Min Gu, Tong Liu, and Junfeng Wang. A black hole-white dwarf compact binary model for long gamma-ray bursts without supernova association. *Monthly Notices of the Royal Astronomical Society*, 475(1):L101–L105, March 2018.

[96] John F. Donoghue. Introduction to the effective field theory description of gravity. In *Advanced School on Effective Theories Almunecar, Spain, June 25-July 1, 1995*, 1995.

[97] Olaf Dreyer, Bernard J. Kelly, Badri Krishnan, Lee Samuel Finn, David Garrison, and Ramon Lopez-Aleman. Black hole spectroscopy: Testing general relativity through gravitational wave observations. *Class. Quant. Grav.*, 21:787–804, 2004.

[98] Serge Droz, Daniel J. Knapp, Eric Poisson, and Benjamin J. Owen. Gravitational waves from inspiraling compact binaries: Validity of the stationary-phase approximation to the fourier transform. *Physical Review D*, 59(12), May 1999.

[99] Kazunari Eda, Yousuke Itoh, Sachiko Kuroyanagi, and Joseph Silk. Gravitational waves as a probe of dark matter minispikes. *Physical Review D*, 91(4), Feb 2015.

[100] G. Efstathiou. A Lockdown Perspective on the Hubble Tension (with comments from the SH0ES team). 7 2020.

[101] P. P. Eggleton. Aproximations to the radii of Roche lobes. *The Astrophysical Journal*, 268:368–369, May 1983.

[102] A. Einstein and L. Infeld. On the motion of particles in general relativity theory. *Canadian Journal of Mathematics*, 1(3):209241, 1949.

[103] Reed Essick, Ingo Tews, Philippe Landry, Sanjay Reddy, and Daniel E. Holz. Direct astrophysical tests of chiral effective field theory at supranuclear densities, 2020.

[104] Event Horizon Telescope Collaboration. First M87 Event Horizon Telescope Results. I. The Shadow of the Supermassive Black Hole. *The Astrophysical Journal, Letters*, 875(1):L1, April 2019.

[105] Jose Mara Ezquiaga, Daniel E. Holz, Wayne Hu, Macarena Lagos, and Robert M. Wald. Phase effects from strong gravitational lensing of gravitational waves, 2020.

[106] Yun Fang, Xian Chen, and Qing-Guo Huang. Impact of a spinning supermassive black hole on the orbit and gravitational waves of a nearby compact binary. *The Astrophysical Journal*, 887(2):210, Dec 2019.

[107] Job Feldbrugge, Jean-Luc Lehners, and Neil Turok. Lorentzian quantum cosmology. *Physical Review D*, 95(10), May 2017.

[108] F. Feroz, M. P. Hobson, and M. Bridges. MultiNest: an efficient and robust Bayesian inference tool for cosmology and particle physics. *Mon. Not. Roy. Astron. Soc.*, 398:1601–1614, 2009.

[109] Eanna E. Flanagan and Scott A. Hughes. Measuring gravitational waves from binary black hole coalescences: 2. The Waves' information and its extraction, with and without templates. *Phys. Rev.*, D57:4566–4587, 1998.

[110] Valentino F Foit and Matthew Kleban. Testing quantum black holes with gravitational waves. *Classical and Quantum Gravity*, 36(3):035006, Jan 2019.

[111] Francois Foucart. A brief overview of black hole-neutron star mergers. *Frontiers in Astronomy and Space Sciences*, 7:46, 2020.

[112] J. Frank, A. King, and D. J. Raine. *Accretion Power in Astrophysics: Third Edition*. January 2002.

[113] Stephen A. Fulling. *Aspects of Quantum Field Theory in Curved Spacetime*. London Mathematical Society Student Texts. Cambridge University Press, 1989.

[114] Walter Gautschi. Computational aspects of three-term recurrence relations. *SIAM Review*, 9(1):24–82, 1967.

[115] G. Ghirlanda, O. S. Salafia, Z. Paragi, M. Giroletti, J. Yang, B. Marcote, J. Blanchard, I. Agudo, T. An, M. G. Bernardini, and et al. Compact radio emission indicates a structured jet was produced by a binary neutron star merger. *Science*, 363(6430):968971, Feb 2019.

[116] Matthew Giesler, Maximiliano Isi, Mark Scheel, and Saul Teukolsky. Black hole ringdown: the importance of overtones. *Phys. Rev.*, X9(4):041060, 2019.

[117] Giuseppe Gnocchi, Andrea Maselli, Tiziano Abdelsalhin, Nicola Giacobbo, and Michela Mapelli. Bounding Alternative Theories of Gravity with Multi-Band GW Observations. 2019.

[118] M. J. Graham, K. E. S. Ford, B. McKernan, N. P. Ross, D. Stern, K. Burdge, et al. Candidate electromagnetic counterpart to the binary black hole merger gravitational-wave event s190521g. *Phys. Rev. Lett.*, 124:251102, Jun 2020.

[119] Samuel E. Gralla, Aaron Zimmerman, and Peter Zimmerman. Transient instability of rapidly rotating black holes. *Physical Review D*, 94(8), Oct 2016.

[120] Stephen R. Green, Federico Carrasco, and Luis Lehner. Holographic path to the turbulent side of gravity. *Physical Review X*, 4(1), Jan 2014.

[121] Stephen R. Green, Stefan Hollands, and Peter Zimmerman. Private communication, to appear.

[122] Stephen R. Green, Stefan Hollands, and Peter Zimmerman. Teukolsky formalism for nonlinear Kerr perturbations. *Class. Quant. Grav.*, 37(7):075001, 2020.

[123] Andrei Gruzinov, Yuri Levin, and Christopher D. Matzner. Negative Dynamical Friction on compact objects moving through dense gas. 2019.

[124] M. Grbner, W. Ishibashi, S. Tiwari, M. Haney, and P. Jetzer. Binary black hole mergers in agn accretion discs: gravitational wave rate density estimates. *Astronomy & Astrophysics*, 638:A119, Jun 2020.

[125] W. J. Handley, A. N. Lasenby, and M. P. Hobson. Novel quantum initial conditions for inflation. *Phys. Rev.*, D94(2):024041, 2016.

[126] J. B. Hartle and S. W. Hawking. Wave Function of the Universe. *Phys. Rev.*, D28:2960–2975, 1983. [Adv. Ser. Astrophys. Cosmol.3,174(1987)].

[127] Tilman Hartwig, Marta Volonteri, Volker Bromm, Ralf S. Klessen, Enrico Barausse, Mattis Magg, and Athena Stacy. Gravitational Waves from the Remnants of the First Stars. *Mon. Not. Roy. Astron. Soc.*, 460(1):L74–L78, 2016.

[128] G Hobbs, A Archibald, Z Arzoumanian, D Backer, M Bailes, N D R Bhat, M Burgay, S Burke-Spolaor, D Champion, I Cognard, and et al. The international pulsar timing array project: using pulsars as a gravitational wave detector. *Classical and Quantum Gravity*, 27(8):084013, Apr 2010.

[129] Stefan Hollands and Robert M. Wald. Quantum fields in curved spacetime. *Physics Reports*, 574:135, Apr 2015.

[130] Gary T. Horowitz and Veronika E. Hubeny. Quasinormal modes of ads black holes and the approach to thermal equilibrium. *Physical Review D*, 62(2), Jun 2000.

[131] Jarrod R. Hurley, Christopher A. Tout, and Onno R. Pols. Evolution of binary stars and the effect of tides on binary populations. *Monthly Notices of the Royal Astronomical Society*, 329(4):897928, Feb 2002.

[132] Zeljko Ivezic, Steven M. Kahn, J. Anthony Tyson, Bob Abel, Emily Acosta, Robyn Allsman, David Alonso, Yusra AlSayyad, Scott F. Anderson, John Andrew, and et al. Lsst: From science drivers to reference design and anticipated data products. *The Astrophysical Journal*, 873(2):111, Mar 2019.

[133] R. L. Jaffe. Casimir effect and the quantum vacuum. *Physical Review D*, 72(2), Jul 2005.

[134] G. H. Janssen, G. Hobbs, M. McLaughlin, C. G. Bassa, A. T. Deller, M. Kramer, K. J. Lee, C. M. F. Mingarelli, P. A. Rosado, S. Sanidas, A. Sesana, L. Shao, I. H. Stairs, B. W. Stappers, and J. P. W. Verbiest. Gravitational wave astronomy with the ska, 2014.

[135] Xisco Jiménez Forteza, Swetha Bhagwat, Paolo Pani, and Valeria Ferrari. Spectroscopy of binary black hole ringdown using overtones and angular modes. *Phys. Rev. D*, 102(4):044053, 2020.

[136] Bradley J. Kavanagh, David A. Nichols, Gianfranco Bertone, and Daniele Gaggero. Detecting dark matter around black holes with gravitational waves: Effects of dark-matter dynamics on the gravitational waveform. *Physical Review D*, 102(8), Oct 2020.

[137] Seiji Kawamura and et al. Current status of space gravitational wave antenna decigo and b-decigo, 2020.

[138] Ali Kaya and Merve Tarman. Stress-energy tensor of adiabatic vacuum in friedmann-robertson-walker spacetimes. *J. Cosmol. Astropart. Phys.*, 2011(04):040, apr 2011.

[139] Matthew Kerr, Daniel J. Reardon, George Hobbs, Ryan M. Shannon, Richard N. Manchester, Shi Dai, Christopher J. Russell, Songbo Zhang, Willem van Straten, Stefan Osowski, and et al. The parkes pulsar timing array project: second data release. *Publications of the Astronomical Society of Australia*, 37, 2020.

[140] C Kiefer, T Padmanabhan, and T P Singh. A comparison between semiclassical gravity and semiclassical electrodynamics. *Classical and Quantum Gravity*, 8(8):L185–L192, aug 1991.

[141] Hyosun Kim and Woong-Tae Kim. Dynamical Friction of a Circular-Orbit Perturber in a Gaseous Medium. *Astrophys. J.*, 665:432–444, 2007.

[142] Hyosun Kim, Woong-Tae Kim, and F. J. Sanchez-Salcedo. Dynamical Friction of Double Perturbers in a Gaseous Medium. *Astrophys. J.*, 679:L33, 2008.

[143] Bence Kocsis, Nicolas Yunes, and Abraham Loeb. Observable Signatures of EMRI Black Hole Binaries Embedded in Thin Accretion Disks. *Phys. Rev. D*, 84:024032, 2011.

[144] Jurjen F. Koksma and Tomislav Prokopec. The cosmological constant and lorentz invariance of the vacuum state, 2011.

[145] Yoshihide Kozai. Secular perturbations of asteroids with high inclination and eccentricity. *Astron. J.*, 67:591–598, November 1962.

[146] H. A. Kramers. Wellenmechanik und halbzahlige Quantisierung. *Zeitschrift fur Physik*, 39(10-11):828–840, October 1926.

[147] Kyle Kremer, Sourav Chatterjee, Katelyn Breivik, Carl L. Rodriguez, Shane L. Larson, and Frederic A. Rasio. LISA Sources in Milky Way Globular Clusters. *Phys. Rev. Lett.*, 120(19):191103, 2018.

[148] A. Lamberts, S. Garrison-Kimmel, P. F. Hopkins, E. Quataert, J. S. Bullock, C. A. Faucher-Giguère, A. Wetzel, D. Kereš, K. Drango, and R. E. Sand erson. Predicting the binary black hole population of the Milky Way with cosmological simulations. *Monthly Notices of the Royal Astronomical Society*, 480(2):2704–2718, October 2018.

[149] L. D. Landau and E. M Lifshitz. *Course on theoretical Physics: Mechanics*. Wiley, 1960.

[150] Muhammad A. Latif and Andrea Ferrara. Formation of supermassive black hole seeds. *Publ. Astron. Soc. Austral.*, 33:e051, 2016.

[151] E. W. Leaver. Solutions to a generalized spheroidal wave equation: Teukolsky's equations in general relativity, and the two-center problem in molecular quantum mechanics. *Journal of Mathematical Physics*, 27(5):1238–1265, 1986.

[152] E. W. Leaver and Subrahmanyan Chandrasekhar. An analytic representation for the quasi-normal modes of kerr black holes. *Proceedings of the Royal Society of London. A. Mathematical and Physical Sciences*, 402(1823):285–298, 1985.

[153] Edward W. Leaver. Spectral decomposition of the perturbation response of the schwarzschild geometry. *Phys. Rev. D*, 34:384–408, Jul 1986.

[154] Nathan W. C. Leigh, Alison Sills, and Torsten Boker. Modifying two-body relaxation in N-body systems by gas accretion. *Mon. Not. Roy. Astron. Soc.*, 433:1958, 2013.

[155] M.L. Lidov. The evolution of orbits of artificial satellites of planets under the action of gravitational perturbations of external bodies. *Planetary and Space Science*, 9(10):719 – 759, 1962.

[156] Halston Lim, Gaurav Khanna, Anuj Apte, and Scott A. Hughes. Exciting black hole modes via misaligned coalescences. ii. the mode content of late-time coalescence waveforms. *Physical Review D*, 100(8), Oct 2019.

[157] Lee Lindblom, Benjamin J. Owen, and Duncan A. Brown. Model Waveform Accuracy Standards for Gravitational Wave Data Analysis. *Phys. Rev.*, D78:124020, 2008.

[158] LISA Science Study Team. LISA Science Requirements Document. https://www.cosmos.esa.int/documents/678316/1700384/SciRD.pdf/25831f6b-3c01-e215-5916-4ac6e4b306fb?t=1526479841000, 2018.

[159] Nicholas Loutrel, Justin L. Ripley, Elena Giorgi, and Frans Pretorius. Second order perturbations of kerr black holes: Reconstruction of the metric. 2020.

[160] Christian Lüders and John E. Roberts. Local quasiequivalence and adiabatic vacuum states. *Commun. Math. Phys.*, 134(1):29–63, Nov 1990.

[161] Thomas J. Maccarone, Arunav Kundu, Stephen E. Zepf, and Katherine L. Rhode. A black hole in a globular cluster. *Nature*, 445(7124):183–185, January 2007.

[162] Caio F.B. Macedo, Paolo Pani, Vitor Cardoso, and Luís C.B. Crispino. Into the lair: gravitational-wave signatures of dark matter. *Astrophys. J.*, 774:48, 2013.

[163] Piero Madau and Martin J. Rees. Massive black holes as Population III remnants. *Astrophys. J.*, 551:L27–L30, 2001.

[164] M. Maggiore. *Gravitational Waves: Volume 1: Theory and Experiments*. Oxford University Press, 2008.

[165] Michele Maggiore, Chris Van Den Broeck, Nicola Bartolo, Enis Belgacem, Daniele Bertacca, Marie Anne Bizouard, Marica Branchesi, Sebastien Clesse, Stefano Foffa, Juan Garca-Bellido, and et al. Science case for the einstein telescope. *Journal of Cosmology and Astroparticle Physics*, 2020(03):050050, Mar 2020.

[166] Alberto Mangiagli, Antoine Klein, Matteo Bonetti, Michael L. Katz, Alberto Sesana, Marta Volonteri, Monica Colpi, Sylvain Marsat, and Stanislav Babak. On the inspiral of coalescing massive black hole binaries with LISA in the era of Multi-Messenger Astrophysics. 6 2020.

[167] Alberto Mangiagli, Antoine Klein, Alberto Sesana, Enrico Barausse, and Monica Colpi. Post-Newtonian phase accuracy requirements for stellar black hole binaries with LISA. *Phys. Rev.*, D99(6):064056, 2019.

[168] Michela Mapelli. Massive black hole binaries from runaway collisions: the impact of metallicity. *Mon. Not. Roy. Astron. Soc.*, 459(4):3432–3446, 2016.

[169] Pablo Marchant, Norbert Langer, Philipp Podsiadlowski, Thomas M. Tauris, and Takashi J. Moriya. A new route towards merging massive black holes. *Astron. Astrophys.*, 588:A50, 2016.

[170] Tommi Markkanen and Anders Tranberg. A Simple Method for One-Loop Renormalization in Curved Space-Time. *JCAP*, 1308:045, 2013.

[171] Thomas Richard Marsh, G. Nelemans, and D. Steeghs. Mass transfer between double white dwarfs. *Mon. Not. Roy. Astron. Soc.*, 350:113, 2004.

[172] Jrme Martin. Everything you always wanted to know about the cosmological constant problem (but were afraid to ask). *Comptes Rendus Physique*, 13(6-7):566665, Jul 2012.

[173] R. McElreath. *Statistical Rethinking: A Bayesian Course with Examples in R and Stan*. Chapman & Hall/CRC Texts in Statistical Science. CRC Press, 2016.

[174] Sean McGee, Alberto Sesana, and Alberto Vecchio. The assembly of cosmic structure from baryons to black holes with joint gravitational-wave and X-ray observations. 2018.

[175] Barry McKernan, K. E. Saavik Ford, J. Bellovary, N. W. C. Leigh, Z. Haiman, B. Kocsis, W. Lyra, M. M. Mac Low, B. Metzger, M. O'Dowd, S. Endlich, and D. J. Rosen. Constraining Stellar-mass Black Hole Mergers in AGN Disks Detectable with LIGO. *The Astrophysical Journal*, 866(1):66, Oct 2018.

[176] Jianwei Mei, Yan-Zheng Bai, Jiahui Bao, Enrico Barausse, Lin Cai, Enrico Canuto, Bin Cao, Wei-Ming Chen, Yu Chen, Yan-Wei Ding, and et al. The tianqin project: Current progress on science and technology. *Progress of Theoretical and Experimental Physics*, Aug 2020.

[177] N. Meidinger. The Wide Field Imager instrument for Athena. *Contributions of the Astronomical Observatory Skalnate Pleso*, 48(3):498–505, Jul 2018.

[178] Norbert Meidinger, Josef Eder, Tanja Eraerds, Kirpal Nandra, Daniel Pietschner, Markus Plattner, Arne Rau, and Rafael Strecker. The wide field imager instrument for athena, 2017.

[179] Mar Mezcua. Observational evidence for intermediate-mass black holes. *International Journal of Modern Physics D*, 26(11):1730021, Jan 2017.

[180] M. Coleman Miller and Douglas P. Hamilton. Production of intermediate-mass black holes in globular clusters. *Mon. Not. Roy. Astron. Soc.*, 330:232, 2002.

[181] J. C. A. Miller-Jones, J. Strader, C. O. Heinke, T. J. Maccarone, M. van den Berg, C. Knigge, L. Chomiuk, E. Noyola, T. D. Russell, A. C. Seth, and G. R. Sivakoff. Deep radio imaging of 47 Tuc identifies the peculiar X-ray source X9 as a new black hole candidate. *Monthly Notices of the Royal Astronomical Society*, 453(4):3918–3931, 09 2015.

[182] Kimball A Milton. The casimir effect: recent controversies and progress. *Journal of Physics A: Mathematical and General*, 37(38):R209R277, Sep 2004.

[183] Philipp Moesta, Daniela Alic, Luciano Rezzolla, Olindo Zanotti, and Carlos Palenzuela. On the Detectability of Dual Jets from Binary Black Holes. *The Astrophysical Journal Letters*, 749(2):L32, Apr 2012.

[184] K. P. Mooley, A. T. Deller, O. Gottlieb, E. Nakar, G. Hallinan, S. Bourke, D. A. Frail, A. Horesh, A. Corsi, and K. Hotokezaka. Superluminal motion of a relativistic jet in the neutron-star merger gw170817. *Nature*, 561(7723):355359, Sep 2018.

[185] C J Moore, R H Cole, and C P L Berry. Gravitational-wave sensitivity curves. *Classical and Quantum Gravity*, 32(1):015014, Dec 2014.

[186] Christopher J. Moore, Davide Gerosa, and Antoine Klein. Are stellar-mass black-hole binaries too quiet for LISA? *Mon. Not. Roy. Astron. Soc.*, 488(1):L94–L98, 2019.

[187] Pierre Mourier, Xisco Jimenez-Forteza, Daniel Pook-Kolb, Badri Krishnan, and Erik Schnetter. Quasi-normal modes and their overtones at the common horizon in a binary black hole merger. 10 2020.

[188] G. Nelemans, L. R. Yungelson, and S. F. Portegies Zwart. The gravitational wave signal from the Galactic disk population of binaries containing two compact objects. *A&A*, 375:890–898, September 2001.

[189] Hans-Peter Nollert. Quasinormal modes: the characteristic sound of black holes and neutron stars. *Classical and Quantum Gravity*, 16(12):R159–R216, nov 1999.

[190] Maria Okounkova. Revisiting non-linearity in binary black hole mergers. 4 2020.

[191] G. Ossola and A. Sirlin. Considerations concerning the contributions of fundamental particles to the vacuum energy density. *Eur. Phys. J. C - Particles and Fields*, 31(2):165–175, Nov 2003.

[192] Eve C. Ostriker. Dynamical friction in a gaseous medium. *Astrophys. J.*, 513:252, 1999.

[193] Iara Ota and Cecilia Chirenti. Overtones or higher harmonics? Prospects for testing the no-hair theorem with gravitational wave detections. *Phys. Rev. D*, 101(10):104005, 2020.

[194] Antonio Padilla. Lectures on the Cosmological Constant Problem. 2015.

[195] Carlos Palenzuela, Luis Lehner, and Steven L. Liebling. Dual Jets from Binary Black Holes. *Science*, 329:927, 2010.

[196] L. Parker and S. A. Fulling. Adiabatic regularization of the energy momentum tensor of a quantized field in homogeneous spaces. *Phys. Rev.*, D9:341–354, 1974.

[197] Saul Perlmutter, Michael S. Turner, and Martin White. Constraining dark energy with type ia supernovae and large-scale structure. *Physical Review Letters*, 83(4):670–673, Jul 1999.

[198] P. C. Peters. Gravitational Radiation and the Motion of Two Point Masses. *Phys. Rev.*, 136:B1224–B1232, 1964.

[199] E. Pian, P. DAvanzo, S. Benetti, M. Branchesi, E. Brocato, S. Campana, E. Cappellaro, S. Covino, V. DElia, J. P. U. Fynbo, and et al. Spectroscopic identification of r-process nucleosynthesis in a double neutron-star merger. *Nature*, 551(7678):6770, Oct 2017.

[200] Anthony L. Piro, Phil Arras, and Lars Bildsten. White dwarf heating and subsequent cooling in dwarf nova outbursts. *Astrophys. J.*, 628:401–410, 2005.

[201] Daniel Pook-Kolb, Ofek Birnholtz, Jose Luis Jaramillo, Badri Krishnan, and Erik Schnetter. Horizons in a binary black hole merger i: Geometry and area increase, 2020.

[202] Daniel Pook-Kolb, Ofek Birnholtz, Jose Luis Jaramillo, Badri Krishnan, and Erik Schnetter. Horizons in a binary black hole merger ii: Fluxes, multipole moments and stability, 2020.

[203] Adam Pound, Barry Wardell, Niels Warburton, and Jeremy Miller. Second-order self-force calculation of gravitational binding energy in compact binaries. *Physical Review Letters*, 124(2), Jan 2020.

[204] Juri Poutanen, Sergei Fabrika, Alexey G. Butkevich, and Pavel Abolmasov. Supercritically accreting stellar mass black holes as ultraluminous X-ray sources. *Mon. Not. Roy. Astron. Soc.*, 377:1187–1194, 2007.

[205] Richard H. Price and Jorge Pullin. Colliding black holes: The close limit. *Physical Review Letters*, 72(21):32973300, May 1994.

[206] David Reitze, Rana X Adhikari, Stefan Ballmer, Barry Barish, Lisa Barsotti, Gari-Lynn Billingsley, Duncan A. Brown, Yanbei Chen, Dennis Coyne, Robert Eisenstein, Matthew Evans, Peter Fritschel, Evan D. Hall, Albert Lazzarini, Geoffrey Lovelace, Jocelyn Read, B. S. Sathyaprakash, David Shoemaker, Joshua Smith, Calum Torrie, Salvatore Vitale, Rainer Weiss, Christopher Wipf, and Michael Zucker. Cosmic explorer: The u.s. contribution to gravitational-wave astronomy beyond ligo, 2019.

[207] Adam G. Riess, Alexei V. Filippenko, Peter Challis, Alejandro Clocchiatti, Alan Diercks, Peter M. Garnavich, Ron L. Gilliland, Craig J. Hogan, Saurabh Jha, Robert P. Kirshner, and et al. Observational evidence from supernovae for an accelerating universe and a cosmological constant. *The Astronomical Journal*, 116(3):1009–1038, Sep 1998.

[208] Justin L. Ripley, Nicholas Loutrel, Elena Giorgi, and Frans Pretorius. Numerical computation of second order vacuum perturbations of kerr black holes, 2020.

[209] Travis Robson and Neil Cornish. Impact of galactic foreground characterization on a global analysis for the LISA gravitational wave observatory. *Class. Quant. Grav.*, 34(24):244002, 2017.

[210] Taeho Ryu, Takamitsu L. Tanaka, Rosalba Perna, and Zoltn Haiman. Intermediate-mass black holes from Population III remnants in the first galactic nuclei. *Mon. Not. Roy. Astron. Soc.*, 460(4):4122–4134, 2016.

[211] A. Sadowski. Slim accretion disks around black holes. *arXiv e-prints*, page arXiv:1108.0396, Aug 2011.

[212] Laura Sberna, Alexandre Toubiana, and M. Coleman Miller. Golden galactic binaries for lisa: mass-transferring white dwarf black hole binaries, 2020.

[213] M.D. Schwartz. *Quantum Field Theory and the Standard Model*. Quantum Field Theory and the Standard Model. Cambridge University Press, 2014.

[214] Noah Sennett, Tanja Hinderer, Jan Steinhoff, Alessandra Buonanno, and Serguei Ossokine. Distinguishing boson stars from black holes and neutron stars from tidal interactions in inspiraling binary systems. *Physical Review D*, 96(2), Jul 2017.

[215] Alberto Sesana. Prospects for Multiband Gravitational-Wave Astronomy after GW150914. *Phys. Rev. Lett.*, 116(23):231102, 2016.

[216] N. I. Shakura and R. A. Sunyaev. Black holes in binary systems. Observational appearance. *Astron. Astrophys.*, 24:337–355, 1973.

[217] Jean Sivardière. Adiabatic invariants for harmonic and kepler motions. *European Journal of Physics*, 9(2):150–151, apr 1988.

[218] D. Spergel and et al. Wide-Field InfrarRed Survey Telescope-Astrophysics Focused Telescope Assets WFIRST-AFTA 2015 Report. *arXiv e-prints*, March 2015.

[219] Leo C. Stein. qnm: A Python package for calculating Kerr quasinormal modes, separation constants, and spherical-spheroidal mixing coefficients. *J. Open Source Softw.*, 4(42):1683, 2019.

[220] James F. Steiner, Jeffrey E. McClintock, and Ramesh Narayan. Jet power and black hole spin: testing an empirical relationship and using it to predict the spins of six black holes. *The Astrophysical Journal*, 762(2):104, Dec 2012.

[221] Nicholas C. Stone, Brian D. Metzger, and Zoltn Haiman. Assisted inspirals of stellar mass black holes embedded in AGN discs: solving the final au problem. *Monthly Notices of the Royal Astronomical Society*, 464(1):946–954, 09 2016.

[222] Nicola Tamanini, Chiara Caprini, Enrico Barausse, Alberto Sesana, Antoine Klein, and Antoine Petiteau. Science with the space-based interferometer eLISA. III: Probing the expansion of the Universe using gravitational wave standard sirens. *JCAP*, 1604(04):002, 2016.

[223] Nicola Tamanini, Antoine Klein, Camille Bonvin, Enrico Barausse, and Chiara Caprini. The peculiar acceleration of stellar-origin black hole binaries: measurement and biases with LISA. 2019.

[224] Alexandre Toubiana, Laura Sberna, Andrea Caputo, Giulia Cusin, Sylvain Marsat, Karan Jani, Stanislav Babak, Enrico Barausse, Chiara Caprini, Paolo Pani, Alberto Sesana, and Nicola Tamanini. Detectable environmental effects in GW190521-like black-hole binaries with LISA, 2020.

[225] V Tudor, J C A Miller-Jones, C Knigge, T J Maccarone, T M Tauris, A Bahramian, L Chomiuk, C O Heinke, G R Sivakoff, J Strader, and et al. Hst spectrum and timing of the ultracompact x-ray binary candidate 47 tuc x9. *Monthly Notices of the Royal Astronomical Society*, 476(2):18891908, Feb 2018.

[226] Michele Vallisneri. Use and abuse of the Fisher information matrix in the assessment of gravitational-wave parameter-estimation prospects. *Phys. Rev.*, D77:042001, 2008.

[227] L. M. van Haaften, G. Nelemans, R. Voss, M. A. Wood, and J. Kuijpers. The evolution of ultracompact X-ray binaries. *A&A*, 537:A104, January 2012.

[228] Frank Verbunt and Saul Rappaport. Mass Transfer Instabilities Due to Angular Momentum Flows in Close Binaries. *The Astrophysical Journal*, 332:193, September 1988.

[229] Licia Verde, Tommaso Treu, and Adam G. Riess. Tensions between the early and late universe. *Nature Astronomy*, 3(10):891895, Sep 2019.

[230] Alexander Vilenkin. Creation of Universes from Nothing. *Phys. Lett.*, 117B:25–28, 1982.

[231] Justin Vines, Jan Steinhoff, and Alessandra Buonanno. Spinning-black-hole scattering and the test-black-hole limit at second post-minkowskian order. *Physical Review D*, 99(6), Mar 2019.

[232] R.M. Wald. *General Relativity*. University of Chicago Press, 1984.

[233] R.M. Wald and J.B.B.H. Pfister. *Quantum Field Theory in Curved Spacetime and Black Hole Thermodynamics*. Chicago Lectures in Physics. University of Chicago Press, 1994.

[234] Robert M. Wald. *Quantum Field Theory in Curved Space-Time and Black Hole Thermodynamics*. Chicago Lectures in Physics. University of Chicago Press, Chicago, IL, 1995.

[235] R. F. Webbink. Double white dwarfs as progenitors of R Coronae Borealis stars and type I supernovae. *The Astrophysical Journal*, 277:355–360, February 1984.

[236] Steven Weinberg. The cosmological constant problem. *Rev. Mod. Phys.*, 61:1–23, Jan 1989.

[237] Steven Weinberg. Quantum contributions to cosmological correlations. *Physical Review D*, 72(4), Aug 2005.

[238] Gregor Wentzel. Eine Verallgemeinerung der Quantenbedingungen für die Zwecke der Wellenmechanik. *Zeitschrift fur Physik*, 38(6-7):518–529, June 1926.

[239] Huan Yang, Kent Yagi, Jonathan Blackman, Luis Lehner, Vasileios Paschalidis, Frans Pretorius, and Nicols Yunes. Black hole spectroscopy with coherent mode stacking. *Physical Review Letters*, 118(16), Apr 2017.

[240] Yigit Yargic, Laura Sberna, and Achim Kempf. Which part of the stress-energy tensor gravitates? *Phys. Rev. D*, 101:043513, Feb 2020.

[241] Hang Yu and Yanbei Chen. A direct determination of supermassive black hole properties with gravitational-wave radiation from surrounding stellar-mass black hole binaries, 2020.

[242] Yungelson, L. R., Lasota, J.-P., Nelemans, G., Dubus, G., van den Heuvel, E. P. J., Dewi, J., and Portegies Zwart, S. The origin and fate of short-period low-mass black-hole binaries. *A&A*, 454(2):559–569, 2006.

[243] J. P. Zahn. Tidal friction in close binary stars. *A&A*, 500:121–132, May 1977.

[244] Zhongyang Zhang, Emanuele Berti, and Vitor Cardoso. Quasinormal ringing of kerr black holes. ii. excitation by particles falling radially with arbitrary energy. *Physical Review D*, 88(4), Aug 2013.

APPENDICES

Appendix A

White dwarf–black hole equilibrium solutions

After the initial phase of mass accretion, a very good approximation of the mass transfer rate between the white dwarf and the black hole can be obtained by setting the right hand side of Eq. (2.38) to 0. Similar equilibrium solutions were studied by Marsh et al. [171] for double white dwarf systems. We also set $\dot{M}_{\rm BH} = -\epsilon_{\rm ISCO}\dot{M}_{\rm WD}$. We find

$$\frac{\dot{M}_{\rm WD,\,e}}{M_{\rm WD}} = -\frac{\dot{J}_{\rm GW}/J_{\rm orb}}{K_{\rm eq}}, \tag{A.1}$$

where

$$\begin{aligned} K_{\rm eq} =& \frac{\zeta_{\rm WD} - \zeta_{r_L}}{2}(1 - 3(1+q)kr_{\rm WD}^2) + (1+q)\lambda kr_{\rm WD}^2(1-\epsilon_{\rm ISCO})(\frac{1}{2}qkr_{\rm WD}^2 - \frac{q}{2(1+q)}) \\ &+ 1 - \epsilon_{\rm ISCO}(q + j_{\rm GR}\sqrt{(1+q)r_{\rm ISCO}}). \end{aligned} \tag{A.2}$$

Using Kepler's law, $\frac{\dot{f}}{2f} = -\frac{3\dot{a}}{2a}$ and replacing Eq. (A.1) in Eq. (2.37) gives, at equilibrium:

$$\begin{aligned} \frac{\dot{f}}{2f} = \frac{3\dot{J}_{\rm GW}/J_{\rm orb}}{K_{\rm eq}(1-3(1+q)kr_2^2)}\Bigg[1 + \left(q - \frac{q}{2(1+q)} + \frac{1}{2}qkr_2^2 + j_{\rm GR}\sqrt{(1+q)r_{\rm ISCO}}\right)\epsilon_{\rm ISCO} \\ - \left(1 + \frac{q}{2(1+q)} + \frac{1}{2}qkr_2^2 + (1+q)\lambda kr_2^2\right)\Bigg]. \end{aligned} \tag{A.3}$$

Furthermore,

$$\frac{\dot{J}_{\rm GW}}{J_{\rm orb}} = \frac{32}{5}\frac{G^3}{c^5}\frac{M_{\rm BH}M_{\rm WD}M}{a^4} \propto M_{\rm BH}M_{\rm WD}M\left(\frac{M}{f^2}\right)^{4/3} \simeq M_{\rm BH}^{2/3}M_{\rm WD}f^{8/3}. \tag{A.4}$$

where in the last step we used $M_{\rm WD} \ll M_{\rm BH}$, so that $M \simeq M_{\rm BH}$. Finally, the late time evolution of the other terms in Eq. (A.3) happens to have a weak dependence on $M_{\rm BH}$, so $\dot{f}M_{\rm BH}^{-2/3}$ is an almost $M_{\rm BH}$ independent quantity as verified in Fig. 2.6, right panel.

Appendix B

Fits to the white dwarf–black hole evolutionary tracks

The coefficients for the evolutionary tracks fits described in the main text are summarized in Table B.1. The number of digits reported in the table is needed to obtain accurate estimates of the black hole and white dwarf masses.

	a_0	a_1	a_2	a_3	a_4
$y = M_{\rm WD}[M_\odot]$	319.7593186	509.0101135	303.8011829	80.7077869	8.0347503
$y = \dot{f} M_{\rm BH}^{-2/3}[{\rm Hz}\, M_\odot^{-2/3}/s]$	142.6384491	236.4026829	136.2183828	35.5719325	3.4778346

Table B.1: Coefficients for the fits to the evolutionary tracks, displayed in Figure 2.6.

Appendix C

Renormalized vacuum stress-energy tensor: free scalar field

In this Appendix, we compute the stress-energy tensor expectation value in the instantaneous ground states and adiabatic vacua, and confirm the results of Section 4.3 for a massive, non-minimally coupled but otherwise non-interacting scalar field. The results presented in this Appendix are not new and can be found elsewhere in the literature [47, 138, 77]. We find it convenient to rederive them here, to balance the theoretical arguments of Section 4.3 with a concrete example. This toy model demonstrates explicitly how instantaneous ground states give a covariantly conserved expectation value; how the adiabatic vacua fulfill the same property up to second adiabatic order; and how the subtraction cancels the radiative contributions to the cosmological constant but not those to the gravitational constant. Other examples can be found in [240].

Regularization is an essential step when dealing with a divergent expectation value. To ensure that the vacuum expectation value of the stress-energy tensor has the correct properties, *e.g.*, it is covariantly conserved, it is important to use a covariant regularization method. For a bosonic theory, we use dimensional regularization. See [191] for a comparison of regularization techniques for scalar fields.

The only dimensionful coupling included in our examples is the gravitational constant, which, in n spacetime dimensions, has mass dimension $[G^{(n)}] = M^{2-n}$. In dimensional regularization, in order to preserve the correct dimensionality while expanding around $n = 4$, we introduce $G^{(n)} = G\mu^{4-n}$ where μ is an arbitrary mass scale and $[G] = M^{-2}$. The

second equation in (4.32) becomes

$$G^{\text{ren.}} = \frac{G}{1 - 8\pi G \left(\mathcal{B}_{\text{AV}} - \mathcal{B}_{\text{GS}}\right) \mu^{4-n}} \,. \tag{C.1}$$

For simplicity, we specialize throughout this section to the flat FLRW metric with line element $\mathrm{d}s^2 = a(t)^2 \left(\mathrm{d}t^2 - \sum_{i=1}^{n-1} \mathrm{d}x_i^2\right)$ where $t = x^0$ is the conformal time and x^i are comoving coordinates. We denote derivatives with respect to the conformal time t by a prime $'$. We remind the reader that we are using units in which $\hbar = c = 1$.

Consider a scalar field ϕ with the action

$$S_\phi = \int \mathrm{d}^n x \, \sqrt{|g|} \left(-\frac{1}{2} \, g^{\mu\nu} \, \partial_\mu \phi \, \partial_\nu \phi - \frac{1}{2} \left(m^2 + \xi R\right) \phi^2 \right) \,, \tag{C.2}$$

where m is the mass, ξ is a dimensionless coupling constant and R is the Ricci scalar. The equation of motion for ϕ is given by

$$\phi'' + (n-2) \, \frac{a'}{a} \, \phi' - \partial_x^2 \phi + a^2 \left(m^2 + \xi R\right) \phi = 0 \,. \tag{C.3}$$

We decompose the field ϕ into its Fourier modes,

$$\phi(t,x) = \int \frac{\mathrm{d}^{n-1} k}{(2\pi)^{(n-1)/2}} \frac{1}{\sqrt{2}} \, a(t)^{-(n-2)/2} \left(\chi_k(t) \, e^{-ikx} \, \hat{a}_k + \chi_k^*(t) \, e^{ikx} \, \hat{a}_k^\dagger \right) \,, \tag{C.4}$$

where $\hat{a}_k$ and $\hat{a}_k^\dagger$ are annihilation and creation operators, and $\chi_k(t)$ is a complex mode function. Note that this decomposition is not unique: one can choose a different set of annihilation and creation operators or, equivalently, a different set of mode functions. Each set of operators defines a vacuum according to $\hat{a}_k \, |0\rangle = 0$, $\forall k$.

The mode functions satisfy the equation of motion

$$\chi_k'' + \left(k^2 + m^2 a^2 - \left(\xi_n - \xi\right) a^2 R\right) \chi_k = 0 \,, \tag{C.5}$$

where we defined $\xi_n \equiv \frac{n-2}{4(n-1)}$. The scalar field is minimally coupled when $\xi = 0$ and conformally coupled when $\xi = \xi_n$.

We perform the canonical quantization by imposing canonical commutation relations $[\hat{\phi}(t,x), \hat{\Pi}(t,y)] = i \, \delta^{n-1}(x-y)$, where $\Pi(t,x) = \delta S_\phi / \delta \phi'(t,x) = a(t)^{n-2} \, \phi'(t,x)$ is the conjugate momentum, as well as $[\hat{a}_k, \hat{a}_l^\dagger] = \delta^{n-1}(k-l)$. Consistency between the commutation relations implies the Wronskian condition

$$\chi_k \, \chi_k'^* - \chi_k' \, \chi_k^* = 2i \,. \tag{C.6}$$

Since (C.5) is a second-order differential equation of a complex function, the space of solutions is 4-dimensional for each mode k. One degree of freedom is an arbitrary global phase. The Wronskian condition (C.6) constrains one more degree of freedom, so we are left with 2 *physical* degrees of freedom for χ_k (for each k).

It is possible to decouple the non-physical degrees of freedom from the mode functions as follows: we write the mode function $\chi_k(t)$ in the polar form as $\chi_k(t) = R_k(t)\,\exp\{-iS_k(t)\}$, where $R_k(t)$ and $S_k(t)$ are real functions. In these new variables, the Wronskian condition (C.6) becomes $R_k^2\,S_k' = 1$. This equation is solved by any positive real function $\Omega_k(t)$ with $\Omega_k(t) = R_k(t)^{-2}$ and $S_k(t) = \int^t \Omega_k(\bar{t})\,\mathrm{d}\bar{t}$ with an arbitrary lower limit of integration corresponding to an arbitrary phase,

$$\chi_k(t) = \frac{1}{\sqrt{\Omega_k(t)}}\,\exp\left\{-i\int^t \Omega_k(\bar{t})\,\mathrm{d}\bar{t}\right\}. \tag{C.7}$$

Then, the equation of motion (C.5) becomes

$$\Omega_k(t)^2 = \omega_k(t)^2 + (\xi_n - \xi)\,a(t)^2 R(t) + \frac{3}{4}\frac{\Omega_k'(t)^2}{\Omega_k(t)^2} - \frac{1}{2}\frac{\Omega_k''(t)}{\Omega_k(t)}\,. \tag{C.8}$$

Here $\omega_k(t)^2 = k^2 + m^2 a(t)^2$. The solution Ω_k can be specified by the initial value and its time derivative (for each k), which correspond to the 2 physical degrees of freedom in χ_k. The problem of defining the vacuum is therefore reduced to choosing a solution to the non-linear differential equation (C.8).

Stress-energy tensor. The stress-energy tensor $T_{\mu\nu}$ for the scalar field ϕ is given by

$$\begin{aligned} T_{\mu\nu} = {} & \partial_\mu\phi\,\partial_\nu\phi - \xi R_{\mu\nu}\,\phi^2 + \xi\,\nabla_\mu\nabla_\nu(\phi^2) - \xi\,g_{\mu\nu}\,\Box(\phi^2) - \frac{1}{2}\,g_{\mu\nu}\,g^{\alpha\beta}\,\partial_\alpha\phi\,\partial_\beta\phi \\ & - \frac{1}{2}\,g_{\mu\nu}\left(m^2 + \xi R\right)\phi^2\,. \end{aligned} \tag{C.9}$$

We promote this to an operator $\hat{T}_{\mu\nu}$ with *symmetrized* operator ordering[1], *e.g.*, $\phi\phi' \to \frac{1}{2}\{\hat{\phi},\hat{\phi}'\}$, [60]

$$\begin{aligned} \langle 0|\,\hat{T}_{00}\,|0\rangle = {} & \frac{1}{4a^{n-2}}\int\frac{\mathrm{d}^{n-1}k}{(2\pi)^{n-1}}\,\frac{1}{\Omega_k}\left(k^2 + m^2a^2 + \Omega_k^2 + \frac{\Omega_k'^2}{4\Omega_k^2}\right. \\ & \left. + (\xi_n - \xi)\,(n-1)\,\frac{a'\left((n-2)\,a'\,\Omega_k + 2a\,\Omega_k'\right)}{a^2\,\Omega_k}\right), \end{aligned} \tag{C.10a}$$

[1]Normal ordering, the standard operator ordering in QFT on flat spacetimes, does not have a generally covariant analogue, and cannot be implemented in our setting. Symmetrized ordering, on the other hand, is covariant.

$$\langle 0|\,\hat{T}_{0j}\,|0\rangle = 0\,, \tag{C.10b}$$

$$\begin{aligned}\langle 0|\,\hat{T}_{ij}\,|0\rangle = \frac{1}{4a^{n-2}}\int\frac{\mathrm{d}^{n-1}k}{(2\pi)^{n-1}}\,\frac{1}{\Omega_k}\Bigg(&2k_ik_j\\ &+\delta_{ij}\,(\xi_n-\xi)\left(4\xi a^2R+(n-1)\,\frac{a'\left((n-2)\,a'\,\Omega_k+2a\,\Omega_k'\right)}{a^2\,\Omega_k}\right)\\ &+\delta_{ij}\,(1-4\xi)\left(\Omega_k^2-k^2-m^2a^2+\frac{\Omega_k'^2}{4\Omega_k^2}\right)\Bigg),\end{aligned} \tag{C.10c}$$

where $i,j\in\{1,...,n-1\}$. If $\Omega_k(t)$ depends only on the modulus $k\equiv|\vec{k}|$, then all non-diagonal terms of $\langle 0|\,\hat{T}_{\mu\nu}\,|0\rangle$ vanish. This is the case for the adiabatic and ground state vacua that we will consider, because of their symmetry properties.

Ground state. The instantaneous ground state at time t is given by the initial values $\{\Omega_k(t),\Omega_k'(t)\}$ which minimize the energy density $\langle 0|\,\hat{T}_{00}\,|0\rangle$ at that time. Setting $\partial\,\langle 0|\,\hat{T}_{00}\,|0\rangle\,(t)/\partial\Omega_k(t)=0$ and $\partial\,\langle 0|\,\hat{T}_{00}\,|0\rangle\,(t)/\partial\Omega_k'(t)=0$ corresponds to

$$\Omega_k(t)=\sqrt{k^2+m^2\,a(t)^2+4\,(n-1)^2\,\xi\,(\xi_n-\xi)\,\frac{a'(t)^2}{a(t)^2}}\,, \tag{C.11a}$$

$$\Omega_k'(t)=4\,(n-1)\,(\xi-\xi_n)\,\frac{a'(t)}{a(t)}\,\Omega_k(t)\,. \tag{C.11b}$$

We clarify here that, while these initial conditions can be used together with Eqs. (C.8) and (C.7) to define a ground state mode function at all times, we wish to compute our expectation values at every time t on the ground state at that time. For this, it is sufficient to directly use (C.11b).

We substitute the expressions above at every time t into (C.10a) and (C.10c). After Taylor expanding around the number of derivatives on the scale factor $a(t)$, we can write the result as

$$\langle\hat{T}_{\mu\nu}\rangle_{\mathrm{GS}(t)}=\left(\frac{m^2}{4\pi}\right)^{n/2}\Gamma\Big[-\frac{n}{2}\Big]\left(-\frac{1}{2}\,g_{\mu\nu}+\frac{n}{2}\,\frac{\xi}{\xi_n}\,(\xi-\xi_n)\,m^{-2}\,G_{\mu\nu}\right)+\mathcal{O}(\partial^4)\,. \tag{C.12}$$

Adiabatic vacuum. In order to define the adiabatic vacua, we solve (C.8) iteratively, so that

$$\left(W_k^{[0]}(t)\right)^2=\omega_k(t)^2\,, \tag{C.13a}$$

$$\left(W_k^{[\mathrm{s}+1]}(t)\right)^2=\omega_k(t)^2+(\xi_n-\xi)\,a(t)^2R(t)+\frac{3}{4}\left(\frac{W_k^{[\mathrm{s}]\prime}(t)}{W_k^{[\mathrm{s}]}(t)}\right)^2-\frac{1}{2}\frac{W_k^{[\mathrm{s}]\prime\prime}(t)}{W_k^{[\mathrm{s}]}(t)}\,. \tag{C.13b}$$

The 2nd order adiabatic vacuum at time t is then defined by the initial conditions

$$\Omega_k(t) = W_k^{[1]}(t) \,, \qquad \Omega_k'(t) = W_k^{[1]\prime}(t) \,. \tag{C.14}$$

In order to find the adiabatic vacuum expectation value of the stress-energy tensor, we substitute (C.14) into (C.10a) and (C.10c). After expanding the result in the number of derivatives on the scale factor, we get

$$\langle \hat{T}_{\mu\nu} \rangle_{\mathrm{AV}(t)} = \left(\frac{m^2}{4\pi}\right)^{n/2} \Gamma\Big[-\frac{n}{2}\Big] \left(-\frac{1}{2}\, g_{\mu\nu} + \frac{n\,(\xi_n - \xi)}{2\xi_n}\, m^{-2}\, G_{\mu\nu}\right) + \mathcal{O}(\partial^4) \,. \tag{C.15}$$

Effective stress-energy tensor. Our results (C.12) and (C.15) confirm Theorems 1 and 2, since these stress-energy expectation values are a linear combination of the covariantly conserved tensors $g_{\mu\nu}$ and $G_{\mu\nu}$. They also confirm Theorem 3,

$$\mathcal{A}_{\mathrm{GS}} = \mathcal{A}_{\mathrm{AV}} = -\frac{1}{2}\left(\frac{m^2}{4\pi}\right)^{n/2} \Gamma\Big[-\frac{n}{2}\Big] \,. \tag{C.16}$$

Finally, by subtracting (C.15) and (C.12), we obtain

$$\langle \hat{T}_{\mu\nu} \rangle^{\mathrm{vac.}} = \mathcal{B}_\Delta\, G_{\mu\nu} + \mathcal{O}(\partial^4) \,, \tag{C.17}$$

where $\mathcal{B}_\Delta = \mathcal{B}_{\mathrm{AV}} - \mathcal{B}_{\mathrm{GS}}$ is given for the scalar theory by

$$\mathcal{B}_\Delta = \left(\frac{m^2}{4\pi}\right)^{n/2} \Gamma\Big[-\frac{n}{2}\Big]\, \frac{n}{12} \left(1 - \frac{24\,(n-1)}{n-2}\, \xi^2\right) m^{-2} \,, \tag{C.18}$$

confirming the results of Section 4.3.4.

In order to complete dimensional renormalization, we expand $\mathcal{B}_\Delta = \mathcal{B}_\Delta(n)$ around $n = 4$. Depending on the parameter ξ, this can be accomplished in two different ways. If we fix the parameter ξ to the conformal coupling number $\xi = \xi_n$ for every dimension n, we get a finite result at $n = 4$, namely

$$\mu^{4-n}\, \mathcal{B}_\Delta\big|_{\xi=\xi_n}(n=4) = \frac{m^2}{288\pi^2} \,. \tag{C.19}$$

Alternatively, we can fix the parameter ξ to a constant independent of n and make a Laurent expansion around $n = 4$ to get

$$\begin{aligned} \mu^{4-n}\, \mathcal{B}_\Delta\big|_{\xi=\mathrm{const.}}(n) = {} & \frac{(1-36\xi^2)\, m^2}{48\pi^2\,(4-n)} - \frac{(1-36\xi^2)\, m^2}{96\pi^2}\left(\gamma + \log\frac{m^2}{4\pi\mu^2}\right) \\ & + \frac{(1-48\xi^2)\, m^2}{96\pi^2} + \mathcal{O}(4-n) \,, \end{aligned} \tag{C.20}$$

where γ is the Euler-Mascheroni constant.